CERN-THESIS-2008-245

Measurement of Ξ^- yield at the NA57 experiment and a Monte Carlo study of the ρ^0 resonance at the ALICE experiment

Richard J. Platt

Thesis submitted for the degree of
Doctor of Philosophy

Particle Physics Group,
School of Physics and Astronomy,
University of Birmingham.

February 2008

Abstract

Experiments have studied heavy ion collisions with the aim of creating and studying a new state of matter, the Quark Gluon Plasma (QGP). In this state of matter, quarks and gluons are not confined to hadrons but behave as free particles. The theoretical background is described, including some expected signatures of the QGP. Some previous experimental results are also discussed.

Two analyses are presented. The first analysis involves the measurement of the yield of the Ξ^- particle in p-Be collisions at 40 GeV/c at NA57, with the aim of measuring *strangeness enhancement*, a proposed signature of the QGP. The Ξ^- yield, measured in this analysis, is compared to the previously obtained yield in Pb-Pb. It is shown that Ξ^- production is enhanced in heavy ion collisions.

The second analysis investigates the prospects for ρ^0 measurement at the future ALICE experiment. Measurement of ρ^0 mass, width and yield may provide information on the state of matter created in the collision. This thesis describes the methods used to carry out this analysis and the systematic and statistical errors involved in the measurement. It is shown that ALICE is potentially capable of measuring the ρ^0 properties in pp and Pb-Pb collisions.

Author's Contribution

This work made use of previously developed software and previously collected data sets. For the NA57 analysis, described in chapters 3 and 4, I made use of the previously available samples of cascades. I investigated many different selection cuts in order to remove the background from the sample, in a continuation of work begun by Dr. P. I. Norman. The final cuts used and all of the plots shown in chapter 3 were obtained from my own investigations. A "clean" sample of Ξ^- candidates was obtained and was used in the later analysis.

The NA57 analysis made use of previously developed software. I used this software to determine the total yields of Ξ^- in p-Be collisions at 40 GeV/c, using the sample of Ξ^- particles obtained in chapter 3. I also tested the technique used to calculate this yield by beginning with a known number of Ξ^- particles and simulating their detection at NA57. I obtain a final yield of Ξ^- in p-Be and a slope parameter which describes the transverse mass distribution of the Ξ^- particles.

My analysis of the ρ^0 at the ALICE experiment required the development of my own software. I developed and used my own fast simulation routine, described in chapter 5. This involved investigating the properties of events generated using the standard ALICE detector simulation and reconstruction software in order to determine what approximations could be reasonably made. This fast simulation routine was then used, together with the existing PYTHIA and HIJING event generators, to generate a large sample of pp and Pb-Pb events. I also developed the software

used to process these simulated events to reconstruct the ρ^0 signal.

I then used this software in the ρ^0 analysis described in chapter 6. I investigated various methods of subtracting background and fitting a ρ^0 to the reconstructed invariant mass spectrum. I also investigated the sources of statistical and systematic errors which may affect the measurement. I showed that measurement of ρ^0 at ALICE should be possible in both pp and Pb-Pb collisions.

Acknowledgements

In the course of my PhD, I have received valuable help and support from a number of people, and I would like to acknowledge them here.

Firstly, I would like to thank my supervisors, Dr. David Evans and Dr. Orlando Villalobos-Baillie, for providing help with every aspect of my work. Thanks must also go to the other staff in the Birmingham NA57 and ALICE groups, including Dr. Gron Tudor-Jones, Dr. Roman Lietava, Dr. Paul Norman and Dr. John Kinson.

I would also like to express gratitude to the other heavy ion students that I worked with, namely Rory Clarke, Stephen Bull, Paul Bacon, Daniel Tapia-Takaki and Liam Daniel. Their help with software, analysis and physics discussions was essential, not to mention their entertaining company in the office and during trips to CERN. I wish good luck to the newer ALICE students, Hannah Scott, Zoe Matthews, Sparsh Navin and Ravjeet Kour.

Although not a member of the Birmingham group, a special note of thanks should go to Jouri Belikov for his very patient assistance with the ALICE software when I was beginning the work and for subsequent advice.

I also owe thanks to many people outside the NA57 and ALICE collaborations, including Dr. Ray Jones and Professor Peter Watkins for their help and support, the Particle Physics and Astronomy Research Council for funding my work, Dr. Lawrence Lowe for technical help with computing, Tamsin Moye for interesting

discussions and lunchtime crosswords and many other people, too numerous to list here, for enjoyable evenings in Staff House.

Finally, I would like to thank my parents for their constant support throughout my studies, without which this thesis would not have been possible.

Contents

1 Theory **1**

1.1 Introduction 1

1.2 Quantum Chromodynamics 2

1.2.1 Renormalization and running coupling constants 2

1.2.2 Calculations in non-perturbative QCD 6

1.2.3 Confinement 7

1.2.4 Breaking of chiral symmetry 7

1.3 The Quark-Gluon plasma 8

1.3.1 The Phase Diagram of QCD 8

1.3.2 Chiral symmetry restoration 11

1.3.3 Conditions under which the QGP may exist 11

1.4 Heavy Ion Collisions 12

1.4.1 QGP in Heavy Ion Collisions 12

1.4.2 Heavy Ion Kinematics 12

1.4.3 Heavy Ion Experiments 15

1.5 Signatures of the Quark-Gluon Plasma 16

1.5.1 Introduction 16

1.5.2 Strangeness enhancement 16

1.5.3 Canonical suppression 19

1.6 Resonances as QGP probes 21

1.6.1 Introduction 21

1.6.2 Daughter particle rescattering 22

1.6.3 Modification of resonance properties in a medium 22

1.6.4 Resonances as a probe of time evolution of the fireball 23

1.6.5 Previous resonance results 24

1.6.6 Other signatures 26

2 Experiment **29**

2.1 The CERN accelerator complex 29

2.1.1 The Super Proton Synchrotron (SPS) 30

2.1.2 The Large Hadron Collider (LHC) 30

2.2 The NA57 Experiment 32

2.2.1 Beam and Target 33

2.2.2 The Silicon Telescope 34

2.2.3 The Trigger System 35

2.3 The ALICE Experiment at the LHC 37

2.3.1 Introduction 37

2.4 The ALICE experiment overview 37

2.4.1 The ALICE main sub-detectors 37

2.4.2 Inner Tracking System 40

2.4.3 Time Projection Chamber 41

2.4.4 Transition Radiation Detector 42

2.4.5 Time of Flight Detector 43

2.4.6 The Trigger 44

2.4.7 Data Acquisition (DAQ) system 47

3 Reconstruction and selection of strange particles at NA57 48

3.1 Introduction 48

3.2 Track reconstruction 48

3.3 Data sets 49

3.4 V^0 and cascade decays 50

3.4.1 Cowboys and sailors 50

3.5 Selection Cuts 51

3.5.1 Decay Vertex Position 52

3.5.2 Closest approach of decay tracks . . . 55
3.5.3 Internal decay angle . . . 56
3.5.4 Armenteros-Podolanski cuts . . . 57
3.5.5 Primary vertex position . . . 60
3.5.6 Summary of Cuts . . . 60
3.6 Ξ signal . . . 63

4 Yield Calculation **66**

4.1 The Weighting Chain . . . 66
4.1.1 Particle Generation and Weight Calculation . . . 67
4.2 Acceptance region . . . 68
4.2.1 m_t slopes . . . 69
4.2.2 Extrapolation to full p_t . . . 69
4.2.3 Monte Carlo determination of acceptance region . . . 71
4.2.4 Test of weighting procedure . . . 71
4.2.5 Breakdown of weights . . . 77
4.3 Yields . . . 78
4.3.1 2001 Data . . . 78
4.3.2 1999 Data . . . 79
4.3.3 Combined Data . . . 79

4.3.4 Results summary 81

4.4 Enhancements 81

4.5 Conclusions 83

5 Monte Carlo simulations at ALICE **85**

5.1 Introduction 85

5.2 Simulation of events 86

5.2.1 The PYTHIA Monte Carlo generator 86

5.2.2 The HIJING Monte Carlo generator 87

5.2.3 Simulation of ALICE detector response 88

5.2.4 Reconstruction of events 88

5.3 The PYTHIA Monte Carlo generator's predictions of the ρ^0 89

5.4 Properties of reconstructed events 91

5.4.1 Primary and secondary tracks 91

5.4.2 Relative abundances of particle species 96

5.5 Detector acceptance and efficiency 97

5.5.1 Efficiency as a function of pseudorapidity 97

5.5.2 Efficiency as a function of transverse momentum 98

5.6 Track momentum resolution 100

5.6.1 Errors in reconstruction 100

5.6.2 Errors in calculation of resonance properties 101

5.7 Particle identification 103

5.8 Fast simulation 104

5.8.1 Acceptance and efficiency 107

5.8.2 Momentum errors 107

5.8.3 Particle Identification modelling 108

5.8.4 Fast simulation performance 109

6 Analysis of the ρ^0 resonance at ALICE **111**

6.1 Introduction 111

6.2 Analysis of the ρ^0 in Pb-Pb collisions 112

6.2.1 Event generation 112

6.2.2 Selection of tracks 113

6.2.3 ρ reconstruction and background subtraction 115

6.2.4 Like-sign background subtraction 115

6.2.5 Mixed event background subtraction 119

6.2.6 Fitting method 119

6.2.7 Fit results 121

6.2.8 Systematic errors in fitting 122

6.2.9 Signal-to-background ratio and significance 125

6.2.10 Effect of reduced signal . . . 127

6.2.11 Error analysis . . . 128

6.2.12 Conclusions . . . 129

6.3 Analysis of the ρ^0 in pp collisions . . . 130

6.3.1 Event generation, fast simulation, reconstruction and background subtraction . . . 131

6.3.2 Fitting . . . 134

6.3.3 Signal-to-background ratio and significance . . . 138

6.3.4 Conclusions for pp measurements . . . 139

6.4 Limitations of these studies . . . 140

7 Summary and conclusions **142**

7.1 Strangeness results summary . . . 142

7.2 Resonance results summary . . . 143

7.3 Extensions and improvements . . . 144

A Bayesian PID in the ALICE detector **146**

A.1 PID in a single detector . . . 146

A.2 Combined PID . . . 147

List of Figures

1.1 Feynman diagrams for electron-muon scattering, with the tree-level diagram on the left and a higher order correction from the vacuum polarization on the right. 3

1.2 A gluon loop in QCD. 4

1.3 Variation of the strong interaction coupling parameter α_s with four momentum transfer Q. 5

1.4 A simple phase diagram of QCD, obtained from the Bag Model, with a rough indication of conditions reached at the Super Proton Synchrotron (SPS), the Relativistic Heavy Ion Collider (RHIC) and the Large Hadron Collider (LHC). The values of T_c at $\mu = 0$ and μ_c at $T = 0$ are shown on the axes. These were obtained from lattice QCD calculations, and are about 170 MeV for T_c and about 1 GeV for μ_c. . 9

1.5 Energy density divided by the fourth power of temperature as a function of temperature, obtained from lattice QCD calculations. The values for ideal Stefan-Boltzmann behaviour are shown by the arrows on the right. 10

1.6 A simple model of the rapidity distribution of particles in the centre of mass frame for a heavy ion collision, with the QGP fireball at central rapidity and the projectile fragmentation regions at high rapidity. . . 13

1.7 An example of a collision of two lead nuclei with impact parameter b. The "wounded nucleons" are shaded in black. 14

1.8 Feynman diagram showing strange quark production by gg fusion. . . 17

1.9 Enhancement of strange baryon production in 158A GeV/c Pb-Pb collisions at the WA97 experiment, normalised to the yield in 158 GeV/c p-Be collisions. 19

1.10 Comparison of strange particle enhancements in heavy ion collisions at STAR and NA57. N_{Part} refers to the number of participant nucleons, where "participant nucleon" is defined in the same way as "wounded nucleon", which is the term used elsewhere. 20

1.11 Canonical suppression model prediction of centrality dependence of Ξ^- enhancement in Pb-Pb collisions at different collision energies. . . 21

1.12 Comparison of excess dimuon mass spectra at NA60 after subtraction of background and known meson contributions. The left plot shows the ρ^0 in peripheral In-In collisions, and the right plot suggests a broadened ρ in more central collisions. 24

1.13 ρ mass as a function of transverse momentum, as measured in the $\pi^+\pi^-$ decay channel at the STAR experiment. 25

1.14 Azimuthal distribution of high-p_t particles measured at the STAR experiment, showing the disappearance of the corresponding "back-to-back" peak in central Au-Au collisions. 28

2.1 The CERN accelerator complex. 31

2.2 The NA57 apparatus as set up for p-Be collisions. The silicon telescope was 40 cm from the target at angle α to the beam. 33

2.3 The ALICE detector. 38

3.1 A cowboy (left) and sailor (right) V^0 decay. The cowboy topology is preferred as the tracks are closer together when they reach the silicon telescope, and so are more likely to both be reconstructed. 51

3.2 Reconstructed Ξ mass distribution for the 2001 sample after preliminary cuts. 52

3.3 Ξ mass against V^0 decay vertex position. Background from interactions in the triggering scintillator is observable at $-27 < x < -25$ cm. Only Ξ candidates whose V^0 vertices were before the scintillator, i.e. to the left of the vertical line, were accepted. 54

3.4 Ξ mass against closest approach of cascade decay tracks. 55

3.5 The internal decay angle of a V^0 decay. The left diagram shows the decay particles emitted back-to-back in the y'-z' plane. The right diagram shows the bending of tracks in the magnetic field and the tracing back from the detector to a vertex. 57

3.6 Ξ mass against the internal decay angle ϕ for the 2001 data sample. The cut on ϕ is shown by the vertical lines. 58

3.7 Armenteros-Podolanski plot for V^0s from NA57 data. 59

3.8 Distribution of primary vertex positions of cascades after other cuts have been applied. 61

3.9 Plot of reconstructed Ξ mass for 2001 Ξ candidates after all cuts apart from the Ξ mass cut. 63

3.10 Plot of reconstructed Ξ mass for 1999 Ξ candidates after all cuts apart from the Ξ mass cut. 64

4.1 Variation of acceptance with rapidity and transverse momentum for Ξ^- particles. The darker regions correspond to greater acceptance. A Ξ^- with p_t and Y in such a region is more likely to be successfully reconstructed than one in a "light" region. 70

4.2 Transverse mass fit for 2001 Ξ^-s, with the fitted inverse slope of 157 MeV shown. 72

4.3 Acceptance of Monte Carlo Ξ^- particles for 1999 and 2001 data sets. Each point corresponds to a reconstructed MC Ξ^-. The large circles indicate those Ξ^- particles which were poorly accepted, i.e. where the probability of successful reconstruction is less than a tenth of the probability for the best accepted Ξ^-. 73

4.4 Transverse mass fit for 1999 Monte Carlo Ξ^-s. 76

4.5 Acceptance region containing the 1999 and 2001 Ξ^- candidates. The large dots indicate weights greater than ten times the smallest weight. The lower curve indicates the lower angle. 80

4.6 Enhancement of Ξ^- going from p-Be to Pb-Pb collisions at 40 GeV/c per nucleon. 84

4.7 Enhancement of Ξ^- going from p-Be to Pb-Pb collisions at 158 GeV/c per nucleon. 84

5.1 Rapidity distribution of generated ρ^0 particles for 10^5 PYTHIA pp events. 90

5.2 Rapidity distribution of generated ρ^0 particles for 10^5 PYTHIA pp events, where the ρ^0 decay tracks have pseudorapidities within the TPC acceptance of $-0.9 < \eta < 0.9$. 90

5.3 Transverse momentum distribution of generated ρ^0 particles for 10^5 PYTHIA pp events. 91

5.4 Ratio of primary tracks to total tracks for tracks satisfying the ITS fitting requirement, divided into 100 MeV/c bins, with no impact parameter cut imposed. The black circles are the values for all particle species and the red triangles are the values for pions only. 92

5.5 The impact parameter in the x-y plane. 93

5.6 Ratio of primary tracks to total tracks for tracks satisfying the ITS fitting requirement and the χ^2 cut, divided into 100 MeV/c bins, with no impact parameter cut imposed. The black circles are the values for all particle species and the red triangles are the values for pions only. 95

5.7 Reconstruction efficiency as a function of pseudorapidity for tracks from PYTHIA pp events which have p_t above 0.2 GeV/c and are either π^+, K^+ or p or their charge conjugates. 97

5.8 Reconstruction efficiency as a function of pseudorapidity for tracks from HIJING central Pb-Pb events which have p_t above 0.2 GeV/c and are either π^+, K^+ or p or their charge conjugates. 98

5.9 Reconstruction efficiency as a function of transverse momentum for pion tracks from PYTHIA pp events which have η between -0.7 and +0.7. 99

5.10 Reconstruction efficiency as a function of transverse momentum for pion tracks from PYTHIA pp events which have η between -0.7 and +0.7. 99

5.11 Reconstruction efficiency as a function of transverse momentum for kaon tracks from PYTHIA pp events which have η between -0.7 and +0.7. 100

5.12 Errors in measurement of ρ transverse momentum, defined as the reconstructed p_t minus the generated p_t. There is a shift of +4.1 MeV/c and a random error with an RMS value of 14.0 MeV/c. 102

5.13 Errors in reconstructed ρ^0 mass. There is a shift of +2.1 MeV/c^2, a random error with an RMS value of 6.4 MeV/c^2. 103

5.14 The distribution of error, defined as the reconstructed value minus the generated value, in the reconstructed ρ^0 rapidity values. There is a shift of -6.8×10^{-5} units of rapidity and a random error with an RMS value of 0.0046 units of rapidity. 104

6.1 Ratio of ρ to π for various collision systems and energies, including HIJING's prediction for Pb–Pb at ALICE. The other systems are e^+e^- at 10.45 GeV and 91 GeV, pp at 6.8 GeV, 19.7 GeV, 27.5 GeV and 52.5 GeV, K^+p at 7.82 GeV, π^-p at 19.6 GeV and peripheral Au-Au at 200 GeV. 113

6.2 Plot of ρ^0 invariant mass signal (solid line) and K^{0*} invariant mass signal (broken line) for 10^6 central HIJING Pb-Pb events using a $\pi^+\pi^-$ hypothesis. 114

6.3 Unsubtracted $\pi^+\pi^-$ invariant mass spectrum for 10^6 central Pb-Pb events. 116

6.4 Background-free ρ^0 invariant mass spectrum for 10^6 central Pb-Pb events. 116

6.5 Comparison of unlike-sign (solid line) and like-sign (circular points) histograms for 10^6 central HIJING Pb-Pb events. 117

6.6 $\pi^+\pi^-$ spectrum for 10^6 central events after like-sign background subtraction, showing individual contributions. 118

6.7 Fit to background-subtracted $\pi^+\pi^-$ spectrum. 122

6.8 Number of reconstructed ρ^0s divided by number of generated ρ^0s. It can be seen that the detected ρ^0 shape is different from the generated shape, as the plot is not flat across the ρ^0 mass range. No normalisation is applied to the samples so the Y-axis units are arbitrary. 123

6.9 Fit to reconstructed ρ^0 signal, with background removed using the MC truth information. 124

6.10 Fit to generated ρ^0 signal, with background removed using the MC truth information. 125

6.11 $\pi^+\pi^-$ invariant mass spectrum for 5×10^7 PYTHIA pp events after like-sign background subtraction, for resonance candidates with any p_t. 132

6.12 $\pi^+\pi^-$ invariant mass spectrum for 5×10^7 PYTHIA pp events after like-sign background subtraction, for resonance candidates with $p_t <$ 1 GeV/c. 132

6.13 $\pi^+\pi^-$ invariant mass spectrum for 5×10^7 PYTHIA pp events after like-sign background subtraction, for resonance candidates with $1 < p_t < 2$ GeV/c. 133

6.14 $\pi^+\pi^-$ invariant mass spectrum for 5×10^7 PYTHIA pp events after like-sign background subtraction, for resonance candidates with $2 < p_t < 4$ GeV/c. 133

6.15 Fit of equation 6.5 to like-sign subtracted $\pi^+\pi^-$ spectrum for resonance candidates of any p_t. The solid dots show the like-sign subtracted spectrum and the crosses show the ρ^0 component. The ρ^0 component of the fit is also shown in the plot for comparison with the actual ρ^0 contribution. 135

6.16 Fit of equation 6.5 to like-sign subtracted $\pi^+\pi^-$ spectrum for resonance candidates with $0 < p_t < 1$ GeV/c. The solid dots show the like-sign subtracted spectrum and the crosses show the ρ^0 component. The ρ^0 component of the fit is also shown in the plot for comparison with the actual ρ^0 contribution. 135

6.17 Fit of equation 6.5 to like-sign subtracted $\pi^+\pi^-$ spectrum for resonance candidates with $1 < p_t < 2$ GeV/c. The solid dots show the like-sign subtracted spectrum and the crosses show the ρ^0 component. The ρ^0 component of the fit is also shown in the plot for comparison with the actual ρ^0 contribution. 136

6.18 Fit of equation 6.5 to like-sign subtracted $\pi^+\pi^-$ spectrum for resonance candidates with $2 < p_t < 4$ GeV/c. The solid dots show the like-sign subtracted spectrum and the crosses show the ρ^0 component. The ρ^0 component of the fit is also shown in the plot for comparison with the actual ρ^0 contribution. 136

6.19 A fit to the reconstructed ρ^0 signal, with all background removed using the Monte Carlo truth information. The fitted mass is 0.76626 GeV/c^2 and the fitted width is 0.14277 GeV/c^2. 137

List of Tables

2.1 Some collision systems studied at the LHC. 32

2.2 Summary of the collision systems studied at NA57 and WA97. 34

4.1 Acceptance window parameters for the 2001 Monte Carlo Ξ^-s. 74

4.2 Comparison between generated and reconstructed yield and slope for the 2001 Monte Carlo Ξ^-s. 74

4.3 Comparison between generated and reconstructed yield and slope for the 2001 Monce Carlo Ξ^-s for a subsample of 35. 74

4.4 Comparison between generated and reconstructed yield and slope for the 1999 Monte Carlo Ξ^-s. 75

4.5 Comparison between generated and reconstructed yield and slope for combined MC Ξ^-. 76

4.6 Summary of Ξ^- yield and inverse slope measurements in p-Be collisions at 40 GeV/c and a comparison with the WA97 p-Be results at 158 GeV/c. The extrapolated yields for the 1999 and 2001 data sets were calculated assuming the inverse slope from the 2001 data set. . . 81

4.7 Yields in Pb-Pb collisions at 40 GeV/c per nucleon. 82

4.8 Ξ^- yields per unit rapidity per wounded nucleon and enhancements in Pb-Pb and p-Be collisions at 40 GeV/c per nucleon. 83

5.1 Table showing the fraction of generated ρ^0s in several p_t sub-regions. . 91

5.2 Relative abundances of the particle species of reconstructed tracks, obtained from a sample of PYTHIA pp events. 96

6.1 Fitted values of ρ^0 mass and width for generated and reconstructed ρ^0s in the absence of background, and a comparison to the generator input values. 124

6.2 Significance and S/B values for ρ^0 in various p_t regions for 10^6 HIJING central Pb–Pb events. 126

6.3 Significance and S/B values for ρ^0 at high p_t based on a sample of 93,000 HIJING central Pb–Pb events. Significance is shown for 10^7 events. 127

6.4 Fitted mass and yield for cases with a number of ρ^0 equal to 50%, 25% and 10% of the HIJING prediction for 10^6 central Pb-Pb events. The width is fixed at 140 MeV/c^2 for these fits. 128

6.5 Fitted values of ρ^0 mass, width and yield for pp collisions at 14 TeV. The number refers to the number per 1000 events, and only ρ^0s which have masses between 630 and 930 MeV/c^2 were included. 134

6.6 Fitted values of ρ^0 mass and width for generated and reconstructed ρ^0s, and a comparison to the generator input values. 138

6.7 Signal, background, significance and S/B values for ρ^0 in various p_t regions for the sample of 50 million PYTHIA pp events analysed. Significance is also shown for the expected 1 year total of 10^9 pp events. 139

Chapter 1

Theory

1.1 Introduction

Results from GeV/fm^3 high energy scattering experiments [1] have revealed that protons and neutrons, which make up nuclei, are composed of pointlike particles known as quarks. They are bound together by the strong interaction, which acts by gluon exchange as described by the theory of Quantum Chromodynamics (QCD). The strong interaction appears to have the property of *confinement*, which prevents free quarks from being observed and restricts strongly interacting matter to "colourless" combinations of quarks. Under normal conditions in nuclear matter, nucleons behave as separate, individual objects, with their internal structure not apparent. However, QCD predicts that a phase transition to a state of deconfined quarks and gluons will occur in hadronic matter at high temperature or density [2]. The goal of heavy ion experiments is to create and study this state of matter, known as the Quark-Gluon Plasma.

The study of this state of matter provides a test of QCD, particularly of the non-perturbative aspects of QCD which are not well understood, furthers the understanding of the behaviour of the strong interaction and has relevance to cosmology

and astrophysics [3, 4]. It is believed that the universe existed in a QGP state up to 10 microseconds after the Big Bang, and it is also suggested that neutron stars may provide suitable conditions for formation of a deconfined state due to the very high density of their cores [5].

1.2 Quantum Chromodynamics

The strong interaction is described by the theory of quantum chromodynamics (QCD) [6]. QCD has some similarities with the theory of the electromagnetic interaction, quantum electrodynamics (QED). QED describes the electromagnetic force as due to the exchange of massless, neutral photons, and QCD describes the strong force as due to the exchange of massless gluons. However, whereas the photon has no electric charge, the gluon carries strong (colour) charge. Therefore, unlike the photon, gluons can self-interact, which leads to the qualitatively different behaviour of the strong interaction.

1.2.1 Renormalization and running coupling constants

The amplitude for a particular interaction in a quantum field theory such as QED is conventionally calculated by applying perturbation theory, with the different terms conveniently represented by Feynman diagrams. For example, considering the first-order term only, the diagram for electron-muon scattering in quantum electrodynamics (QED) is shown on the left in figure 1.1. However, higher order terms exist, such as that shown on the right in figure 1.1. These higher-order diagrams must be taken into consideration if correct results are to be obtained from the theory. Furthermore, some of them are divergent, and lead to corrections of infinite size. Fortunately, these problems can be dealt with by a procedure known as renormalization.

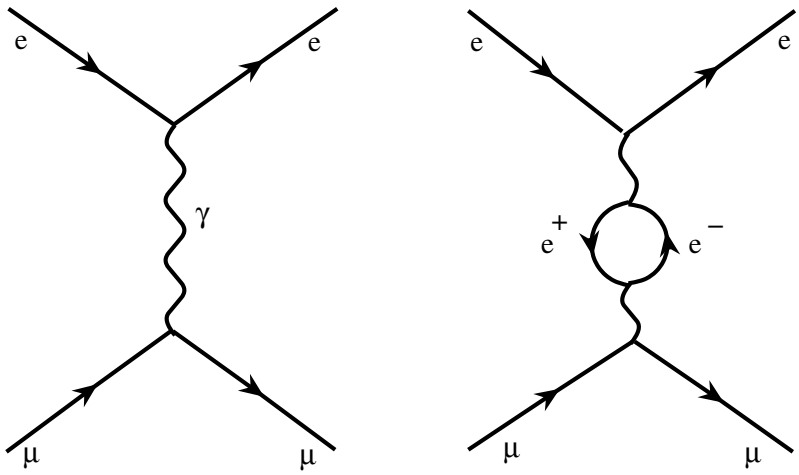

Figure 1.1: Feynman diagrams for electron-muon scattering, with the tree-level diagram on the left and a higher order correction from the vacuum polarization on the right.

Renormalization

The renormalization procedure contains a means by which the divergences can be removed. Typically, an upper limit is applied to the momentum that can be present in a loop such as that shown in figure 1.1, which makes its contribution finite. Then, a subtraction technique can be employed to allow a result to be calculated which is independent of the cutoff chosen [7]. The results from this procedure show that the effects of these higher-order diagrams can be understood in two equivalent ways:

- The effective charge of a particle is modified, and becomes distance dependent. This is interpreted as "screening" by particles produced from the vacuum, and as distance decreases, the screening effect is reduced. Screening can produce either a decrease or an increase in apparent charge, where charge refers to the electric charge for QED or colour charge for QCD.
- The coupling parameter, α_s is not constant, but depends on the momentum transfer in the interaction.

For the electromagnetic interaction, the modification of the coupling constant is relatively small - α_{em} increases from about 1/137 at low energy to about 1/130 at the Z^0 mass [7].

The running coupling constant α_s and asymptotic freedom

Similar higher order Feynman diagrams exist in QCD, for example, a quark may emit a gluon which forms a $q\bar{q}$ pair. However, the gluon self-interaction in QCD means that gluon loops can also exist, such as the loop shown in figure 1.2. These are

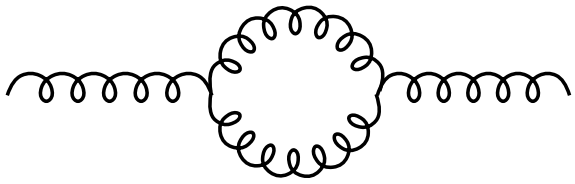

Figure 1.2: A gluon loop in QCD.

responsible for α_s decreasing rather than increasing with increasing Q^2 or decreasing distance [7]. As Q^2 becomes large, the effective α_s tends to zero as shown in figure 1.3. This is known as asymptotic freedom.

QCD predicts the energy dependence of the renormalized α_s, but not the value, which must be determined from experiment. However, once the value is known for a given energy, it can be calculated for any other energy. The scaling is approximately described by the equation:

$$\alpha_s = \frac{12\pi}{(33 - 2N_f)ln(\frac{Q^2}{\Lambda^2})} \tag{1.1}$$

where Q^2 is the 4-momentum transfer squared and Λ is known as the QCD scale parameter, which has been determined experimentally to be approximately 200 MeV [7].

The variation of α_s with distance or, equivalently, four-momentum transfer (Q) is of great importance in QCD physics. As shown in figure 1.3 [8], α_s is significantly

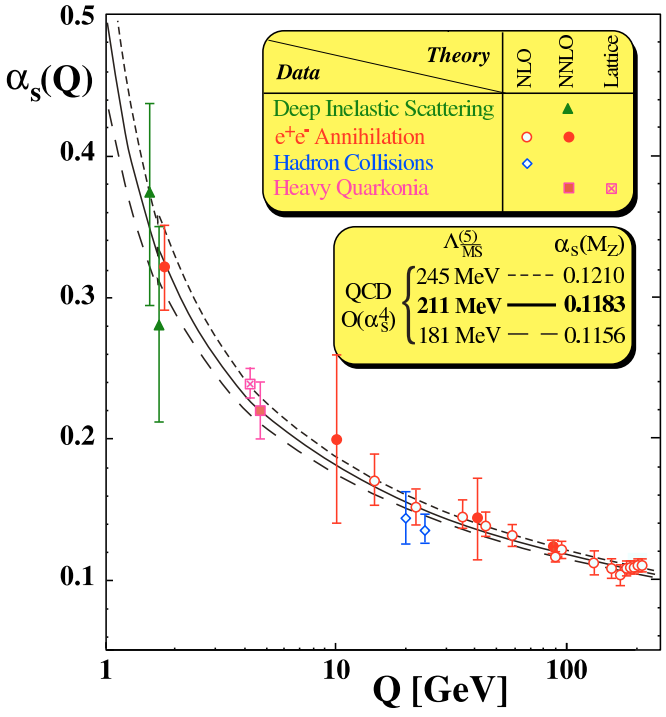

Figure 1.3: Variation of the strong interaction coupling parameter α_s with four momentum transfer Q.

smaller than 1 at high Q, and perturbation theory can therefore be applied, with the resulting physics resembling that of the electromagnetic interaction. The perturbative approach has been highly successful at predicting experimental results in the regime in which it is valid. However, at low Q, α_s is no longer small, and the perturbative approach as used for QED and high-energy QCD cannot be used, as higher order diagrams do not necessarily have smaller contributions than lower order diagrams. In this non-perturbative regime, the behaviour of quarks and gluons is qualitatively different and much less well understood, and appears to include features such as confinement, described below. Consequently, it can be expected that nuclear matter under conditions of low α_s will behave quite differently to nuclear matter under normal conditions. An indication of the energy scale at which α_s approaches 1, and therefore the point at which the theory becomes non-perturbative, is given by Λ.

These large values of α_s can be compared with the typical value and scaling behaviour of the electromagnetic coupling constant α_{em}, which is approximately 1/137 at low energy and increases slowly with Q^2. Non-perturbative effects are not seen in QED.

1.2.2 Calculations in non-perturbative QCD

Due to the difficulty in calculating the predictions of QCD in the non-perturbative regime, various phenomenological models and numerical techniques have been used.

The MIT bag model

The MIT bag model [9] is a model of a hadron in which the quarks are free inside the hadron and are confined by an external pressure which exists outside the hadron region. The pressure is included by including a scalar constant B with dimensions of energy density. Some results obtained from this model are described in section 1.3.

Lattice QCD

Lattice QCD is a numerical technique which has played an important role in non-perturbative QCD calculations. It involves defining the space-time integral of the Lagrangian on a discrete four dimensional space-time lattice [10]. It allows the calculation of quantitative results directly from QCD, and has allowed calculations relating to the QGP phase transition which were previously either not possible, or could only be obtained from models. Some of these predictions are described in section 1.3.1.

1.2.3 Confinement

Single photon exchange in QED leads to the familiar Coulomb potential, shown in equation 1.2.

$$V(r) = -\frac{A}{r} \tag{1.2}$$

The confinement of quarks to hadrons is believed to be a consequence of non-perturbative QCD. Lattice QCD calculations indicate that the potential between two quarks in the vacuum is of the form shown in equation 1.3 [11], which resembles the potential for QED but with an additional term which is proportional to separation.

$$V(r) = -\frac{A(r)}{r} + Kr \tag{1.3}$$

This can be interpreted as due to the gluon self-interaction causing the field lines to form a "flux-tube" rather than the dipole pattern seen in QED [12]. For small r, the first term dominates and the system behaves similarly to the electromagnetic case. At large r, the energy binding two quarks increases with separation until it is energetically favourable to form a new quark-antiquark pair. As a result, quarks are never observed individually but always as part of a 3 quark state, known as a baryon, or a quark-antiquark state, known as a meson.

1.2.4 Breaking of chiral symmetry

The QCD Lagrangian exhibits chiral symmetry - for the case of massless quarks, helicity is conserved and, for example, a left-polarized quark would remain so forever. However, in a quantum field theory, a symmetry can be broken spontaneously even if it is present in the Lagrangian. The vacuum state is the lowest energy state and this may correspond to a non-zero field. In QCD, the strong attraction between q and $\bar{q}$ means that the formation of such pairs in the vacuum is favourable, and therefore the vacuum state contains a $q\bar{q}$ condensate [13]. Chiral symmetry is spontaneously

broken in QCD due to the presence of this condensate. The $q\bar{q}$ pairs consist of a left-handed quark and its corresponding right-handed quark. A left-handed quark can annihilate with a left-handed antiquark from the vacuum, releasing its right-handed partner. Therefore, the quark appears to change chirality. This has the same effect as giving a mass to the quark, as only massive particles can change chirality in this way [14].

1.3 The Quark-Gluon plasma

Suggestions that nuclear matter may exist in a different phase under conditions of high density or temperature were made soon after asymptotic freedom was discovered [15]. These have been based on hadron models and thermodynamic arguments. More recently, numerical calculations have provided further reason to believe in a transition to a state of deconfined quarks and gluons. Some of the predictions are described below.

1.3.1 The Phase Diagram of QCD

A system of quarks and gluons can be considered statistically by considering a temperature, T, and a *baryochemical potential* μ, which is the energy required to add a baryon to the system. The baryochemical potential is proportional to the net baryon density of the system per unit volume [2]. An independent variable is required for baryon content as baryon number must be conserved, so equilibrium systems cannot be completely defined by their temperature. The system produced in a heavy ion collision may have a positive net baryon density due to the baryons present in the initial colliding ions.

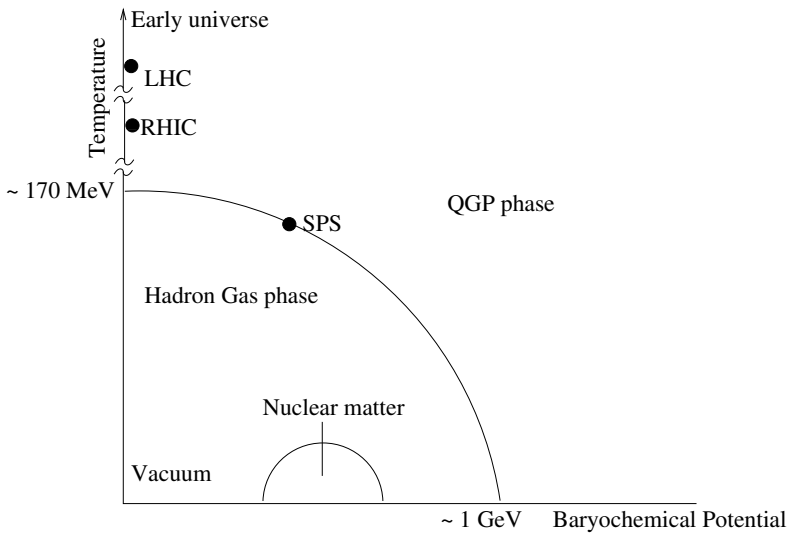

Figure 1.4: A simple phase diagram of QCD, obtained from the Bag Model, with a rough indication of conditions reached at the Super Proton Synchrotron (SPS), the Relativistic Heavy Ion Collider (RHIC) and the Large Hadron Collider (LHC). The values of T_c at $\mu = 0$ and μ_c at $T = 0$ are shown on the axes. These were obtained from lattice QCD calculations, and are about 170 MeV for T_c and about 1 GeV for μ_c.

Predictions of the Bag Model

The MIT bag model can be used to predict the shape of the phase boundary, and to provide an estimate of the critical T and μ. A state of a weakly interacting gas of free, massless u and d quarks and gluons is considered. Confinement is incorporated by including a negative pressure B given by the bag constant. Also present is the ground state energy and the pressure due to thermal excitation. As the temperature and density of the particles in the bag increases, the pressure increases. At certain values of T and μ, the pressure inside the bag will become greater than the external, confining pressure, and a transition to the deconfined phase will occur. This set of values for T and μ forms the phase boundary. The critical temperature calculated by this model for μ=0 is between 100 and 200 MeV for typical values of the bag constant [16]. The shape of the phase diagram obtained from this model is shown in figure 1.4.

The results described above are obtained considering a simplified model of hadrons. A more rigorous set of predictions can be obtained using lattice QCD. Results from lattice QCD suggest a phase transition to a state of deconfined quarks and gluons at a temperature of approximately 170 MeV and energy density of the order of 1 GeV/fm^3 [17]. Figure 1.5 [17] shows the energy density divided by the fourth power of temperature as a function of temperature. For blackbody electromagnetic radiation, the quantity ϵ/T^4 is a constant. The lattice results shown in figure 1.5 indicate that a rapid increase in ϵ/T^4 occurs at about 170 MeV, and that the quantity stays constant above this. This suggests an increase in the number of degrees of freedom of the system, i.e. a transition from hadrons to deconfined quarks and gluons. However, as shown in figure 1.5, the value that is reached is less than the Stefan-Boltzmann value for ideal behaviour, indicated by the arrows on the right of figure 1.5. This suggests that there are still interactions between quarks and that they are not totally free particles.

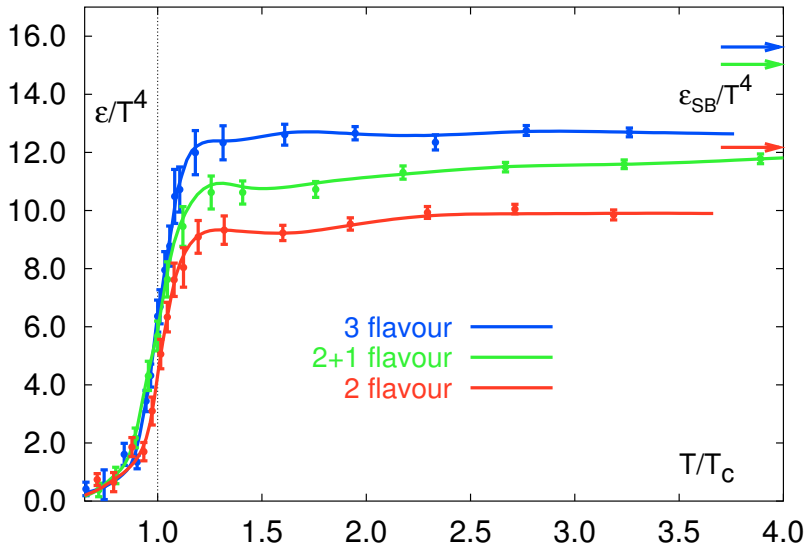

Figure 1.5: Energy density divided by the fourth power of temperature as a function of temperature, obtained from lattice QCD calculations. The values for ideal Stefan-Boltzmann behaviour are shown by the arrows on the right.

Lattice QCD has also provided information on the phase boundary in μ and T. The transition is expected to occur, for $\mu = 0$, at a temperature of about 170 MeV. For T=0, the transition occurs at a μ of the order of 1 GeV [18].

1.3.2 Chiral symmetry restoration

The transition to the QGP phase is expected to result in the partial restoration of chiral symmetry. As conditions move into the perturbative region of QCD, the formation of the $q\bar{q}$ condensate becomes unfavourable. Results from lattice QCD indicate that the value of $< \bar{\psi}\psi >$ drops rapidly around a critical temperature, which coincides with the temperature at which deconfinement appears to occur [13].

As the chiral symmetry breaking in QCD is responsible for most of the quarks' masses, its restoration will result in a decrease of the quark masses to their "bare" values. These values are a few MeV/c^2 for the u and d quarks and about 80-150 MeV/c^2 for the strange quark [19].

1.3.3 Conditions under which the QGP may exist

The Universe immediately after the Big Bang is believed to have been in a state of high T and low μ, as the number of particles and antiparticles was nearly equal. These conditions are also probed by the higher energy heavy ion collisions. In lower energy heavy ion collisions, some of the quarks in the colliding nucleons are present in the central fireball and, therefore, there is an asymmetry between particles and antiparticles. Neutron star cores have a very high density, so there is the potential for the formation of a deconfined state of matter at high baryochemical potential and low temperature [5].

1.4 Heavy Ion Collisions

1.4.1 QGP in Heavy Ion Collisions

A Pb-Pb collision at sufficiently high energy should result in the formation of the QGP. Heavy ions such as lead are preferred as the resulting fireball is larger and longer lived than for lighter ions. After formation, the QGP fireball expands and cools rapidly due to its very high pressure. This happens at a speed of the order of the speed of light [2]. The timescale of interactions is, therefore, on the same scale as the time taken for light to travel the radius of a nucleus, which is of the order of 10^{-23} seconds. The exact timescale depends on the energy of the collision, and is expected to be longer at the LHC than at the SPS. It is expected this is sufficient time for the quarks and gluons to reach thermal equilibrium [2]. When the fireball has expanded and cooled, the system undergoes a phase transition to the hadron gas phase, and the quarks and gluons enter a confined state and form hadrons. After the transition to a hadron gas, further development can be characterised by two freezeout stages - chemical freezeout, where inelastic collisions cease, and thermal freezeout, where all interactions between particles cease.

The fireball lifetime is too short for direct observation, but a number of signatures of the QGP have been proposed, some of which are described in section 1.5.

1.4.2 Heavy Ion Kinematics

It is useful to define the variable *rapidity* as shown in equation 1.4, where E is the energy of a particle and p_l is its longitudinal momentum.

$$Y = \frac{1}{2} \ln \left[\frac{E + p_l}{E - p_l} \right] \tag{1.4}$$

The rapidity is a quantity which is shifted by a fixed amount under a longitudinal Lorentz boost. The shape of a rapidity distribution is unchanged by transformation

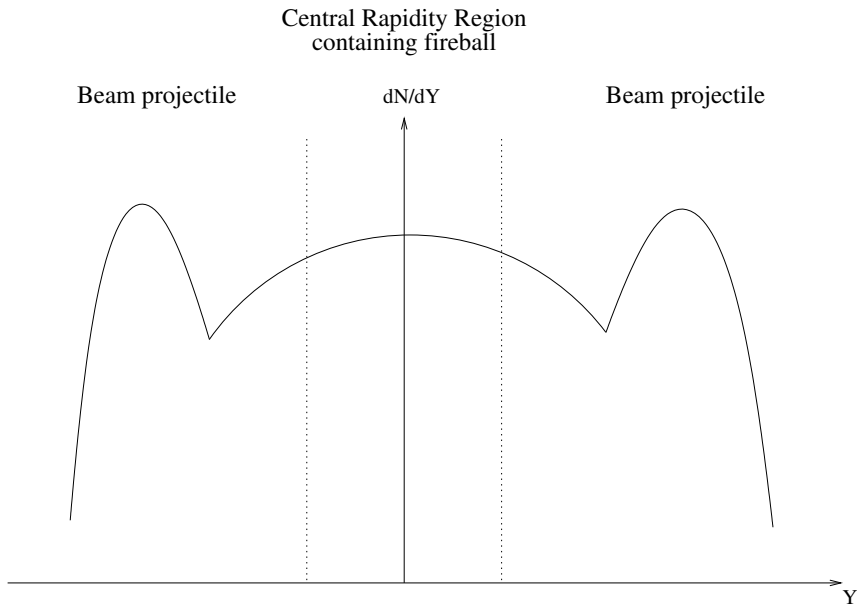

Figure 1.6: A simple model of the rapidity distribution of particles in the centre of mass frame for a heavy ion collision, with the QGP fireball at central rapidity and the projectile fragmentation regions at high rapidity.

between frames. Figure 1.6 gives an approximate rapidity distribution for a heavy ion collision at a colliding beam experiment. The QGP is expected to be formed in the central rapidity region, and the two peaks at large positive and negative rapidities are related to production associated with the projectile nuclei.

A fixed target experiment's rapidity distribution in the lab frame will have the same shape but will be shifted to positive rapidity. For higher energy beams, the difference in rapidity between the ions is larger. The large peaks at the sides are due to particle production in the projectile nucleons, which continue at somewhat reduced energy after the collision. The QGP fireball is produced at central rapidity, so it is this region which is of most interest. The WA97 [20] and NA57 [21] experiments were designed to study the central rapidity region.

The quantity *pseudorapidity* is sometimes used, particularly when discussing detector acceptance and efficiency. It is approximately equal to rapidity for highly

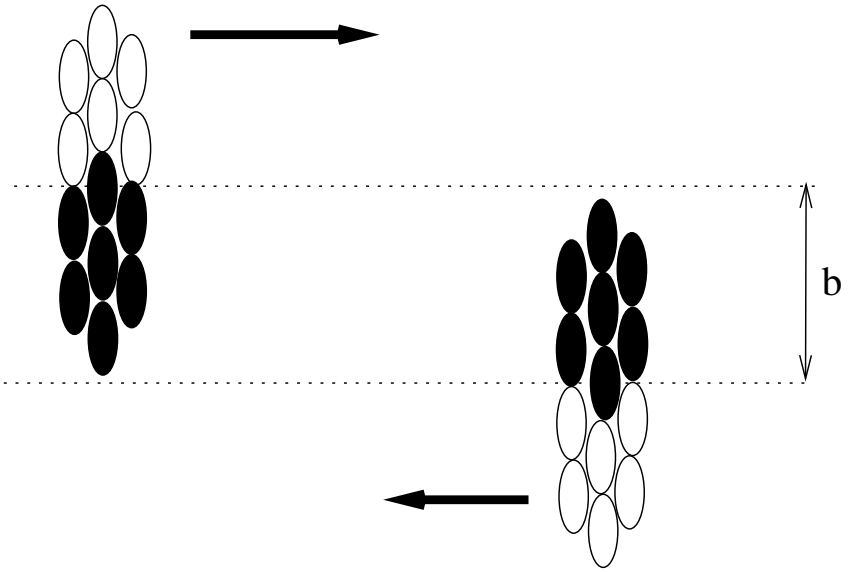

Figure 1.7: An example of a collision of two lead nuclei with impact parameter b. The "wounded nucleons" are shaded in black.

relativistic particles, and is defined as:

$$\eta = \frac{1}{2} \ln \left[\frac{p + p_l}{p - p_l} \right] \tag{1.5}$$

which is equivalent to:

$$\eta = -\ln \left[\tan \left(\frac{\theta}{2} \right) \right] \tag{1.6}$$

where θ is the angle relative to the beam axis. Therefore, the pseudorapidity is a function of angle only, and hence can be readily related to the detector geometry.

Collisions between two large ions rarely involve all the ions' nucleons, as demonstrated in figure 1.7. It is the central rather than peripheral collisions which result in conditions suitable for QGP formation, as peripheral collisions are less likely to produce suitable temperatures and energy densities, particularly at the relatively low collision energies at the SPS. The centrality of a collision is related to the number of "wounded nucleons", i.e. the number of primary collisions. By looking at the variation of QGP signatures with centrality, the onset of QGP can be investigated.

1.4.3 Heavy Ion Experiments

Many experiments have searched for the QGP by studying heavy ion collisions. Fixed target programmes have existed at the Brookhaven AGS and the CERN SPS. More recently, experiments at the RHIC colliding beam facility have made use of Au-Au collisions with a centre of mass energy an order of magnitude larger than at the CERN fixed target experiments. Some relevant SPS experiments were:

- WA97 and NA57 [21] which investigated strangeness enhancement. Some results from these experiments are presented in this thesis.
- NA49, which also studied strangeness enhancement over a wider acceptance but with lower statistics.
- NA45 [22], which investigated dielectrons and, for later runs, charged hadrons.
- NA50, which investigated J/Ψ suppression by measuring dimuons.
- WA98, which investigated direct photons.

Pb-Pb collisions at the SPS energy are thought to have probed the phase boundary for the QGP transition, shown in figure 1.4. Signatures such as strangeness enhancement and J/Ψ suppression, described in detail below, were visible.

The factor of 10 increase in centre of mass energy available at RHIC should result in conditions above the phase boundary. In addition, hard probes are produced in sufficient quantity to allow their use in QGP investigations. For example, "jet quenching" has been observed [23], where the energy of high p_t particles is absorbed in the medium. The RHIC experiments are STAR [24], PHENIX [25], PHOBOS [26] and BRAHMS [27].

ALICE at the CERN LHC is a multipurpose detector designed to investigate the full range of QGP signals [28]. The LHC will collide lead ions at a centre of mass

energy of 5.5 TeV per nucleon. The resulting fireball is expected to be far larger, hotter and longer lived than that at the SPS or RHIC, and will result in a much larger number of particles produced per collision [29]. Hard probes will be produced in abundance, and signatures such as direct photons should be measurable.

1.5 Signatures of the Quark-Gluon Plasma

1.5.1 Introduction

The QGP state cannot be observed directly, but various observable signatures have been proposed which would indicate the formation of a QGP and allow its study. The observables of particular relevance to the analysis described later are weakly decaying strange particles, for measuring strangeness enhancement, and strongly-decaying resonances. These are described in detail below. Some other signatures for which results have been obtained are described more briefly.

1.5.2 Strangeness enhancement

Enhanced production of strange baryons such as the Λ (uds) or Ξ (dss) is predicted if a QGP is formed in heavy ion collisions [30]. As a consequence of chiral symmetry restoration in the QGP, described in section 1.2.4, the masses of the quarks reduce to their bare values. The mass of the strange quark reduces from around 550 MeV/c^2 to between 80 and 150 MeV/c^2. The temperature of the QGP transition, by contrast, is believed to be over 150 MeV, and so abundant and rapid production of $s\bar{s}$ pairs should take place by reactions involving free quarks and gluons, for example:

$$gg \rightarrow s\bar{s} \tag{1.7}$$

The Feynman diagram for this process is shown in figure 1.8. Strangeness production is expected to approach equilibrium within the lifetime of the fireball [30]. As

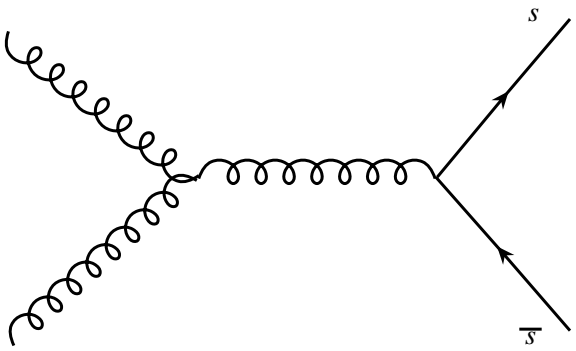

Figure 1.8: Feynman diagram showing strange quark production by gg fusion.

the plasma expands and undergoes a transition back to the hadron gas state, hadronisation occurs and the strange quarks appear in strange hadrons such as K^0s and Λs. Strangeness is conserved as the fireball lifetime is too short for weak interactions to occur.

By contrast, in the non-QGP scenario, production must proceed via hadronic channels such as:

$$pp \rightarrow pK^+\Lambda \tag{1.8}$$

This requires an energy input of approximately 700 MeV, as compared to about 300 MeV required for the process shown in equation 1.7 with a strange quark mass of 150 MeV/c^2. This means that the production of strangeness in a hadronic system is much slower, as few of the colliding particles will be sufficiently energetic, further reducing the strangeness produced, particularly in lower energy collisions such as at the SPS. This effect is even larger for doubly and triply strange particles such as Ξ and Ω, as a series of interactions is necessary to produce them.

To allow the change in strangeness to be measured, an *enhancement* factor was defined. The yield of a species of strange particle, such as Λ, in a Pb-Pb collision was divided by the number of projectile nucleons which participate in the collision, known as *wounded nucleons*. The number of wounded nucleons is larger for a more central collision. The result was then normalised to the yield of that strange particle species per wounded nucleon in the reference p-Be collision.

This strangeness enhancement in the QGP can be observed by measuring the yields of particles containing strange quarks, such as the Λ (uds), Ξ (dss) and Ω (sss). This model predicts that the degree of enhancement will increase with increasing strangeness content, so the enhancement for Ξ is expected to be greater than the enhancement for Λ.

Production of particles of higher strangeness should be enhanced more in the QGP than those of lower strangeness, and therefore a "hierarchy" should be observed, with doubly strange particles such as Ξ^- being enhanced more than singly strange particles such as Λ^0.

Quarks are fermions, and so are subject to the Pauli exclusion principle. Production of a large number of identical quarks in a small region is therefore suppressed, as the quarks must be produced in higher energy states. This makes strangeness production in the QGP even more favourable than would be expected from chiral symmetry restoration alone. This effect, known as Pauli blocking, is larger for lower energy collisions, such as those at the SPS, where the fireball contains a significant fraction of the quarks from the original nucleons [30].

Strangeness enhancement in Pb-Pb collisions has been confirmed by the WA97 experiment at a beam energy of 158A GeV/c. The results are shown in figure 1.9 [31]. As expected, enhancement is present for all strange particle species, with enhancement increasing with increasing strangeness, which agrees with predictions for strangeness production in a QGP.

Strangeness enhancement has also been observed in Au-Au collisions at the STAR experiment at RHIC at a centre of mass energy of 200 GeV per nucleon. The results are shown in figure 1.10 [32]. The observed enhancements are similar for STAR and NA57, with the exception of the $\bar{\Lambda}$.

Strangeness enhancement is also expected to be observed for the LHC, as it has been at the SPS and RHIC. Measurements at ALICE will investigate enhancements

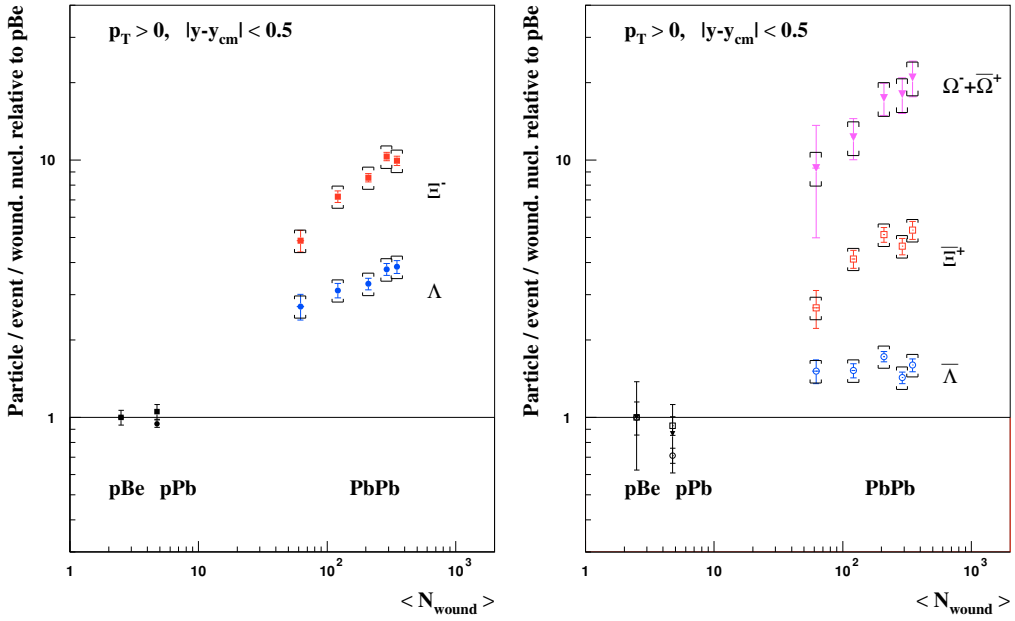

Figure 1.9: Enhancement of strange baryon production in 158A GeV/c Pb-Pb collisions at the WA97 experiment, normalised to the yield in 158 GeV/c p-Be collisions.

in hotter and longer lived systems than have previously been created.

1.5.3 Canonical suppression

It has been suggested that an enhancement of strange particle production will be present in heavy ion collisions even in the absence of a QGP due to the increase in system size [33]. A large system may be modelled using the grand canonical ensemble, where conservation laws are true on average. For small systems, the canonical ensemble must be used, and this introduces a suppression factor which is a function of temperature and volume. As the system becomes larger and hotter, the difference between the canonical and grand canonical predictions tends towards zero. It has been suggested that this effect can account for the observed enhancement without assuming a Quark-Gluon Plasma.

However, the canonical suppresion model predicts a decrease in strangeness en-

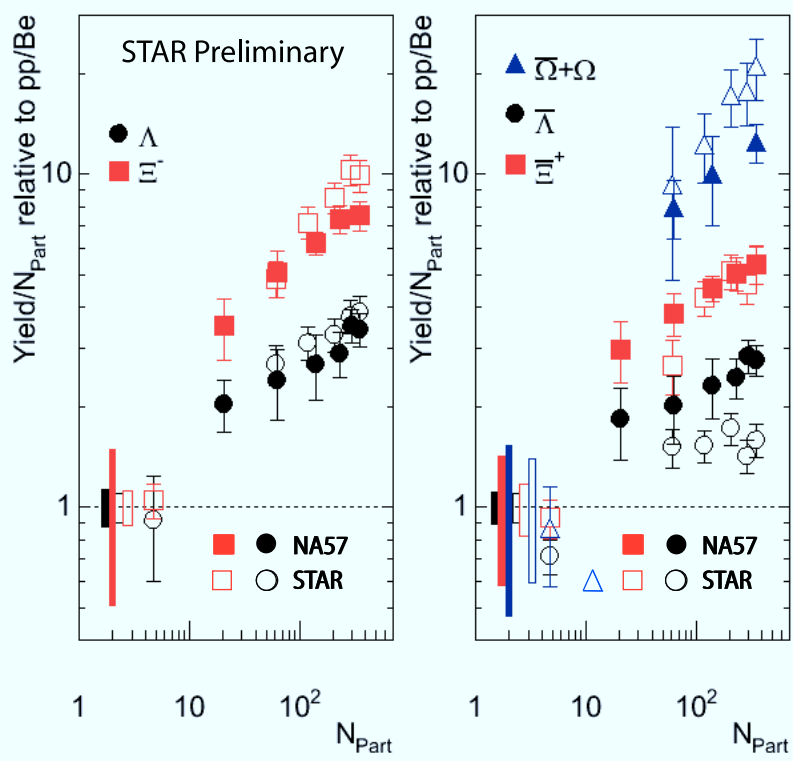

Figure 1.10: Comparison of strange particle enhancements in heavy ion collisions at STAR and NA57. N_{Part} refers to the number of participant nucleons, where "participant nucleon" is defined in the same way as "wounded nucleon", which is the term used elsewhere.

hancement with collision energy. For example, it predicts a significantly lower enhancement for the high energy SPS result than for the low energy SPS result, as shown in figure 1.11 [33]. However, the observed enhancements are similar for all energies [34]. Additionally, it predicts an enhancement which is independent of number of participants for N_{part} greater than 100, whereas the data indicates an increase in enhancement with increasing centrality. Given these discrepancies, this model does not appear to account for the observed enhancement, and so strangeness enhancement can still be considered a valid piece of evidence supporting the formation of a QGP.

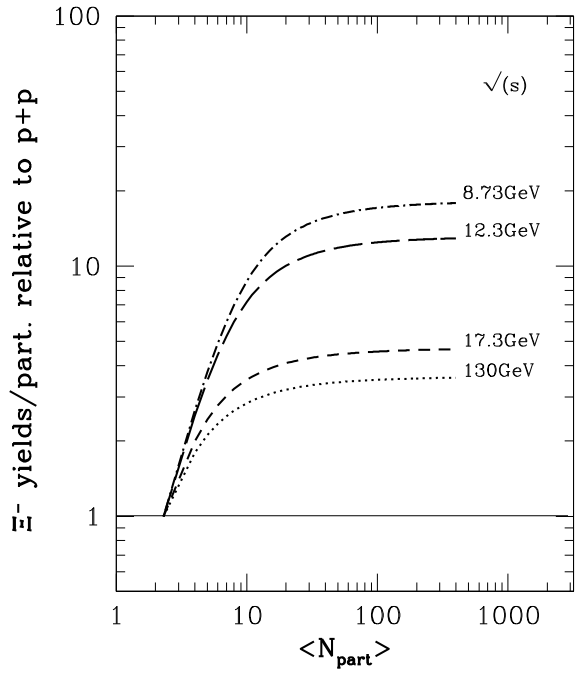

Figure 1.11: Canonical suppression model prediction of centrality dependence of Ξ^- enhancement in Pb-Pb collisions at different collision energies.

1.6 Resonances as QGP probes

1.6.1 Introduction

The weakly decaying strange particles, described above, can provide some information about the state of matter created in the collision. However, there is the potential for additional information to be obtained by studying particles with lifetimes similar to the lifetime of the fireball. Strongly-decaying resonances such as the ρ^0, ϕ or K^{0*} satisfy this requirement. As they can decay inside the medium, different information can be obtained than from longer lived particles. For example:

- Their decay particles may be rescattered in the medium, reducing the observed yield. This magnitude of this rescattering depends on the properties of the medium.

- The resonance mass, width or line shape may be modified in the medium. The nature and size of such modification may provide information on the conditions produced in the collision.

These are described in more detail below.

1.6.2 Daughter particle rescattering

The measured yield of resonances is sensitive to properties of the medium. The decay tracks from a resonance decay are produced in a dense environment, and so they may undergo scattering. If this occurs, the reconstructed invariant mass for the resonance that produced the tracks will be incorrect, and so the resonance signal will be "smeared out". The magnitude of this rescattering depends on the nature of the medium, the nature of the decay particles, the density of the medium and the time scale involved.

Resonances which are composed of a quark and its anti-quark, e.g. ρ and ϕ can decay into dileptons as well as by the much more likely hadronic channel. Leptons do not couple to the strong interaction, so rescattering must be electromagnetic and is therefore expected to occur at a much lower rate. Therefore, the degree of daughter particle rescattering is expected to be much lower for the leptonic decay channel. Consequently, this channel can, in principle, be used to measure the total resonance yield, and to probe all stages of the interaction. By contrast, the hadronic channel can only allow reconstruction of resonances from the later stages of the system. Therefore, the observed ρ^0 yield may depend on the decay channel.

1.6.3 Modification of resonance properties in a medium

Particle properties such as mass, width and line shape may depend on the particle's environment, and so may be modified from their values in the vacuum. Particles

with short lifetimes, therefore, may allow the observation of modifications due to the medium created in a heavy ion collision. Various mechanisms which can cause observable modifications have been proposed. For example, the restoration of chiral symmetry may reduce the ϕ mass, giving rise to an additional peak at lower mass in the dilepton invariant mass spectrum [35].

There have been various theoretical predictions of the effects of the phase transition on the ρ^0 mass. Increase in the width is a common feature [36, 37, 38, 39, 40, 41], but predictions of the mass under such conditions vary. Predictions of a decrease [36, 42], an increase [38] and no change [39, 40] all exist.

Measurements of resonances which decay earlier on in the more extreme conditions may be carried out using the leptonic decay channel, whereas the hadronic channel allows the measurement of resonance properties in the later, more dilute stages of the system. Additionally, the observed resonances come from different times of the fireball depending on their lifetime [43]. Therefore, the properties of longer-lived resonances will reflect later stages of the collision system than those of shorter-lived resonances.

1.6.4 Resonances as a probe of time evolution of the fireball

Resonances can provide information about the later states of the evolution of the collision system. Statistical models have been used to fit the observed yields of resonances and long-lived particles. The yields of long-lived particles are well described by a statistical model, but yields of resonances are not [44]. This can be explained by the short lifetime of the resonance. The relative abundances of particle species are determined by conditions at chemical freezeout. However, further interactions may take place after chemical freezeout but before thermal freezeout. If a resonance decays in this region, its decay tracks may be rescattered and the observed yield will be lower. Similarly, regeneration of resonances from these interactions may act to

increase the observed yield [44, 43]. Measurements of resonance yields can therefore be used to investigate the time between chemical and thermal freezeout.

1.6.5 Previous resonance results

Measurements of $\rho^0(770)$

The NA60 experiment at the CERN SPS has measured $\rho \to \mu^+\mu^-$ in In-In collisions of varying centrality with a beam momentum of 158 GeV/c per nucleon [45]. After the subtraction of combinatorial background and known meson decays, the ρ peak is clearly visible. A broadening of the ρ is observed when going from peripheral to

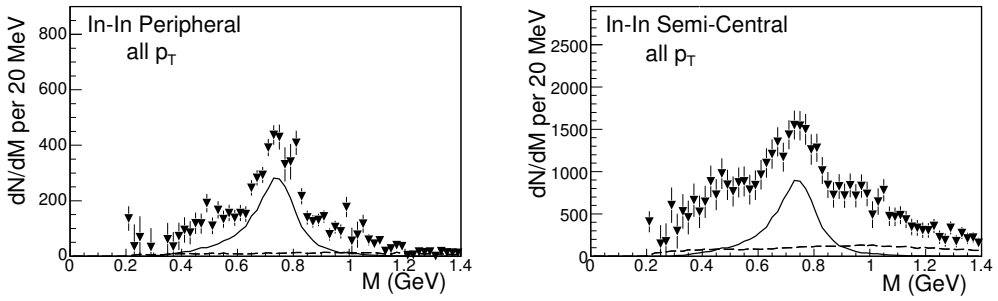

Figure 1.12: Comparison of excess dimuon mass spectra at NA60 after subtraction of background and known meson contributions. The left plot shows the ρ^0 in peripheral In-In collisions, and the right plot suggests a broadened ρ in more central collisions.

more central collisions, as shown in figure 1.12 [45], but there is no indication of a mass shift. The results are most consistent with the Rapp/Wambach in-medium broadening of the ρ^0 [45, 39, 40].

The STAR experiment at RHIC has measured $\rho \to \pi^+\pi^-$ in p-p and peripheral Au-Au collisions [46]. A mass reduction of 70 MeV/c^2 is observed in Au-Au collisions at low p_t, compared a mass reduction of 40 MeV/c^2 in pp as shown in figure 1.13 [46]. The mass shifts appear to reduce at large p_t, which is consistent with a greater

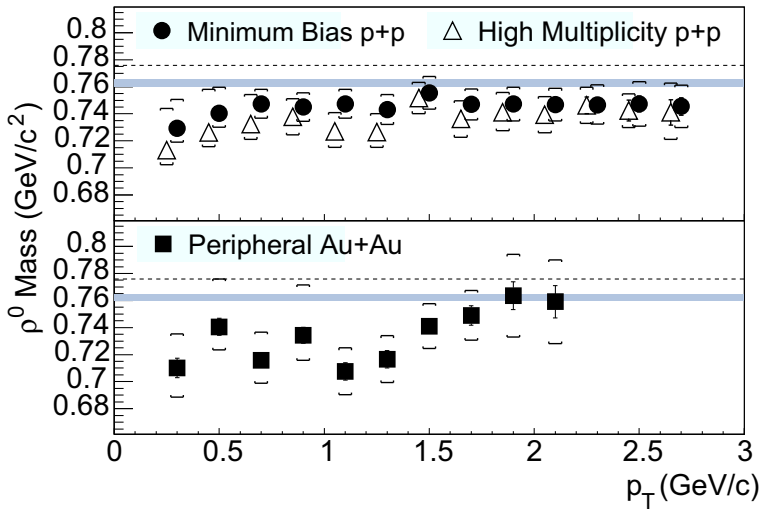

Figure 1.13: ρ mass as a function of transverse momentum, as measured in the $\pi^+\pi^-$ decay channel at the STAR experiment.

probability of the ρ decaying later and in less extreme conditions. However, there is no explanation as to why the measured ρ^0 mass in pp collisions is so different from that measured at other experiments. Until this is clearly understood, this result should not be considered conclusive.

The NA45 experiment measured dielectrons in heavy ion collisions at the CERN SPS, and observed an enhancement of low-mass e^+e^- pairs [47, 48]. Modification of the ρ^0 was suggested as an explanation, and the results were compared with models for ρ^0 modification [48]. However, no clear interpretation was apparent.

Measurements of ϕ

The NA49 experiment has measured ϕ production in the $\phi \to K^+K^-$ channel [49], and the NA50 experiment has measured it in the $\phi \to \mu^+\mu^-$ channel [50]. The yield of the ϕ measured in the dilepton channel, after correction for branching ratio, is larger, by a factor of two to four, than the number measured in the hadronic channel. If correct, this supports the idea of daughter re-scattering.

The NA45 experiment has measured ϕ production in Pb-Au collisions at the SPS in both hadronic and leptonic decay channels [51]. The measured yield was the same in both channels, and is consistent with the result measured at NA49 but inconsistent with the result from NA50 [51].

The PHENIX experiment has measured ϕ production in the K^+K^- decay channel at RHIC in Au-Au collisions at a centre of mass energy of 200 GeV per nucleon [52]. No deviation of ϕ mass or width from the PDG values was observed.

The set of results which have been obtained for the ϕ so far do not lead to any conclusive interpretation. A particular problem is the inconsistency between the NA50 result and those from NA45 and NA49. PHENIX's observation of an unchanged mass or width as measured by the hadronic channel is contrary to some predictions [52], but the hadronic channel can only investigate the later stages of the collision.

1.6.6 Other signatures

Jet quenching

The initial interactions in a high energy collision may result in the formation of high momentum quarks. As quarks are confined under normal conditions, they will then fragment into hadrons, with the momentum of the resulting group of hadrons being equal to the momentum of the initial quark. Therefore, a high momentum quark produced in a collision appears as a "jet" of particles. The requirement for the conservation of momentum means that jets are formed back-to-back in ϕ.

A quark-gluon plasma consists of a large density of colour charges. A coloured object passing through this medium will lose energy by gluon radiation, in the same manner as an electrically charged particle passing through a region of dense electrical charges will lose energy via bremsstrahlung [53]. Therefore, a high-p_t coloured

particle will lose energy as it travels through the QGP medium, and consequently the momentum of the resulting jet will be reduced. Therefore, suppression of jet production may indicate QGP formation. In the hadron gas medium, the hadrons are colourless and so the energy loss is expected to be much weaker. Model predictions suggest that the energy loss in a QGP is an order of magnitude larger than in cold nuclear matter [53].

Results from the STAR experiment suggest that such suppression is present in central Au-Au collisions. The highest p_t particle in an event is selected and defined to be at $\phi = 0$. The distribution of the angles of the other particles satisfying a minimum p_t criterion is shown in figure 1.14 [54]. It can be seen that the number of high p_t particles with ϕ around 180 degrees is greatly reduced in central Au-Au collisions. This could be a result of the away-side jet travelling further through the medium and consequently losing its energy, and appearing as particles with p_t too low to be included in figure 1.14. Additionally, measured values of the normalised production of tracks in central Au-Au collisions show a suppression relative to d-Au which is particularly marked at high p_t [54].

J/Ψ suppression

A quark-gluon plasma contains a high density of colour charges. In such a medium, a quark will effectively see a reduced colour charge from a distant quark due to the effect of Debye screening [55]. The J/Ψ is a meson consisting of $c\bar{c}$ and has a large binding radius. If the Debye screening length is small compared to the binding radius, the c and $\bar{c}$ quarks will effectively no longer see each other and the bound state will break up. At SPS energies, the high mass of the charm quark means that little production takes place in the QGP, and so almost all of them are produced in the initial collision. It has been therefore been suggested that, if a QGP is formed, the J/Ψ yield will be suppressed relative to the yield in elementary particle collisions [55].

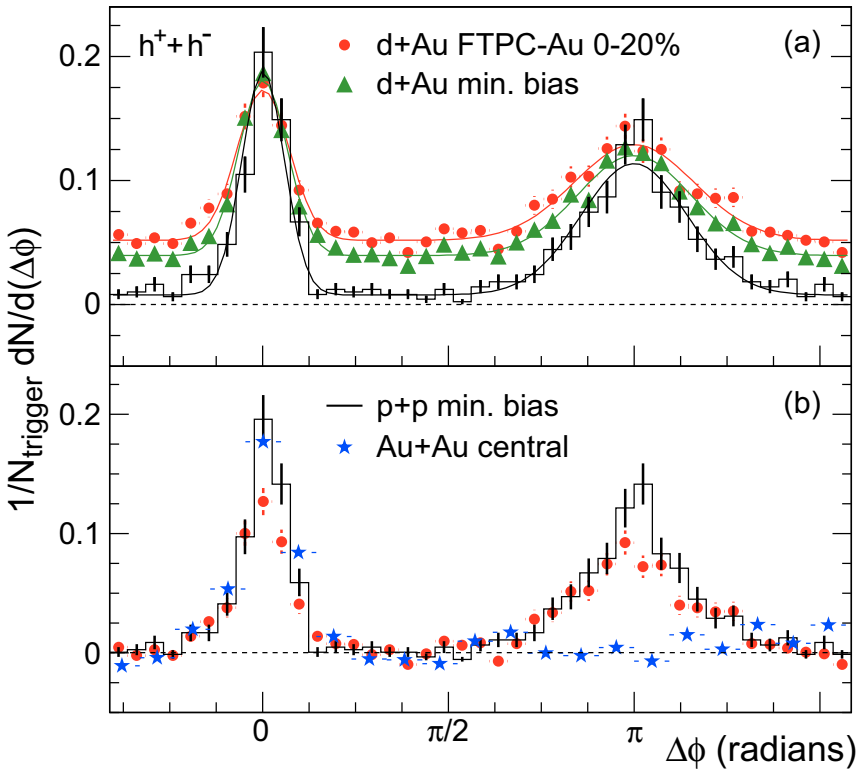

Figure 1.14: Azimuthal distribution of high-p_t particles measured at the STAR experiment, showing the disappearance of the corresponding "back-to-back" peak in central Au-Au collisions.

The NA50 experiment has measured J/Ψ in heavy ion collisions in the dimuon channel. It was observed that J/Ψ production was suppressed in heavy ion collisions in moderately central to central collisions, as compared to a pp reference [56].

Chapter 2

Experiment

2.1 The CERN accelerator complex

The particle physics laboratory CERN has a complex of particle accelerators of varying energies. These produce beams for use directly in fixed target experiments or to feed into other accelerators for further acceleration and collision. This network of accelerators is shown in figure 2.1. For the analyses in this thesis, the Super Proton Synchrotron (SPS) and Large Hadron Collider (LHC) are of primary interest, and acceleration of both protons and lead ions is of importance.

Acceleration of protons begins in a linear accelerator, LINAC 2, shown in figure 2.1. After acceleration to 50 MeV/c, the protons are fed into the Proton Synchrotron Booster (PSB) and then into the Proton Synchrotron (PS). On leaving the PS, the protons are sent to the SPS, which is described in the next section.

Acceleration of lead ions begins in LINAC 3. At this stage, the ions are only partially stripped of electrons. After leaving LINAC 3, the ions are passed through a metal foil to further strip electrons from the lead ions, resulting in Pb^{+53}. As for protons, the ions are then passed through the PSB and the PS, and on leaving the

PS are passed through a final stripper foil, which produces the fully stripped ions [57]. They are then injected into the SPS for further acceleration.

2.1.1 The Super Proton Synchrotron (SPS)

The SPS is a proton and heavy ion accelerator with a 9 km circumference, capable of accelerating protons to a momentum of 450 GeV/c and lead ions to a momentum of 158 GeV/c per nucleon.

It has been used as a collider in itself, known as the $Sp\bar{p}S$, as an injector for other accelerators such as the Large Electron-Positron Collider (LEP) and the Large Hadron Collider (LHC) and as a beam source for fixed target experiments in the North Area and West Area experimental halls as shown in figure 2.1. The NA57 fixed target experiment, based in the North Area, used the proton and lead beams from the SPS.

2.1.2 The Large Hadron Collider (LHC)

The LHC is a high energy hadron collider at CERN, and will produce both proton-proton and heavy ion collisions. The energy of the p-p collisions, 14 TeV, is more than 7 times as large as at the Tevatron, the next highest energy p-p collider. The energy of the Pb-Pb collisions, 5.5 TeV per nucleon, is more than 25 times larger than the energy of the Au-Au collisions at RHIC.

Accelerated protons or ions are transferred from the SPS to the LHC ring, as shown in figure 2.1. The particles circulate in the LHC, guided by superconducting magnets which produce an 8.4 T field, and are accelerated further to their final energy. Collisions are produced at four interaction points. The detectors are constructed around these interaction points, and are marked on figure 2.1 as ALICE [58], ATLAS [59], CMS [60] and LHC-b [61]. Close to the interaction points, quadrupole

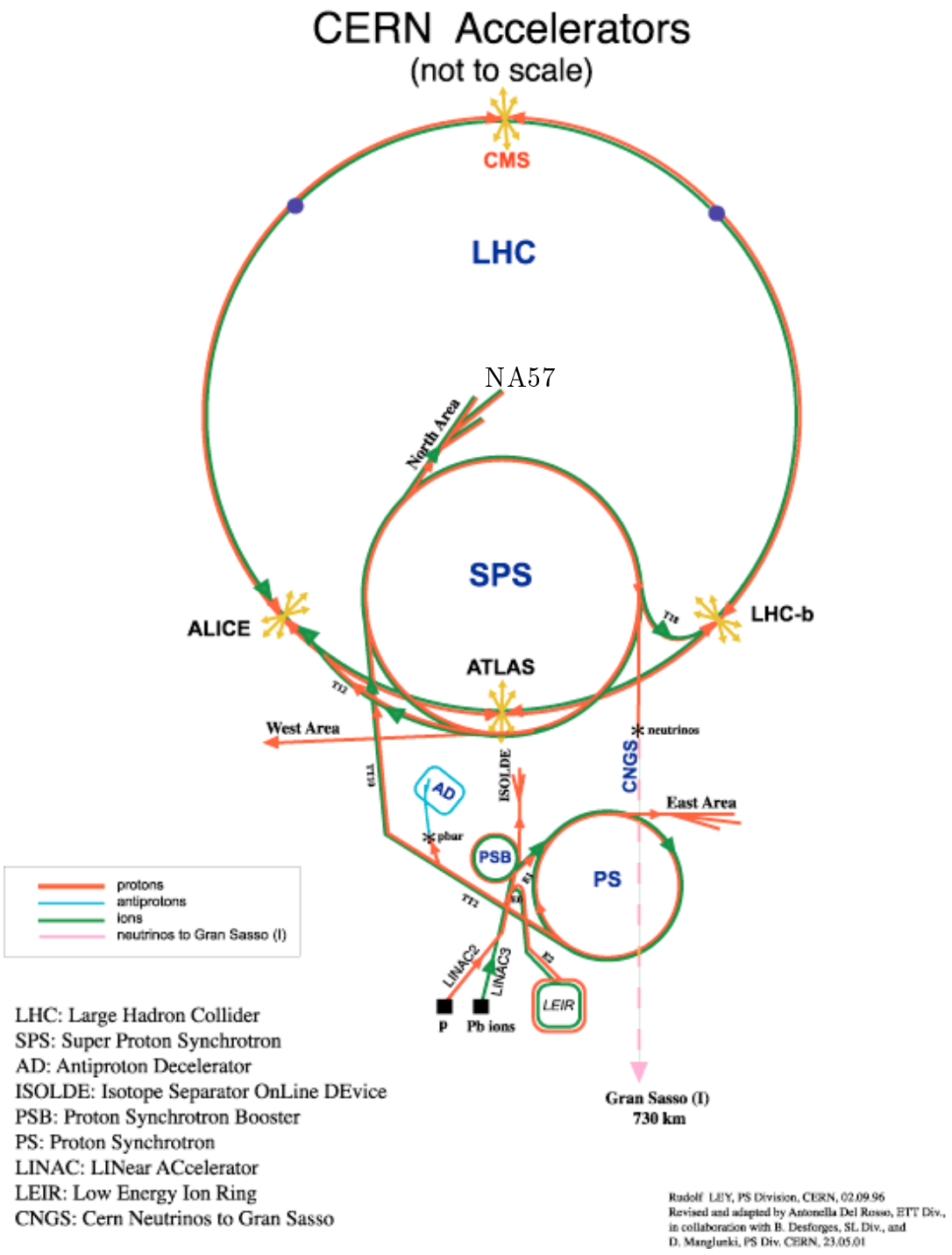

Figure 2.1: The CERN accelerator complex.

magnets are used to focus the beams into a small cross-sectional area to increase the probability of interaction. Table 2.1 shows some of the expected collision systems, energies and luminosities that will be produced at the LHC.

Table 2.1: Some collision systems studied at the LHC.

Collision system	Energy	Luminosity / $cm^{-2}s^{-1}$
pp	14 TeV	10^{34} (ATLAS/CMS)
pp	14 TeV	$\leq 3.0 \times 10^{30}$ (ALICE) [62]
Pb-Pb	5.5A TeV	$\sim 10^{27}$ [62]

ATLAS and CMS are primarily intended to search for previously undiscovered heavy particles, such as the Higgs boson and supersymmetric particles. LHC-B is a dedicated B physics experiment designed to look for CP violation by studying B meson decays. These experiments primarily study proton-proton collisions. ALICE is primarily intended for the study of heavy ion collisions, but it will also be used to study pp collisions, and is described in section 2.3. Proton-proton collisions will be studied at ALICE to use as a comparison for Pb-Pb collisions, and also to investigate pp physics in its own right.

2.2 The NA57 Experiment

The NA57 experiment [21] was a fixed target experiment at the CERN SPS which studied the production of strange hadrons in heavy ion and more elementary collisions. It was the successor to the WA97 experiment, and was intended to extend the search for strangeness enhancement to less central Pb-Pb collisions and to lower beam energies. The layout of the NA57 experiment and the NA57 coordinate system are shown in figure 2.2. The beam travelled in the +x direction, and the tracks were bent in the x-y plane by the magnetic field, described below. Data from p-Be

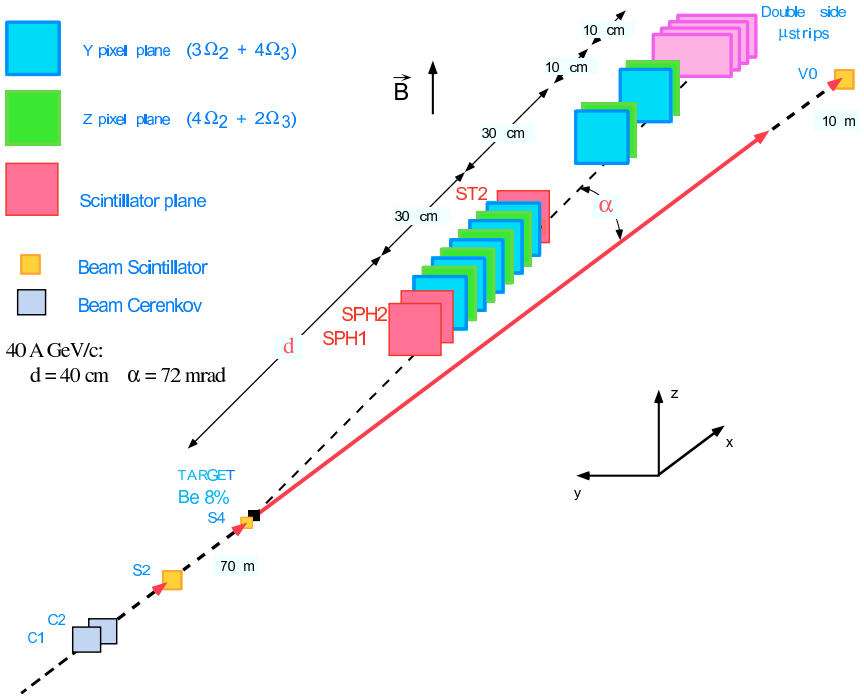

Figure 2.2: The NA57 apparatus as set up for p-Be collisions. The silicon telescope was 40 cm from the target at angle α to the beam.

and Pb-Pb collisions were taken between 1998 and 2001. These have been analysed separately.

The apparatus was placed in a 1.4 T magnetic field produced by the GOLIATH magnet, which allowed calculation of charged particle momentum by measurement of track curvature. Data were also taken with the field polarity reversed in order to reduce systematic errors. The experimental setup was slightly different for p-Be and Pb-Pb due to different triggering requirements and to ensure equivalent coverage in rapidity and transverse momentum.

2.2.1 Beam and Target

Different beams were used - protons at a beam momentum of 40 GeV/c and lead ions at 40 GeV/c per nucleon and 158 GeV/c per nucleon, as shown in table 2.2

Table 2.2: Summary of the collision systems studied at NA57 and WA97.

System	Beam momentum	Number of Events	Data set
p-Be	158 GeV/c	180 million	WA97
p-Pb	158 GeV/c	290 million	WA97
p-Be	40 GeV/c	60 million	NA57, 1999
p-Be	40 GeV/c	110 million	NA57, 2001
Pb-Pb	40A GeV/c	290 million	NA57, 1999
Pb-Pb	158A GeV/c	230 million	NA57, 1998
Pb-Pb	158A GeV/c	230 million	NA57, 1998

[21]. The NA57 data were complemented by data from 158 GeV/c p-Be and p-Pb collisions at WA97. The p-Be collision system provided a control experiment to be used for comparison with Pb-Pb. The Be target was 3 cm thick, which corresponds to an 8% probability of a proton interacting in it. The lead beam was used with a lead target to provide collisions suitable for QGP formation. The lead target was 0.4 mm thick which corresponds to 1% of an interaction length for a lead beam.

2.2.2 The Silicon Telescope

The NA57 detector was composed mainly of silicon pixel planes [63]. Silicon pixels allow the handling of the very high multiplicity in Pb-Pb collisions, provide high precision vertex finding and have a high rate capability which allows the collection of a large sample of events.

The main detector consisted of a "telescope" of thirteen silicon pixel planes, with eight planes in a compact part which was 30 cm long. Seven of these planes used pixels which were 75 $\mu m \times 500\ \mu m$ in size, with the other six using pixels with a size of 50 $\mu m \times 500\ \mu m$ [21]. Each plane was 5 cm $\times$ 5 cm and the telescope consisted of about 1.1×10^6 pixels in total. The telescope position was chosen in order to

accept particles produced within one unit of rapidity about central rapidity. As NA57 was a fixed target experiment, coverage of the central rapidity region required the telescope to be some distance from the target and at a shallow angle to the beam. For the 40 GeV/c runs, the telescope was placed 40 cm from the target and the lower edge made an angle of 40 mrad to the beam. For the 158 GeV/c runs, a separation of 60 cm was used and the angle was 72 mrad [21]. The minimum angles of 40 and 72 mrad resulted in an effective transverse momentum cut which was dependent on the mass of the particle producing the track. The minimum p_t for pions to be reconstructible with reasonable efficiency was about 180 MeV/c for Pb-Pb collisions [64].

2.2.3 The Trigger System

When an interesting collision occurred, the detectors were read out and the information was stored. In order to determine when such an event occurred, a trigger system was used. The NA57 trigger system was somewhat different for p-Be and Pb-Pb collisions, and both are described below.

The p-Be trigger system made use of two scintillators placed in front of the compact telescope, known as SPH1 and SPH2, and one behind the telescope, known as ST2. These are shown in figure 2.2. If at least two tracks passed simultaneously through the SPH1 and SPH2 scintillators together with a track through ST2, the trigger was activated. There were also detectors present in the beam before the target, known as S2 and S4, and additional detectors, C1 and C2, were placed in the beam and used to reject contamination from pions and kaons. These were designed so that the beam's protons travelled slower than light in the detector medium, but lighter particles with the same momentum travelled faster and so produced Cherenkov light. If this light was present, the trigger was rejected and the event was not recorded.

The scintillators in front of and behind the telescope were removed for Pb-Pb runs. Pb-Pb triggering used a petal detector, which consisted of 6 scintillators arranged around the beam axis. It was placed 10 cm downstream of the target. Each petal would provide a triggering signal if the number of tracks passing through it was greater than a defined threshold. If five out of six petals satisfied this condition, the trigger was activated. The Multiplicity Strip Detectors (MSD), were used to sample the charged particle multiplicity of Pb-Pb events which activated the petal trigger described above. The information from these MSD strips was used offline to calculate the collision centrality [65]. When using a Pb beam, the C1, C2, S2 and S4 detectors were replaced by a single detector, S2, which was used to detect when a lead ion was present in the beam. The number of photons produced in the S2 detector was much higher for lead ions than for any other possible particle in the beam, and so lead-lead events can easily be selected.

For p-Be collisions, an event was accepted if the following condition was met:

$$\overline{\mathrm{C1}}.\overline{\mathrm{C2}}.\mathrm{S2}.\mathrm{S4}.\mathrm{SPH}.\mathrm{SPH2}.\mathrm{ST2}.\overline{\mathrm{BUSY}} \tag{2.1}$$

i.e. if the beam contained protons ($\overline{\mathrm{C1}}.\overline{\mathrm{C2}}$), the beam was on target (S2.S4), there were at least 2 tracks in the detector (SPH1.SPH2.ST2) and the data acquisition system was ready to receive an event ($\overline{\mathrm{BUSY}}$).

For Pb-Pb collisions, an event was accepted if the following condition was met:

$$\mathrm{S2}.\mathrm{PETALS}.\overline{\mathrm{BUSY}} \tag{2.2}$$

i.e. if the beam was on target and contained a Pb ion (S2), a large number of charged tracks was produced (PETALS) and the DAQ was ready to receive an event ($\overline{\mathrm{BUSY}}$).

2.3 The ALICE Experiment at the LHC

2.3.1 Introduction

The ALICE experiment is one of four large experiments at the LHC, and is the only detector at the LHC which is designed primarily for the study of heavy ion collisions. As a result, it must be a general purpose detector which can measure a wide range of of QGP signatures. This chapter will describe the sub-detectors and general features of ALICE, with emphasis on the areas most relevant to the analysis in this thesis.

2.4 The ALICE experiment overview

The ALICE detector differs from most previous heavy ion experiments in that it is designed to be as general purpose as possible, rather than focussing on specific signatures. To achieve this, it uses a large number of sub-detectors, allowing for the detection, tracking and identification of hadrons and leptons over a large range of p_t, as well as precise vertex finding and identification of secondary tracks for measurement of strangeness, charm and beauty signals.

2.4.1 The ALICE main sub-detectors

The ALICE detector, shown in figure 2.3, is composed of a central tracking barrel and a number of additional detectors. The central tracking uses four detectors - the inner tracker (ITS), a time projection chamber (TPC), a transition radiation detector (TRD) and a time of flight detector (TOF).

The ITS, TPC and TOF detectors are primarily intended to study hadronic signals, and cover the pseudorapidity range $-0.9 < \eta < 0.9$ and the full 2π azimuth.

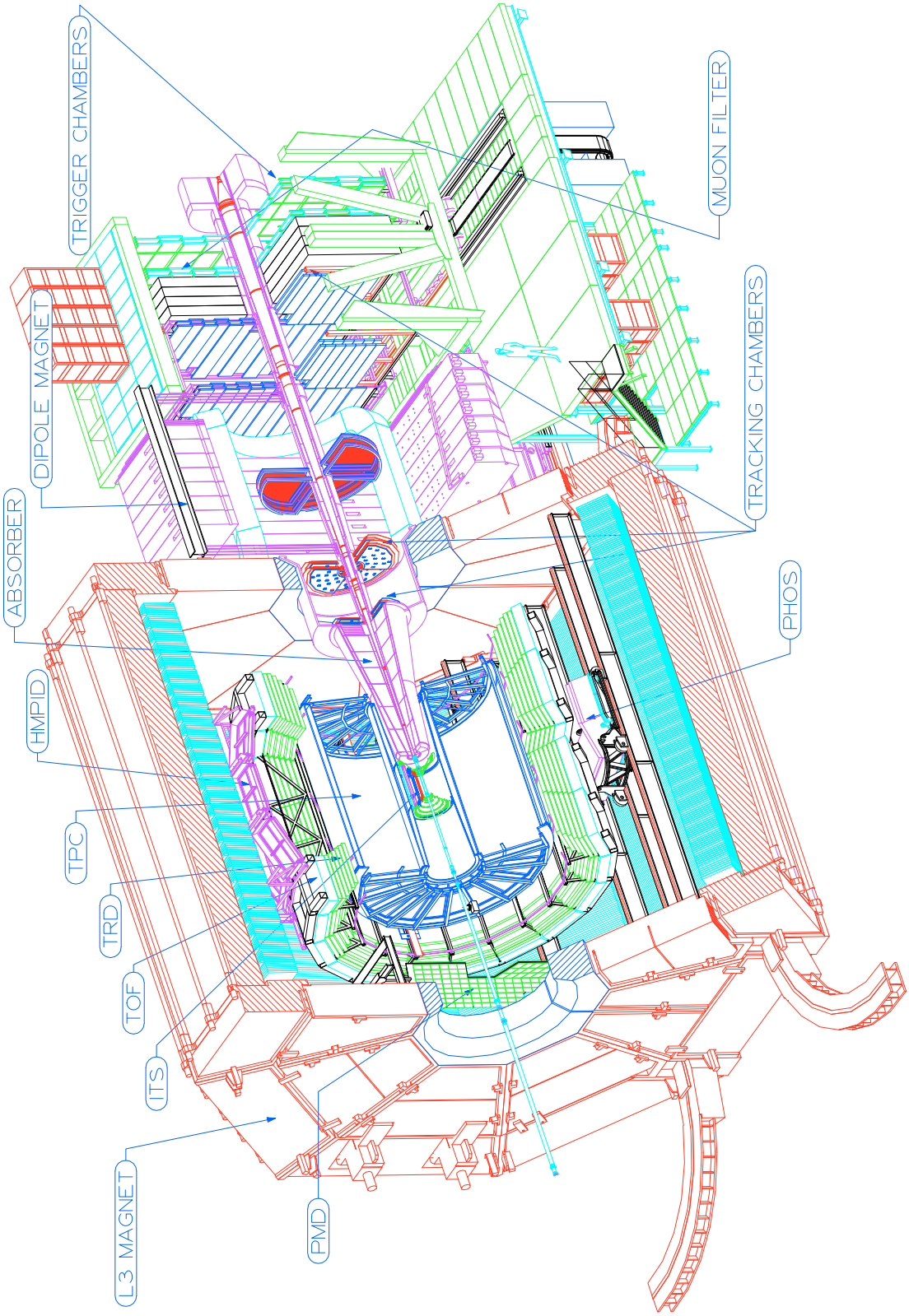

Figure 2.3: The ALICE detector.

These detectors and their roles are described individually in the sections below. The other detectors include:

- The transition radiation detector (TRD), used for identification of electrons in the central rapidity region. It is described further in section 2.4.4.
- The High Momentum Particle Identification Detector (HMPID) [66], which uses a Ring Imaging Cherenkov (RICH) detector to provide effective particle identification (PID) at higher transverse momentum than the other detectors.
- The Photon Spectrometer (PHOS) is an electromagnetic calorimeter designed for the measurement of photons. It consists of 17,920 separate elements, which are made of lead-tungstate crystals. It covers a small pseudo-rapidity range of $-0.12 < \eta < +0.12$ and has an azimuthal acceptance of 100 degrees [67]. It will be used for the investigation of direct photons from the early stages of the collision, π^0 reconstruction and other physics topics [67].
- The Forward Muon Spectrometer [68] is dedicated to the study of muon pairs in the forward rapidity region, such as those from the decay of heavy quarkonia. It covers the pseudorapidity range $2.5 < \eta < 4.0$ and consists of a set of absorbers to remove hadrons and other background, a 0.7 T dipole magnet to allow momentum measurement and triggering and tracking systems.
- Smaller detectors, such as the Zero Degree Calorimeter and the triggering detectors, V0 and T0, which are described later.
- A large acceptance electromagnetic calorimeter (EMCAL), which will provide triggering on high energy jets and improve jet energy resolution [69].

The ITS, TPC, TRD, TOF, PHOS and HMPID detectors are placed in a 0.5 T magnetic field produced by a warm solenoid magnet [28]. The muon tracker is placed in a 0.7 T field produced by a warm dipole magnet [68].

2.4.2 Inner Tracking System

The ITS [70] is composed of six cylindrical layers of silicon detectors. The inner two layers are silicon pixel detectors, similar to those used by NA57. They are placed at radii of 4 cm and 7 cm, close to the interaction point which is at r = 0. The layers consist mostly of pixels of size 50 μm × 300 μm and cover the full 2π azimuth and the region -16.5 cm < z < +16.5 cm [70]. These can cope with a very high density of particles, have a high rate capability and allow precise impact parameter measurement [28], but do not provide particle identification information. The middle two layers, at 15 cm and 24 cm, are silicon drift detectors and the outer two layers, at 39 cm and 44 cm, are double-sided microstrip detectors. The drift and microstrip detectors have analogue readout and so can provide a measurement of dE/dx, which can be used for particle identification at low p_t. The ITS covers the pseudorapidity range $-0.9 < \eta < 0.9$, with the first pixel layer having a larger coverage of $-1.98 < \eta < 1.98$.

A key feature of the ITS is high precision position measurements. To achieve this, there are approximately ten million cells in the pixel detectors [28], which provide good track separation, even in the high multiplicity environment of a central Pb-Pb collision. Precision in position measurement is 100 μm in the beam direction and 12 μm in the $r\phi$ direction. The silicon drift detectors improve the precision of z measurement, having a precision of 28 μm.

The contributions of the ITS to the physics analysis include:

- High precision measurement of the primary vertex. The precision depends on the charged track multiplicity, and so is different for pp and Pb-Pb collisions. It is of the order of 100 μm for pp collisions and 10 μm for central Pb-Pb collisions [70].
- Reconstruction of secondary vertices from weak decays.

- Tracking and identification of particles with momentum below 100 MeV/c.
- Improvement of angle and momentum resolution for particles reconstructed in the TPC.
- Precise measurement of track impact parameters.

For the analysis discussed later in this thesis, the ITS contributes to the rejection of secondary tracks by measuring track impact parameters and improves momentum measurement and particle identification.

2.4.3 Time Projection Chamber

The Time Projection Chamber (TPC) [71] is a large, gas-filled chamber which is the main tracking detector of ALICE. It must be able to cope with a large number of tracks per event and provide excellent position and momentum measurement for each of these tracks. A gas-based detector is well-suited to these conditions, as the low material density reduces production of secondary tracks from interactions in the material, while its large volume allows for good measurements of particle paths and correct tracking of separate particles despite the high track density.

The TPC is a cylinder with an inner radius of about 85 cm, an outer radius of about 250 cm and a length of 500 cm along the beam direction. It is filled with a mixture of neon ($\sim 85\%$), carbon dioxide ($\sim 10\%$) and nitrogen ($\sim 5\%$) [72].

As charged particles travel through the gas, they cause ionization. An electric field is applied in the longitudinal direction, so electrons produced by this ionization drift to the readout chambers. The readout chambers are multiwire proportional chambers with cathode pad readout. They make use of three grids - a gating grid, a cathode wire grid and an anode wire grid [71]. As the electrons produced from ionization drift into the chamber, the acceleration between cathode and anode grids

produces an avalanche of electrons, amplifying the signal. The gating grid can be used to prevent electrons from the drift volume from entering the amplification region if a valid trigger is not present.

The drift field strength is about 400 V/cm, giving a maximum drift time of about 88 μs. This time places a limit on the acceptable event rate, as too high a rate will cause overlapping events, known as pile-up. Pile-up is considered unacceptable for central Pb-Pb events, as the multiplicity for a single event is very high, but it is allowed for pp in order to obtain a larger event sample. An average of about 40 pp interactions occur within the TPC drift time [62], but the low multiplicity means that these events can be distinguished.

The TPC can track particles in the pseudorapidity range $-0.9 < \eta < 0.9$ and with transverse momentum up to 100 GeV/c with good momentum resolution. The typical momentum resolution for tracks with momenta between 100 MeV/c and 1 GeV/c is 1 to 2 percent [28]. In addition to tracking, the TPC provides particle identification by measurement of dE/dx, as particles of different mass will produce different levels of ionization.

2.4.4 Transition Radiation Detector

The TRD [73] is designed to identify electrons at p_t greater than 1 GeV/c in the pseudorapidity range $-0.9 < \eta < 0.9$, in order to allow measurements of the di-electron continuum and of both light and heavy resonances in the electronic decay channels. For example, to measure decays of J/Ψ, ρ or ϕ in the dielectron channel, it is essential to be able to distinguish pions and electrons accurately in order to reject contamination by the much more abundant pions.

The TRD exploits the fact that a relativistic charged particle will radiate when passing between two media of different dielectric constants. The intensity of the radiation is strongly dependent on the relativistic γ factor, and is approximately

proportional to it if γ is large. As the next lightest particle is more than 200 times heavier than the electron, the γ for equivalent momenta is a similar factor smaller. Therefore, the amount of transition radiation produced for electrons is much larger than for any other charged particle, and this allows the electrons to be easily identified.

The TRD occupies the region with radial position between 2.9 and 3.7 metres, and is divided into 18 azimuthal segments, 6 radial layers and 5 longitudinal segments, giving a total of 540 modules. Each TRD module consists of a 4.8 cm thick radiator, composed of a fibre/foam sandwich, and a multiwire proportional chamber (MWPC) [73]. Each chamber has 144 pads in the $r\phi$ direction and between 12 and 16 pad rows in the z direction. A particle passing through the radiator will produce transition radiation, which causes ionization of the gas in the the MWPC. The gas used is 85% xenon and 15% carbon dioxide to allow optimal absorption of the radiation [73]. Amplification occurs due to multiplication in the gas, and the signal produced can then be measured.

The TRD also helps with the tracking, and improves the measured momentum resolution when combined with the ITS and TPC.

2.4.5 Time of Flight Detector

The TOF subdetector [74] is used for particle identification at larger p_t than is provided by the ITS and TPC. It provides identification of hadrons in the momentum range of 0.5 GeV/c to 2.5 GeV/c, and identifies particles by measuring their velocity. Since momentum is known from the tracking detectors, this allows the mass to be determined. The ability of the TOF to distinguish pions and kaons in this range means that the TOF can make a useful contribution to the ρ^0 analysis described later in this thesis. Due to particles of this momentum being relativistic and, therefore, travelling at similar velocities, excellent time resolution is essential. An overall

resolution of 150 ps is needed to achieve the level of identification required, and the ALICE TOF is expected to have an intrinsic resolution of ~ 90 ps and to satisfy the 150 ps requirement when other sources of error are taken into account [74].

The TOF is placed inside the ALICE solenoid magnet and covers the full 2π azimuth and the pseudorapidity range $-0.9 < \eta < +0.9$ [75]. It has an inner radius of 3.70 metres and is made of 1,638 modules. Each module consists of multigap resistive plate chambers (MRPCs) and the front end analogue cards [75]. The resistive plate chambers are gas-filled chambers containing stacks of equally spaced resistive plates. An electric field is applied between the plates, which creates an avalanche effect when a particle traversing the gaps causes ionization. The signal produced can then be sampled and read out.

2.4.6 The Trigger

The trigger system is an essential component of the ALICE detector, and performs several roles. Its principal role is to identify when interesting events occur, and to trigger the read-out of the sub-detectors for these cases. It must protect against pile-up and handle both common and rare triggers to ensure that appropriate rates of data are taken [62].

The trigger reacts to signals from special triggering detectors, as well as signals from some of the main sub-detectors. The ALICE trigger system has a diverse set of requirements. It must be able to correctly trigger on heavy ion events of various multiplicities, and must also handle rare, specialised triggers such as high p_t $\mu^+\mu^-$ events in pp collisions.

The Central Trigger Processor

The CTP [76] receives triggering inputs from the triggering detectors and status information from all detectors. Using the information from the trigger detectors, it supplies triggering signals to the sub-detectors to ensure that they are read out at the appropriate time. The CTP also handles calibration requests from the sub-detectors and provides monitoring information to the Data Acquisition system (DAQ).

The ALICE trigger system has three levels. Level 0 has 24 inputs and is very fast - the time between a collision and the detector receiving a readout command from the trigger is 1.2 μs, which is mostly due to the transit time in the cables. The actual processing time of the CTP for level 0 triggers is about 100 ns. Level 1 has up to 24 inputs and delivers a trigger signal to the detectors 6.5 μs after the collision. Level 2 has 12 inputs and waits until the end of all detector sensitive periods, and so does not provide its signal until at least 88 μs [76]. The detectors which contribute to the trigger system are the cosmic ray detector and trigger (ACORDE), EMCAL, the silicon pixel detectors of the ITS, the muon arm, PHOS, TOF, TRD, V0, T0 and the ZDC. Minimum bias and centrality based triggers, which are of interest to my analysis, make use of triggers from T0, V0, the TRD and the ZDC. Other, rarer triggers, intended to study specific physics processes, make use of the other detectors.

Due to the long readout time of the TPC, it is possible for a second event to overlap the first, which is known as pile-up. This must be avoided for central Pb-Pb events due to the very high multiplicity, and information from faster detectors is used to reject overlapping events. This is handled by the level 2 trigger, which waits until the end of the past-future protection interval of 88 μs to make sure there are no overlapping events.

V0 and T0

The V0 detector [77] consists of two arrays, V0A and V0C, which are located at either side of the interaction point. Each array is made of 72 counters, which contain scintillator material connected to photomultipliers by optical fibres. Its roles include supplying a minimum bias trigger for the central barrel detectors, providing centrality triggers for Pb-Pb collisions and rejecting background from, for example, beam-gas interactions [28].

The T0 detector [77] provides more precise timing information than the V0 detector. It is used to provide the earliest triggers, to reject beam-gas interactions by measuring the vertex position and to provide signals for the TOF and TRD detectors. It also measures the particle multiplicity and provides one of three trigger signals: minimum-bias, semi-central or central. The detector consists of Cherenkov counters in two arrays, with twelve counters per array. $T0_R$ is placed 70 cm from the nominal vertex and $T0_L$ is about 350 cm from the nominal vertex on the opposite side.

Both V0 arrays are placed close to the beam pipe, with an inner radius of about 4 cm. V0A is located 340 cm from the interaction point and V0C is placed 90 cm from the interaction point on the opposite side. Particle detection is possible down to an angle of 0.7 degrees for V0A and 2.6 degrees for V0C [77].

ZDC

The Zero Degree Calorimeter (ZDC) [78] is used to measure the energy of the non-interacting nucleons in a Pb-Pb collisions. This energy decreases with increasing centrality, and so this measurement allows the collision centrality to be determined.

The ZDC is placed 116m from the interaction point. It consists of two hadronic calorimeters - a neutron ZDC and a proton ZDC. An electromagnetic calorimeter is

also included. This measures the energy of particles at forward rapidity, which are mostly photons from π^0 decays.

2.4.7 Data Acquisition (DAQ) system

The DAQ [79] system is responsible for coordinating the detector read-out and data storage. The trigger and DAQ systems must be able to handle both frequent and rare triggers, and must make sure both are recorded efficiently.

The DAQ system is designed to be able to store data at a rate of up to 1.25 GB/s for Pb-Pb running [62]. Data storage capability is a limiting factor for common triggers - the typical interaction rate for central Pb-Pb events is 10^3 Hz and for minimum bias Pb-Pb events is 10^4 Hz, which is far more than the DAQ is capable of storing. Certain physics studies, such as dimuons, require a much larger sample of events than this, so the trigger and DAQ systems must give special consideration to these events and trigger on them at a proportionally higher rate to minimum-bias events. For my analysis, described later in this thesis, the central and minimum bias events are desired.

Data volumes for pp collisions are much smaller, and events can be stored at a larger rate. The DAQ is capable of recording data for pp collisions at the maximum possible rate for the ALICE detectors, 1 kHz, and is expected to store pp events at 100 Hz on average [62].

When a valid level 2 trigger is received, the data is read out from all the sub-detectors in parallel and transferred to the DAQ system. The DAQ then constructs the event from this information, and performs triggering according to the high level trigger (HLT). The final event construction is performed as required and sent to mass storage.

Chapter 3

Reconstruction and selection of strange particles at NA57

3.1 Introduction

The aim of the NA57 experiment was to measure strange particle yields. To achieve this, it was necessary to reconstruct the strange particles and to obtain a clean sample, free from background. In order to remove the background, a set of selection criteria was imposed, known as "cuts", which are described and justified below. A sample of Ξ^- particles was obtained, which was used in the later analysis to calculate the total yield of this strange particle species.

3.2 Track reconstruction

A charged particle passing through the silicon pixel planes leaves a trail of signals in the pixels, known as hits. The NA57 track reconstruction program, ORHION, was used to fit helical tracks to these hits. The momenta of the particles were calculated

from the track curvature using the well-known relationship between curvature and momentum in a magnetic field:

$$p = 0.3Br \tag{3.1}$$

where p is momentum in GeV/c, B is magnetic field strength in Tesla and r is the radius of curvature in metres.

The high precision position measurement provided by the pixels allowed vertices, or the positions of intersections of tracks, to be determined to good precision, which was essential for the rejection of background.

3.3 Data sets

Two separate data sets were analysed, each containing a sample of p-Be collisions at a beam momentum of 40 GeV/c. One of the data sets was recorded in 1999 and contained 60 million events, and the other was recorded in 2001 and contained 110 million events. Some changes were made to the experimental setup between the 1999 and 2001 runs. For example, the arrangement of planes in the telescope was changed, and the microstrips shown in figure 2.2 were not used for the 1999 run. Additionally, the pixel efficiencies themselves may have changed due to radiation damage.

When analysing this data, it was observed that the quantity and distribution of background was sometimes not the same for the two data sets. Consequently, different cuts were sometimes used.

3.4 V^0 and cascade decays

The NA57 experiment measured yields of strange particles in order to investigate strangeness enhancement in heavy ion collisions. The particles investigated were the Λ(uds), Ξ(dss) and Ω(sss) baryons and the K^0 meson. They were found by reconstructing the weak decays

$$K^0 \rightarrow \pi^+\pi^- \tag{3.2}$$

$$\Lambda \rightarrow p\pi^- \tag{3.3}$$

$$\Xi^- \rightarrow \Lambda\pi^- \rightarrow p\pi^-\pi^- \tag{3.4}$$

$$\Omega^- \rightarrow \Lambda K^- \rightarrow p\pi^- K^- \tag{3.5}$$

and the corresponding antiparticle decays. The K^0 and Λ are neutral particles which decay into two oppositely charged particles, and these decays are known as V^0 decays. The Ξ and Ω particles decayed into a Λ and a charged track. The Λ then decayed as above, and so these are known as cascade decays. The charged particles in all of these cases were detected by the silicon telescope. V^0s were identified by looking for two oppositely charged tracks which intersect. Cascades were identified by first finding V^0s, then looking for intersections of the calculated V^0 line of flight and a charged track. This procedure was performed by the NA57 CASCADE program.

3.4.1 Cowboys and sailors

V^0 decays can have two topologies, known as cowboys and sailors. In a cowboy decay, the decay tracks initially travel in the opposite direction to their acceleration due to the magnetic field. The tracks from sailor decay initially travel in the same direction as their acceleration. The tracks from a cowboy decay bend back and do

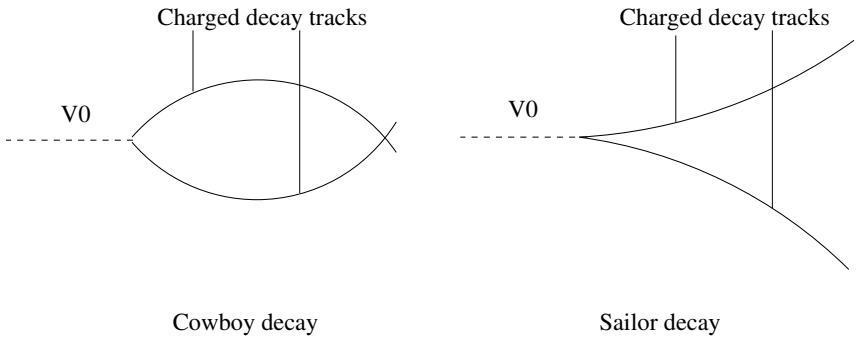

Figure 3.1: A cowboy (left) and sailor (right) V^0 decay. The cowboy topology is preferred as the tracks are closer together when they reach the silicon telescope, and so are more likely to both be reconstructed.

not spread out as much as for a sailor decay, as shown in figure 3.1. As a result of this, the cowboy decays had a much higher acceptance in the NA57 detector than the sailor decays.

3.5 Selection Cuts

This analysis was concerned with cascade decays. In the p-Be collisions at 40 GeV/c, the number of Ωs produced was low, and so the Ξ^- and $\overline{\Xi}^+$ were the focus of this analysis.

The reconstruction process combined tracks with appropriate sign to form V^0s and cascades. The mass of the original particle was determined by considering energy and momentum conservation, assuming that the particles forming the decay had certain masses. For example, when reconstructing Λs, it was assumed that the positive decay track was a proton and the negative track was a pion. This assumption was not always correct, as the background will include non-pion tracks, and some V^0s which decayed into other particles. As a result, a large background was superimposed onto the signal and this background must be reduced as much as possible. This was achieved by applying various selection procedures, known as

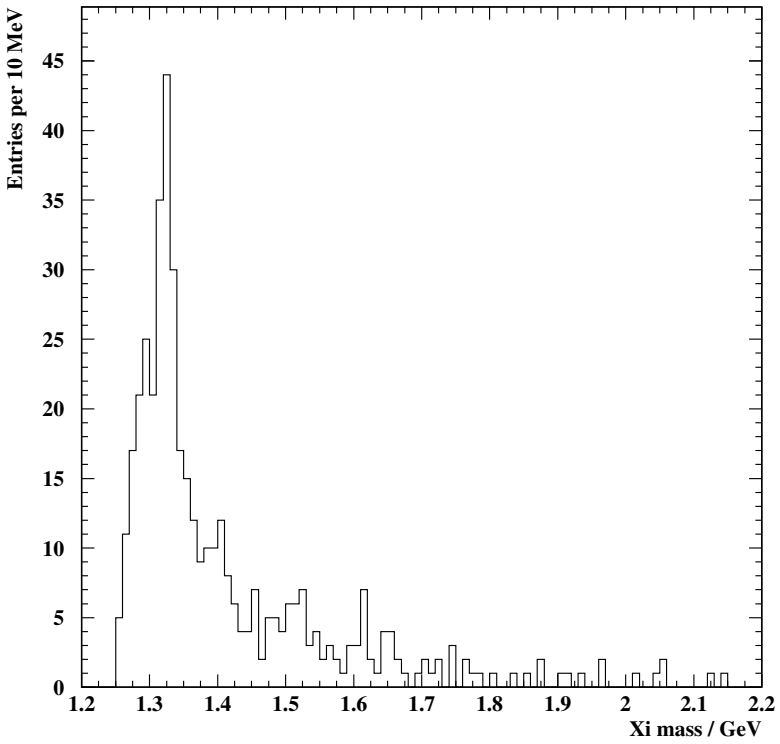

Figure 3.2: Reconstructed Ξ mass distribution for the 2001 sample after preliminary cuts.

cuts.

Some preliminary cuts were applied by the reconstruction software. However, these were very loose and were not sufficient to produce a clean sample of Ξ^- particles. A plot of the reconstructed Ξ mass with only these cuts is shown in figure 3.2. The focus of the analysis described in this chapter was to improve this result by applying further selection cuts.

3.5.1 Decay Vertex Position

For V^0s which decayed close to the target, there was a lot of background from tracks produced in the collision, which were mostly pions. Combinations of these tracks

may result in false V^0 reconstructions. The position of the detector was chosen to minimise this problem, but further background reduction was required. The decay tracks were traced back to the point of intersection, i.e. the decay vertex, and so V^0 and cascade decay vertex positions were found for each Ξ.

In order for the trigger to be activated, two charged tracks must pass through the scintillators in front of the telescope. Therefore, particles which decayed beyond the scintillators will not have been recorded unless other tracks activated the trigger. Very little signal was seen beyond this point, but a large amount of noise was present from interactions in the scintillator and telescope, in particular from gamma conversions, and so a cut was used to remove the noise. The cut required the position of the V^0 decay vertex, xvc, to be less than -27 cm, as x = -27 cm corresponded to the start of the scintillator. This cut is illustrated in figure 3.3. As described in chapter 2.2, the beam travelled in the +x direction, so this cut selected only Ξ candidates whose corresponding V^0s decayed before the triggering scintillator. The region of low signal-to-background ratio was rejected by this cut.

Additionally, in a small number of cases, one track was reconstructed as two tracks with nearly identical positions and momenta. These extra tracks were known as ghost tracks, and resulted in a false cascade decays being reconstructed from a V^0 decay. Although these were rare, the desired signal was also rare and so these ghost tracks caused significant contamination. These false cascades had their V^0 and cascade decay vertices very close to each other, and so could be filtered out on this basis. The cuts used to do this were:

- For the 2001 data sample, the V^0 and cascade decay vertices must be separated by at least 2 cm in x.
- For the 1999 data sample, the V^0 and cascade decay vertices must be separated by at least 4 cm in x.

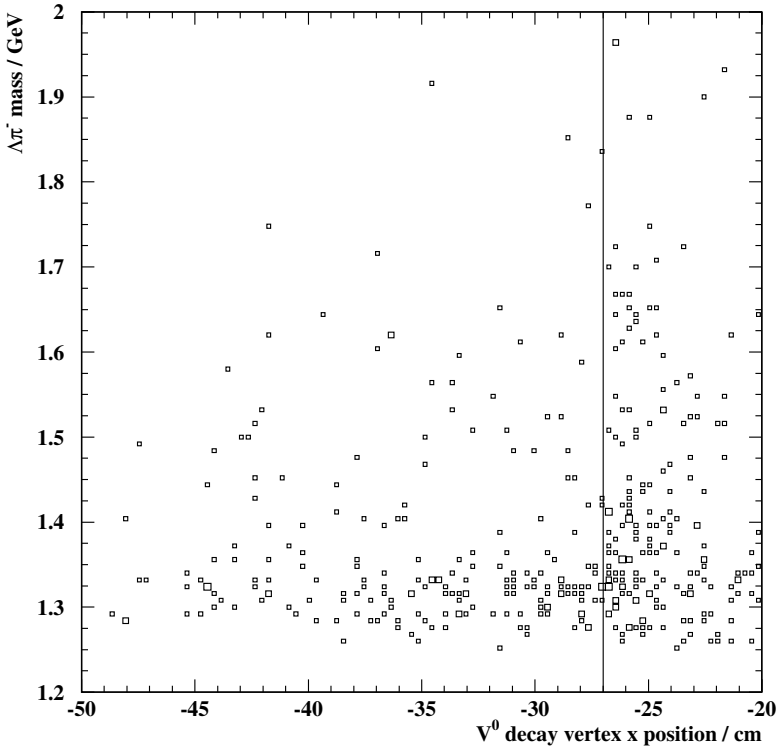

Figure 3.3: Ξ mass against V^0 decay vertex position. Background from interactions in the triggering scintillator is observable at $-27 < x < -25$ cm. Only Ξ candidates whose V^0 vertices were before the scintillator, i.e. to the left of the vertical line, were accepted.

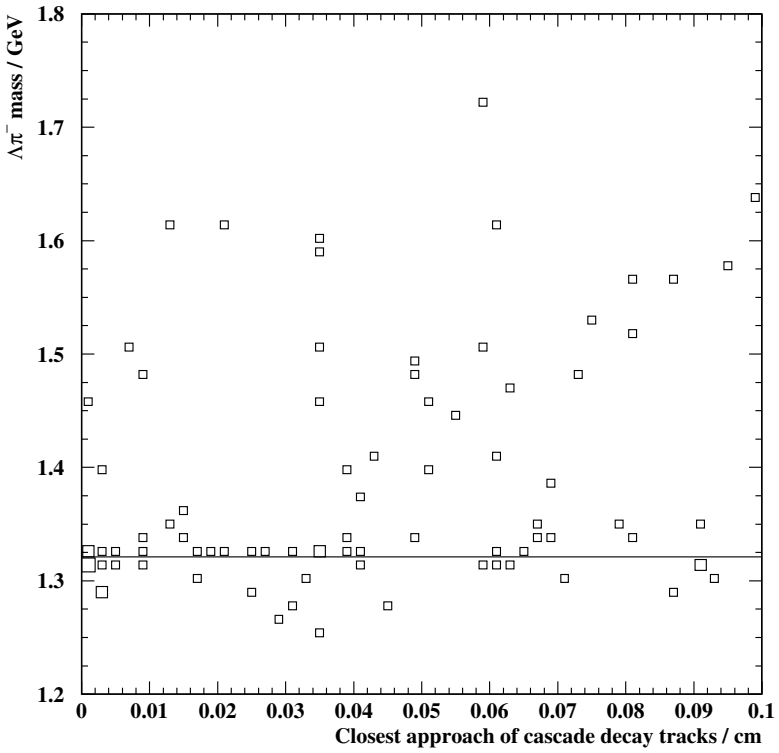

Figure 3.4: Ξ mass against closest approach of cascade decay tracks.

3.5.2 Closest approach of decay tracks

As the decay tracks from a V^0 originate at the same point, the reconstructed tracks should intersect when traced back from the telescope. However, due to errors in position and momentum measurement, they will realistically have some finite minimum separation. The decay vertex is at the point where the tracks are closest, and the separation at this point is known as the distance of closest approach. For a genuine decay, this distance should be small, with a reasonable maximum determined by the experimental resolution. As this gets larger, the probability of the decay being genuine decreases, as it becomes more likely that the tracks are unrelated.

The increase in background at large values of closest approach can be seen in figure 3.4. A cut was therefore made on the closest approach for the V^0 and cascade

decays:

- The closest approach of decay tracks for V^0 and cascade decays must be less than 0.066 cm.

3.5.3 Internal decay angle

Further background reduction was achieved by considering the internal decay angle. For this, a new coordinate system was defined, x', y', z'. x' is the direction of travel of the V^0, y' is perpendicular to x' and is in the bending (x-y) plane. z' is perpendicular to x' and y'. In the $z' - y'$ plane, the decay particles appear back-to-back in order to conserve momentum. A projection of a decay track's vector onto this plane can be made, and the internal decay angle, known as ϕ, is the angle between this projection and the y' axis. An example of a V^0 and its ϕ angle is shown in figure 3.5.

The tracks from a genuine V^0 decay are produced with a uniform distribution in ϕ, as the initial y' and z' momentum components of the V^0 are zero and no decay angle is preferred. However, false V^0s from combinatorial background were not produced uniformly in ϕ, and in fact there was a large excess of background at low ϕ, as can be seen in figure 3.6. This was due to the fact that a pair of unrelated tracks is much more likely to appear to have a valid V^0 vertex if the ϕ angle is small. The following cuts were used to remove this background:

- For the 2001 data, the magnitude of ϕ must be greater than 0.2 radians.
- For the 1999 data, the magnitude of ϕ must be greater than 0.4 radians.

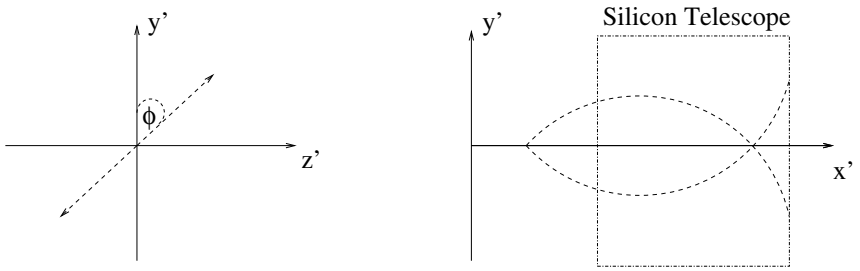

Figure 3.5: The internal decay angle of a V^0 decay. The left diagram shows the decay particles emitted back-to-back in the y'-z' plane. The right diagram shows the bending of tracks in the magnetic field and the tracing back from the detector to a vertex.

3.5.4 Armenteros-Podolanski cuts

A variable α is defined in equation 3.6 [80].

$$\alpha = \frac{q_l^+ - q_l^-}{q_l^+ + q_l^-} \tag{3.6}$$

where q_l^+ and q_l^- are the components of momentum of the positive and negative decay tracks respectively with respect to the V^0's direction. In the V^0 rest frame, the momentum distributions of the decay tracks must be the same due to conservation laws. When the Lorentz boost is applied to this to obtain the momentum in the laboratory frame, this symmetry is broken and the heavier particle will have more momentum. If the positive decay particle is more massive, the distribution of α will be centred around a positive α. This can be used to distinguish particle decays from antiparticle decays, and both from background. For cascades, this equation is modified slightly, with the q_l of one of the charged tracks being replaced with that of the V^0 from the decay.

The Armenteros plot uses α for the x-axis and q_t, which is the magnitude of the component of momentum of one of the decay tracks perpendicular to the direction of the V^0, for the y-axis. Conservation of momentum requires that q_t is the same for both tracks. Figure 3.7 shows an example Armenteros plot for the V^0s. Each particle species forms a separate ellipse, and the separate species are easily distinguishable.

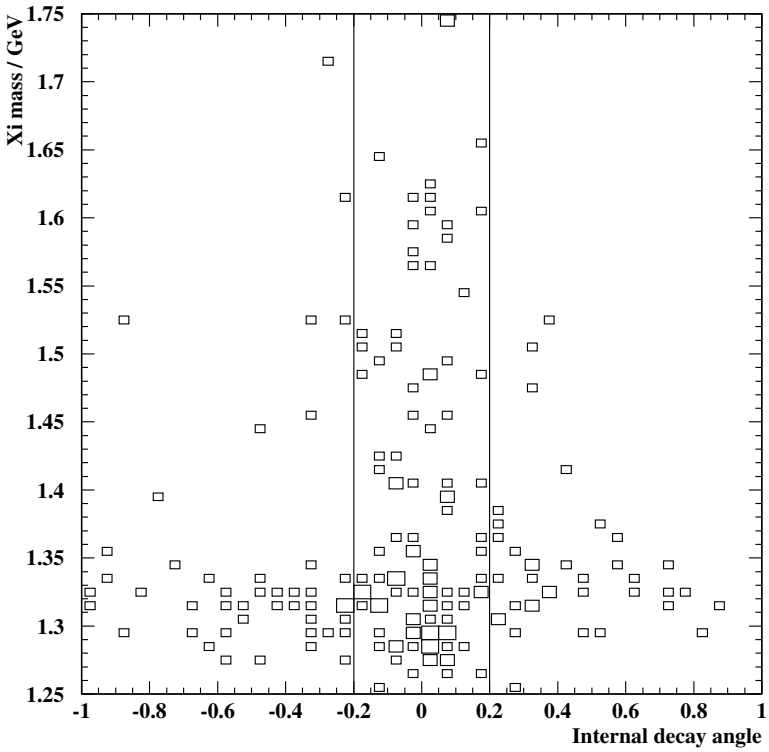

Figure 3.6: Ξ mass against the internal decay angle ϕ for the 2001 data sample. The cut on ϕ is shown by the vertical lines.

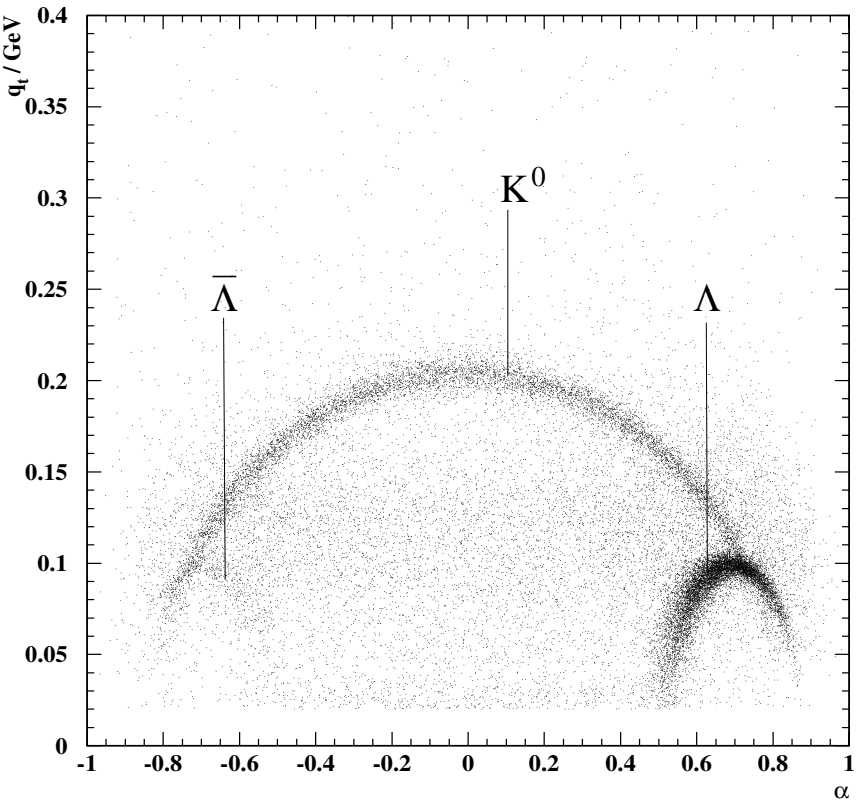

Figure 3.7: Armenteros-Podolanski plot for V^0s from NA57 data.

A cut on the Armenteros-Podolanski variable was not necessary for the 2001 data, but the following cuts were used for the 1999 data to select Ξ^-:

- α for the cascade decay must be greater than zero.
- α for the V^0 decay must be greater than zero.

To select the $\overline{\Xi}^+$, these cuts were reversed so that the αs must be less than zero.

3.5.5 Primary vertex position

The Be target was 3 cm thick and was centred at x = -60.00 cm during the 1999 run and at x = -60.75 cm during the 2001 run. The S4 scintillator was upstream of the target, and the beam interacting in this scintillator produced particles which entered the detector and caused background. Some of these can be seen in figure 3.8. To filter these out, the point of creation, known as the primary vertex, was calculated for each Ξ, and this was required to be within a reasonable distance of the target. The primary vertex was calculated by tracing back the cascade from its decay vertex to the point at which its z-coordinate intersects that of the beam, using equation 3.7. The x position of the primary vertex was required to be within 6 cm of the target's central position.

$$x_{primary} = x_{cascade} - (z_{cascade} - z_{beam})\frac{p_x}{p_z} \tag{3.7}$$

3.5.6 Summary of Cuts

The cuts used for the 2001 data set are summarised below:

1. The V^0 and cascade decay vertices must be separated by at least 2 cm in the x direction.

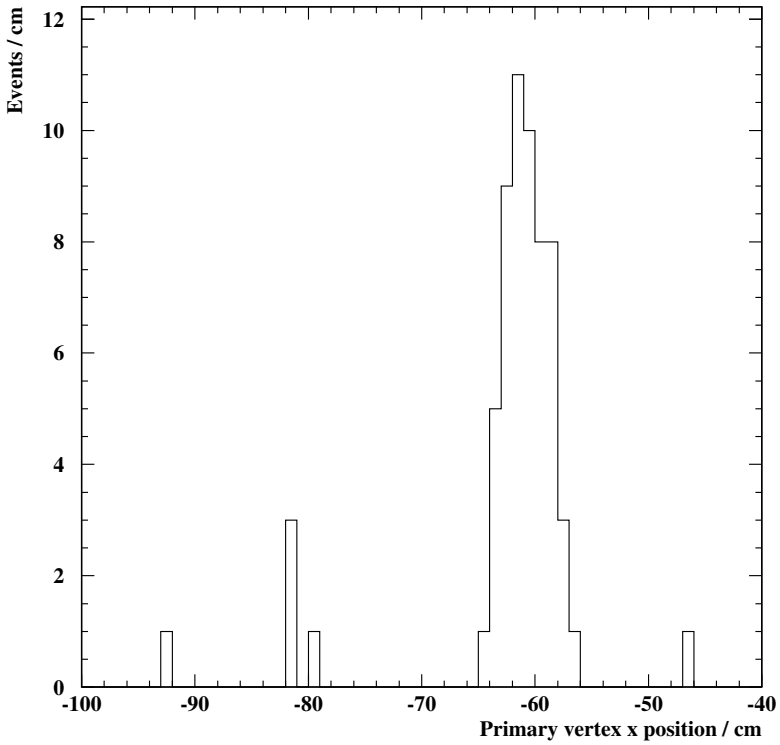

Figure 3.8: Distribution of primary vertex positions of cascades after other cuts have been applied.

2. The closest approach of the V^0 and cascade decay vertices must be less than 0.066 cm.

3. The ϕ angle for the cascade decay must be greater than 0.2 radians.

4. The V^0 decay vertex, and hence the cascade decay vertex, must have an x position less than -27 cm, i.e. must be before the telescope.

5. The primary vertex must have an x position within 6 cm of the central value of the target.

6. The reconstructed Ξ mass must be within 15 MeV/c^2 of the PDG value.

7. The reconstructed Λ mass must be within 15 MeV/c^2 of the PDG value.

Similarly, the cuts used for 1999 were:

1. V^0 and cascade decay vertices must be separated by at least 4 cm in the x direction.

2. The closest approach of the cascade decay vertex must be less than 0.066 cm.

3. The ϕ angle for the cascade decay must be greater than 0.4 radians.

4. The V^0 decay vertex must have an x position less than -27 cm, i.e. must be before the telescope.

5. The primary vertex must have an x position within 6 cm of the central value of the target.

6. The Armenteros α for cascade and V^0 decays must be greater than zero to select Ξ^- and less than zero to select $\overline{\Xi}^+$.

7. The reconstructed Ξ mass must be within 15 MeV/c^2 of the PDG value [19].

8. The reconstructed Λ mass must be within 15 MeV/c^2 of the PDG value [19].

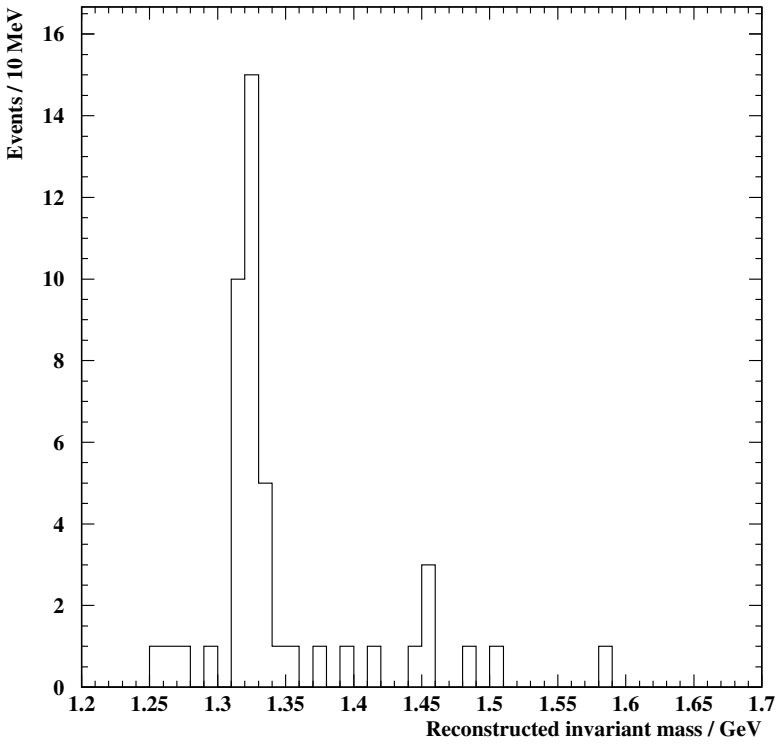

Figure 3.9: Plot of reconstructed Ξ mass for 2001 Ξ candidates after all cuts apart from the Ξ mass cut.

3.6 Ξ signal

Figures 3.9 and 3.10 show histograms of reconstructed Ξ mass before the final mass cuts were made, including both Ξ^- and $\overline{\Xi}^+$candidates. There is a clear signal with minimal background for 2001, but the statistics are low. As a result, there will be a large statistical error on the final yield. The 1999 data has even lower statistics and there is some evidence of remaining background.

The final, clean event samples obtained were used in the weighting procedure described in the next chapter. 29 Ξ^-s and 1 $\overline{\Xi}^+$were present in the 2001 sample after cuts and 10 Ξ^-s and 1 $\overline{\Xi}^+$were present in the 1999 sample after cuts. The number of $\overline{\Xi}^+$candidates is not high enough to calculate a yield, but a yield should

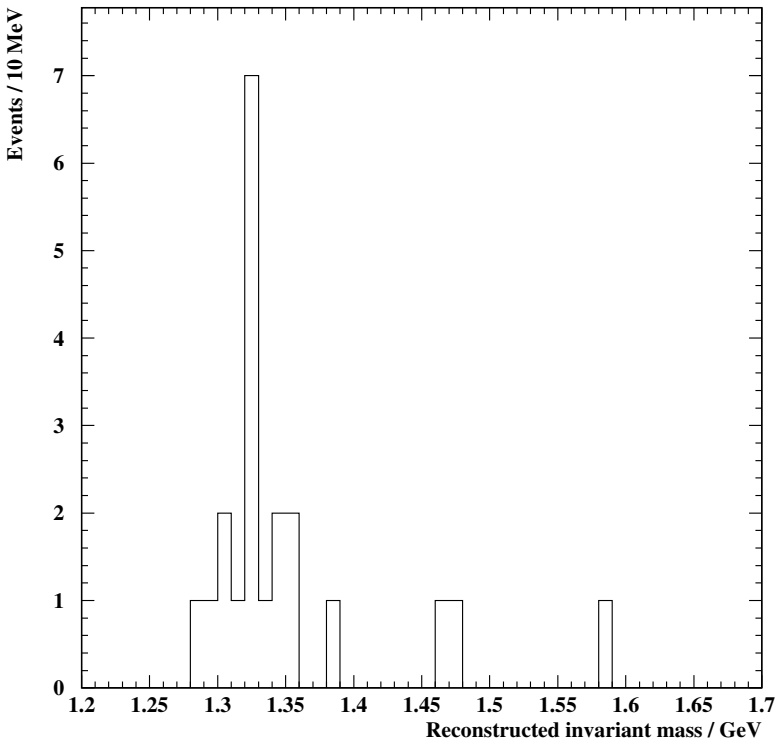

Figure 3.10: Plot of reconstructed Ξ mass for 1999 Ξ candidates after all cuts apart from the Ξ mass cut.

be obtainable for Ξ^-.

Chapter 4

Yield Calculation

4.1 The Weighting Chain

The sample of Ξ^- particles obtained in the previous chapter represents a small fraction of the number produced in the collisions. Due to the low geometric acceptance of the detector, most particles missed it completely. Additionally, the detectors were not 100% efficient, and so not all of the particles which passed through the detector were successfully reconstructed. The cuts applied will reduce this number further. These factors must be corrected for in order to find the total yield.

A software simulation of the experiment was used. Monte Carlo particles were generated and were allowed to decay with the decay tracks passing through the simulated apparatus. The detector response was simulated and the resulting "hits" were embedded into background events obtained from the real data. The track-finding routine was used on this data, and the cascade-finding routine were used on the output from the track finder.

4.1.1 Particle Generation and Weight Calculation

The package GEANT [81] was used to generate many Monte Carlo Ξ^- particles for each Ξ^- found in the final sample of the real data after cuts. Each of these had the same rapidity and transverse momentum as the real Ξ^-, but other parameters such as decay angles and decay lengths were randomly chosen to give the same distribution as would be applicable to the real particles. GEANT then tracked the particle and its decay products through the apparatus. Each charged track left a trail of hits in the silicon pixel planes. The detector response, including efficiency, was included in the GEANT simulation. The resulting detector output was in the same format as the real experiment, and was used in the next stage.

It was required that 10,000 generated Ξ^-s were "good", i.e. that the tracks should pass through the compact part of the detector and miss no more than five pixel planes. This typically required around 3 million Ξ^-s to be generated for each Ξ^- to be weighted.

In the real data, each event was observed together with background from noise in the pixel planes and other tracks from the collision. To account for this in the weighting procedure, the simulated detector output from GEANT was embedded into background events from the real data using the MIXRAW package. The output from this procedure resembled a real event containing a Ξ^-. This output was passed through ORHION and CASCADE, as was done for the real data in sections 3.2 and 3.4. This gave the number of successfully reconstructed Ξ^-s.

The weight was calculated by dividing the number of generated particles by the number of successfully reconstructed particles. A weight was calculated for each detected real Ξ^-. The average weight was about 20,000, but this varied considerably with p_t and Y. The major contribution to this large weight is the geometric acceptance of the detector, with selection cuts also making a significant contribution. The effect due to the efficiency of the pixels was small, as the efficiency was

typically above 90% per plane.

4.2 Acceptance region

The NA57 detector only accepted particles in a small range of rapidity and transverse momentum, and the efficiency with which V^0 and cascade particles are reconstructed varies considerably with p_t and Y. The term "acceptance" is used here to refer to the overall ability of the detector to detect and successfully reconstruct particles with a given p_t and Y, and includes geometrical factors, pixel efficiency, reconstruction algorithm efficiency and the effects of selection cuts.

The intention of the analysis was to determine the total yield of particles per unit of rapidity about the central rapidity, which was 2.2 for the 40 GeV/c data set. It was assumed that the rapidity distribution of the particles is flat, but that the distribution of transverse momentum is not and that this must be corrected for. Measurements for Λs at NA57 at higher energy have shown that the variation in the yield over the acceptance region is small, and is therefore unlikely to introduce a large error in the final calculated weight [82].

The acceptance region is defined in terms of transverse momentum and rapidity. A minimum and maximum for these was obtained, together with angles corresponding roughly to the edges of the telescope. For particles with high statistics, such as Λs, the parameters of the acceptance region were obtained by requiring the maximum weight inside the window to be no larger than ten times the minimum weight. This method was not suitable for Ξ^-s as there were only 39 Ξ^-s in the sample. Instead, a Monte Carlo simulation was used.

4.2.1 m_t slopes

As can be seen in figure 4.1, the acceptance region does not cover the full range of p_t. To find a yield, the result must be extrapolated to full p_t. This was done using the transverse mass, defined in equation 4.1:

$$m_t = \sqrt{m^2 + p_t^2} \tag{4.1}$$

where m is the mass of the particle and p_t is the transverse momentum. The distribution of particles was assumed to obey the relation 4.2 [2],

$$\frac{1}{m_t}\frac{d^2N}{dm_t dY} = ke^{-\frac{m_t}{T}} \tag{4.2}$$

where T is a parameter known as the "inverse slope" and k is a constant. For Pb-Pb collisions, which we assume reach thermal equilibrium, T is related to the temperature of the fireball, and the velocity of its expansion. Methods for distinguishing the two effects and obtaining values of temperature and flow velocity, such as the blast-wave model, are available, and this analysis has been done for the NA57 158A GeV Pb-Pb data [83]. The elementary p-p collisions also exhibit this "thermal-like" behaviour [84]. Therefore, equation 4.2 was also used for p-Be with T as the slope parameter. This parameter was fitted to the weighted data using the maximum likelihood method. The result of the fit for the 2001 data is shown in figure 4.2.

4.2.2 Extrapolation to full p_t

An extrapolation factor was obtained which related the number of particles generated in the whole p_t range to the number of particles generated in the acceptance region. This factor was given by the integral of equation 4.2 over the full range of p_t and one unit of rapidity in the central rapidity region divided by the integral of equation 4.2 over the acceptance window, and was evaluated numerically. The sum of weights contained in the window is a measure of number of particles produced in

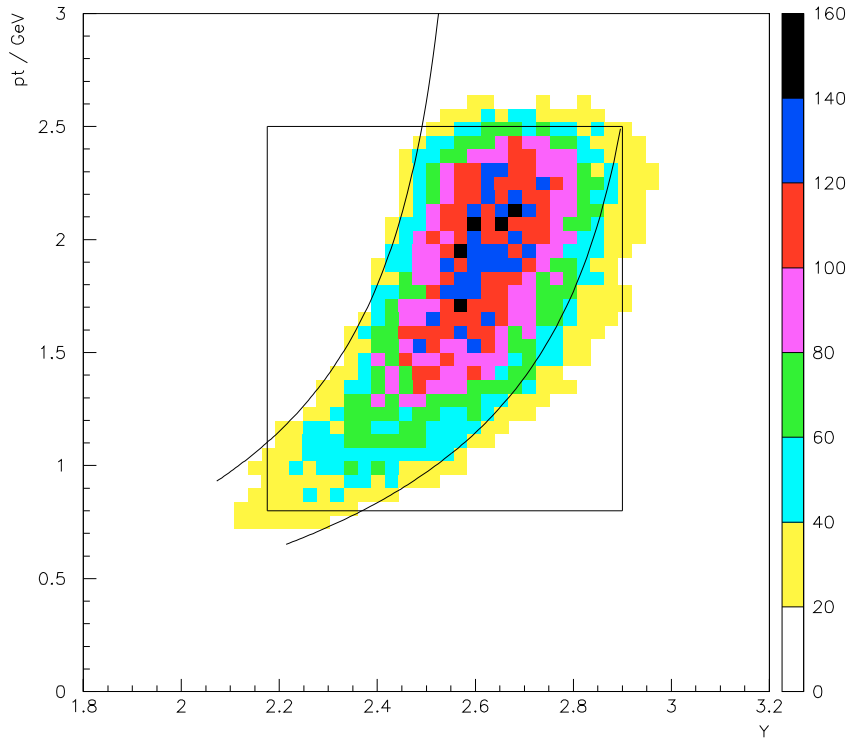

Figure 4.1: Variation of acceptance with rapidity and transverse momentum for Ξ^- particles. The darker regions correspond to greater acceptance. A Ξ^- with p_t and Y in such a region is more likely to be successfully reconstructed than one in a "light" region.

the window. Therefore, to find the total yield, the sum of weights was multiplied by the extrapolation factor.

4.2.3 Monte Carlo determination of acceptance region

Monte Carlo Ξ^-s were generated with a flat distribution over a range of p_t and Y. These were embedded into background events and reconstructed. This method resulted in a high statistics sample which was used to determine acceptance. For this analysis, 10^9 Ξ^-s were generated. Because the distribution was uniform, the acceptance region could be easily determined. It was required that the lowest acceptance regions contain no less than 10% of the number of Ξ^-s in the highest. Figure 4.1 shows the result, with the darker regions corresponding to a greater acceptance.

4.2.4 Test of weighting procedure

As an additional method of identifying the region of good acceptance, a large number of Ξ^-s were generated with a physically realistic inverse slope. Each successfully reconstructed particle was passed through the weighting chain to obtain a weight. The result was used in two ways - firstly, the region of good acceptance was indicated by high weights, as can be seen in figure 4.3. This can be compared with the region determined by the method above. Secondly, the yield calculation procedure can be tested, as it should be possible to calculate the number generated from the weights data.

2001 Data Sample

For the 2001 data simulation, 4×10^9 Ξ^-s were generated per run for 53 different runs, with a uniform distribution in rapidity (Y) from $Y = 1.9$ to $Y = 3.0$. An

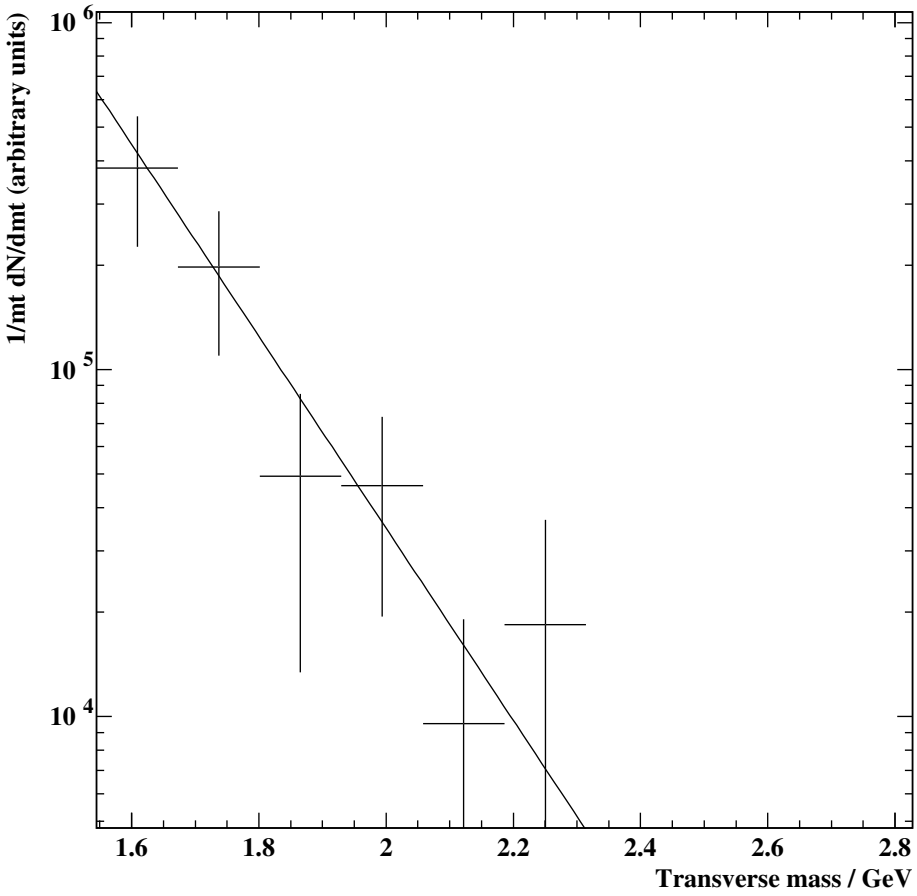

Figure 4.2: Transverse mass fit for 2001 Ξ^-s, with the fitted inverse slope of 157 MeV shown.

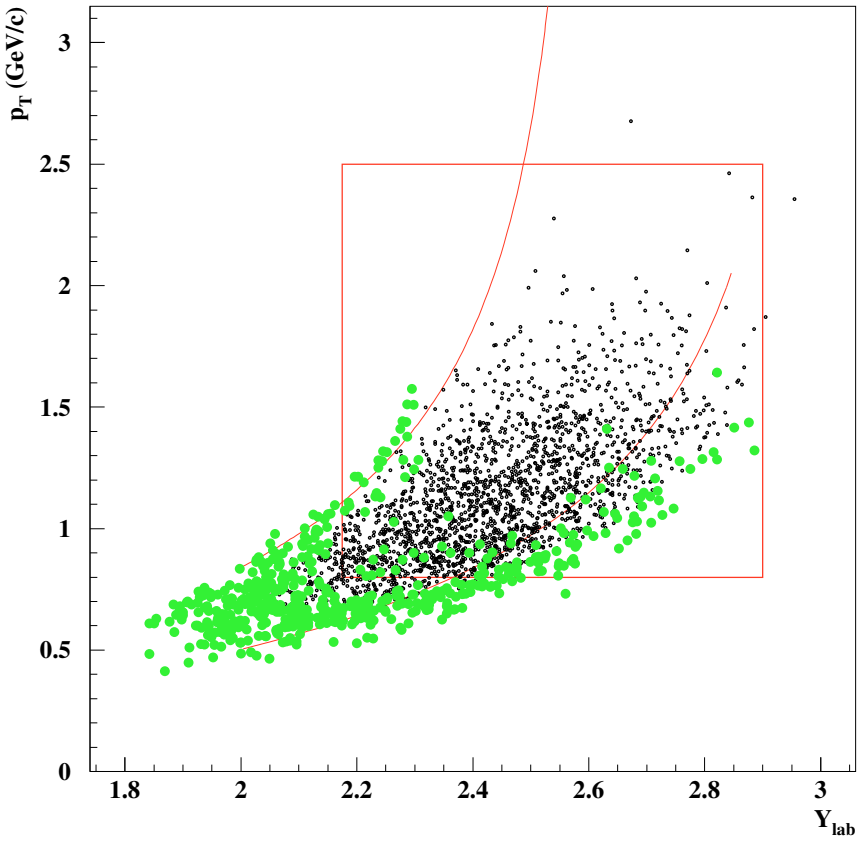

Figure 4.3: Acceptance of Monte Carlo Ξ^- particles for 1999 and 2001 data sets. Each point corresponds to a reconstructed MC Ξ^-. The large circles indicate those Ξ^- particles which were poorly accepted, i.e. where the probability of successful reconstruction is less than a tenth of the probability for the best accepted Ξ^-.

inverse slope of 140 MeV was used as preliminary analysis of the real data suggested that the real inverse slope was similar to this. No cut was applied to transverse momentum. In total, 1.93×10^8 Ξ^-s were generated per unit rapidity. Of these, 876 were successfully reconstructed.

The acceptance window was chosen to exclude most of the high weights while preserving as much "good" data as possible. The parameters chosen are shown in figure 4.3 and in table 4.1. The results obtained are given in table 4.2. The result is compatible with the number generated, which suggests that the method is valid. However, this test cannot exclude the possibility of bugs or discrepancies between

Table 4.1: Acceptance window parameters for the 2001 Monte Carlo Ξ^-s.

	Minimum	Maximum
p_t / GeV	0.80	2.50
Rapidity (Y)	2.175	2.90
Angle / radian	0.098	0.148

Table 4.2: Comparison between generated and reconstructed yield and slope for the 2001 Monte Carlo Ξ^-s.

	Generated	Reconstructed
Inverse Slope (MeV)	140	140.2 ± 5.3
Number Ξ^-s	193×10^6	$(205 \pm 10) \times 10^6$

the Monte Carlo simulation and the physical apparatus.

To test the low-statistics performance, which is relevant to the real data, a subsample of 35 particles was chosen from the full sample of 876. The results are given in table 4.3, and are compatible with the generated values, though obviously with larger statistical errors. The number reconstructed has been multiplied by factor $\frac{876}{35}$ to allow direct comparison with $N_{generated}$.

Table 4.3: Comparison between generated and reconstructed yield and slope for the 2001 Monce Carlo Ξ^-s for a subsample of 35.

	Generated	Reconstructed
Inverse Slope (MeV)	140	134 ± 25
Number Ξ^-s	193×10^6	$(245 \pm 60) \times 10^6$

Table 4.4: Comparison between generated and reconstructed yield and slope for the 1999 Monte Carlo Ξ^-s.

	Generated	Reconstructed
Inverse Slope (MeV)	140.0	142.0 ± 6.5
Number Ξ^-s	108.2×10^6	$(112.2 \pm 6.5) \times 10^6$

1999 Data Sample

The same technique was applied for the 1999 simulation. This time, 10^6 Ξ^- were generated per run for 119 runs, for the same range of Y as for 2001. An inverse slope of 140 MeV was used. The total number of Ξ^-s generated for full p_t and one unit of rapidity was 1.08×10^8. The number of Ξ^-s reconstructed was 704. Therefore, the average weight is smaller than for the 2001 data set. The reconstructed slope and yield are given in table 4.4, and are compatible with the generated values. Figure 4.4 shows the reconstructed transverse mass distribution for the 1999 Monte Carlo Ξ^- particles.

Combined Data Sample

Due to the low statistics, it may be useful to combine the 1999 and 2001 data sets to obtain a single yield value. This procedure was tested using the Monte Carlo used above.

The 704 Ξ^-s for 1999 were combined with the 876 Ξ^-s for 2001. The results are given in table 4.5. The slope is reconstructed correctly, and the number of Ξ^-s is 1.5σ away from the number generated. This is most likely due to the calculated value of N for 2001 also being 1.5σ away from the generated value, and does not indicate any problem with the combination.

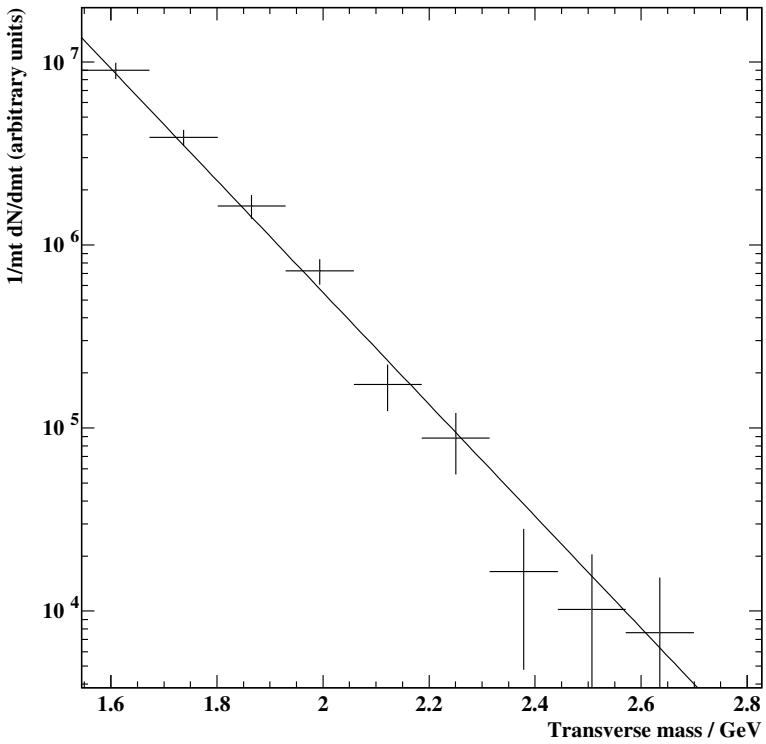

Figure 4.4: Transverse mass fit for 1999 Monte Carlo Ξ^-s.

Table 4.5: Comparison between generated and reconstructed yield and slope for combined MC Ξ^-.

	Generated	Reconstructed
Inverse Slope (MeV)	140.0	139.8 ± 4.2
Number Ξ^-s	302×10^6	$(321 \pm 13) \times 10^6$

4.2.5 Breakdown of weights

The final weight has components due to geometric acceptance, pixel plane efficiency, reconstruction efficiency and cuts. In order to investigate whether the weight was reasonable, some Monte Carlo studies were carried out to determine how much each of the effects above contributed to the weight, and particularly how much of the real signal was lost in the cuts.

Monte Carlo Ξ^-s were generated with a fixed p_t and rapidity. To investigate acceptance, it was required that the decay tracks passed through the compact part of the telescope. Each track was allowed to miss a maximum of one pixel plane. 7.85 million Ξ^-s were generated and 5000 were accepted, giving a weight due to acceptance of 1570. The mixing stage was skipped and ORHION was run directly on the GEANT output. The number of Ξ^-s found by CASCADE using loose cuts was 997. Applying the cut on V^0 vertex position, xvc $<$ -27 cm, to the real data removed the background caused by the scintillators in front of the telescope. Applying it here shows that it also reduces the signal by a factor of two, as 483 Ξ^-s remain after this cut. The original loose cut was xvc $<$ -10 cm. For the real data, events with decay vertices beyond the scintillators did not activate the trigger so nothing can be gained by a loose cut here. The cut requiring V^0 and cascade decay vertices to be separated by at least 2 cm, used to remove "ghost tracks", reduces the signal further from 483 to 355 Ξ^-s, and the internal decay angle cut reduces this further to 181. Therefore, the high weights observed do not seem unreasonable, with low geometrical acceptance accounting for a factor of around 1500. Detector and reconstruction inefficiencies together with cuts account for a further factor of 20-30.

4.3 Yields

In the final samples, 10 Ξ^- candidates were detected for the 1999 run and 29 were detected for the 2001 run. Two $\overline{\Xi}^+$candidates were reconstructed, one in the 1999 data and one in the 2001 data.

The yield was calculated by finding the sum of weights inside the acceptance region, and multiplying it by the extrapolation factor calculated above. This was then divided by the branching fractions for the decays 4.3 and 4.4.

$$\Lambda \rightarrow p\pi^-(63.9\%) \tag{4.3}$$

$$\Xi^- \rightarrow \Lambda\pi^-(99.9\%) \tag{4.4}$$

This, summarised in equation 4.5, gave the total number of Ξ^-s produced per unit rapidity in all events.

$$\text{Yield} = \frac{\Sigma\text{W} \times \text{extrapolation}}{0.639 \times 0.999} \tag{4.5}$$

To obtain a yield per interaction, the total yield was divided by the number of interactions. The number of particles in the beam is measured on a run-by-run basis, along with the fraction of protons in the beam. This fraction was 0.21, with an error of approximately 1%, almost all of which was systematic. The beryllium target was of a size such that there is an 8% probability of a proton interacting in it. The error in this figure was also of the order of 1% and was due to the error in measuring the target thickness. The number of interactions was calculated using equation 4.6.

$$N_{interactions} = N_{beam} \times 0.21 \times 0.08 \tag{4.6}$$

4.3.1 2001 Data

Out of the 29 Ξ^-s in the final sample, 20 were present in the final acceptance region. The sum of their weights was 394962 and the inverse slope was 157$\pm$32 MeV. For this

slope and window, the extrapolation factor was $10.9^{+5.4}_{-2.5}$. The number of interactions for the 2001 sample was 5.385×10^9, and therefore the final yield was $0.00125^{+0.00069}_{-0.00042}$ Ξ^- per unit rapidity. This yield varied by no more than 10% with changes in the acceptance region, and so can be considered stable.

4.3.2 1999 Data

The number of interactions in the 1999 run was 2.02×10^9, much smaller than for 2001. As a result, the sample of Ξ^-s available for the analysis was smaller and the measurement of the yield had a correspondingly larger statistical error. In addition, the small number of Ξ^-s means that the slope's error was too large to be useful. The calculated inverse slope was 403 ± 233 MeV, and is unstable when small changes are made to the acceptance region. Therefore, the 1999 data was not useful by itself, but it may be reasonable to combine it with the 2001 data with appropriate weighting for each of the data sets.

By using the slope that was calculated from the 2001 data, together with the 2001 acceptance window, a yield can be calculated. The sum of the weights in the window is 149200. If this is used with the extrapolation factor calculated for the 2001 data, the result is a yield of $0.00126^{+0.00078}_{-0.00070}$ Ξ^- particles per unit of rapidity.

4.3.3 Combined Data

The acceptance window parameters used were the same as those obtained for the Monte Carlo study, and are shown in table 4.1. This acceptance region, containing both the 1999 and the 2001 data points, is shown in figure 4.5.

The simplest way to combine the results is to take a weighted average, with the error reduced due to the higher statistics. As the statistical errors on the yields are the same, the weighted average is $0.00125^{+0.00068}_{-0.00041}$. However, this error is statistical

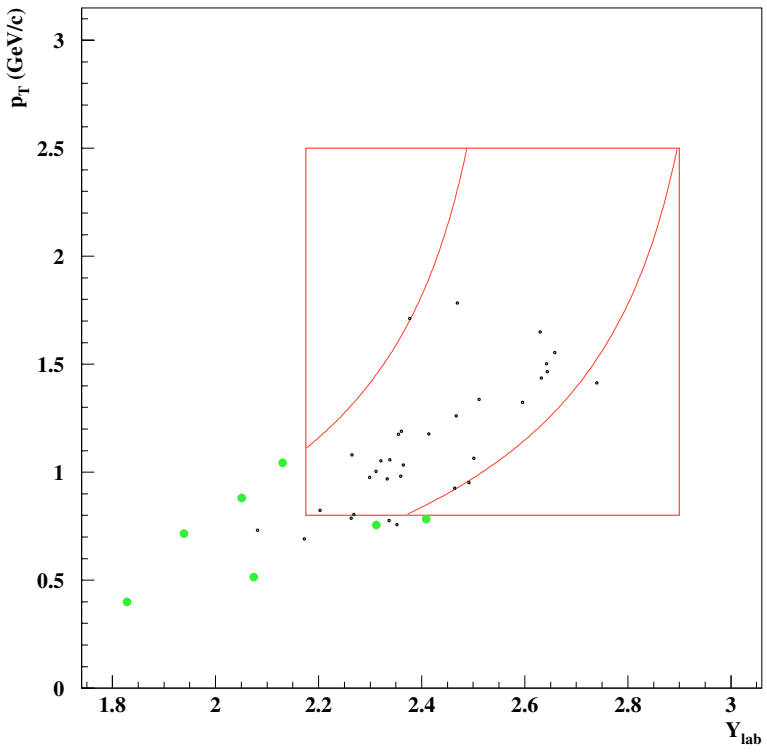

Figure 4.5: Acceptance region containing the 1999 and 2001 Ξ^- candidates. The large dots indicate weights greater than ten times the smallest weight. The lower curve indicates the lower angle.

only and does not account for any systematic difference that could be present between the two data samples. In the case of a systematic difference, this error would be an underestimate.

4.3.4 Results summary

A summary of the results is given in table 4.6. The extrapolated yields refer to the yields per event in one unit of rapidity and for all transverse momenta. The WA97 experiment investigated p-Be collisions at 158 GeV/c and measured a Ξ^- yield of 0.0015 ± 0.0003 [85] with an inverse slope of 202 ± 13 MeV [86]. A comparison with the results obtained here indicates that the Ξ^- yields at 40 GeV/c and 158 GeV/c are the same within errors. The number of $\overline{\Xi}^+$candidates was too small to allow a calculation of yield and inverse slope.

Table 4.6: Summary of Ξ^- yield and inverse slope measurements in p-Be collisions at 40 GeV/c and a comparison with the WA97 p-Be results at 158 GeV/c. The extrapolated yields for the 1999 and 2001 data sets were calculated assuming the inverse slope from the 2001 data set.

	1999 Data	2001 Data	WA97 Data
Yield in acceptance	$1.16 \pm 0.61 \times 10^{-4}$	$1.15 \pm 0.28 \times 10^{-4}$	-
Extrapolated yield	$0.00126^{+0.00078}_{-0.00070}$	$0.00125^{+0.00069}_{-0.00042}$	0.0015 ± 0.0003
Inverse slope / MeV	404 ± 233	157 ± 32	202 ± 13

4.4 Enhancements

By comparing the yield calculated above to the yield obtained in Pb-Pb collisions at the same energy, a factor of "strangeness enhancement" can be obtained. The

Table 4.7: Yields in Pb-Pb collisions at 40 GeV/c per nucleon.

Bin	% of σ_{tot}	$< N_{wound} >$	Yield
0	42-56%	57	0.077 ± 0.026
1	25-42%	119	0.306 ± 0.048
2	12-25%	208	0.713 ± 0.078
3	5-12%	292	1.746 ± 0.207
4	0-5%	346	1.989 ± 0.305
p-Be 2001	-	2.5	$0.00125^{+0.00069}_{-0.00042}$
p-Be 1999	-	2.5	$0.00126^{+0.00078}_{-0.00070}$
p-Be Combined	-	2.5	$0.00125^{+0.00068}_{-0.00041}$

yields are normalised to yield per event per wounded nucleon, with the number of wounded nucleons calculated by the Glauber model [87]. If the nucleus-nucleus collision behaves as nothing more than the sum total of the individual nucleon-nucleon interactions, the normalised yield should be the same for Pb-Pb and p-Be and there will be no strangeness enhancement. If the normalised yield for Pb-Pb collisions is larger than for p-Be collisions then strangeness enhancement is present. The analysis of the Pb-Pb data is described in [88].

Yields in Pb-Pb collisions at 40 GeV/c per nucleon are given in table 4.7 [89, 90]. The Pb-Pb collisions are divided into five centrality bins, with bin 4 containing the 5% most central collisions. The Glauber model is used to calculate the number of participating nucleons. The normalised yields are given in table 4.8, together with strangeness enhancement factors for the different centrality classes. The enhancements quoted here and in figure 4.6 are based on the 2001 p-Be result.

Figure 4.6 shows a plot of strangeness enhancements when going from p-Be to Pb-Pb collisions of varying centrality, and can be compared to the enhancement in 158 GeV/c collisions shown in figure 4.7 [31]. There is strong evidence for enhancement

Table 4.8: Ξ^- yields per unit rapidity per wounded nucleon and enhancements in Pb-Pb and p-Be collisions at 40 GeV/c per nucleon.

	Normalised Yield	Enhancement
p-Be	0.0008	1
Pb-Pb Bin 0	0.00135	$2.7^{+1.3}_{-1.8}$
Pb-Pb Bin 1	0.00257	$5.1^{+2.0}_{-3.0}$
Pb-Pb Bin 2	0.00343	$6.9^{+2.5}_{-3.9}$
Pb-Pb Bin 3	0.00598	$12.0^{+4.3}_{-6.9}$
Pb-Pb Bin 4	0.00575	$11.5^{+4.3}_{-6.7}$

in central Pb-Pb collisions, and evidence that enhancement increases with collision centrality.

4.5 Conclusions

A strong enhancement of Ξ^- particles is observed in Pb-Pb collisions at 40 GeV/c when compared to pp collisions. The enhancement in central collisions is of a similar size to the enhancement in 158 GeV/c collisions. The results for the more peripheral collisions suggest a lower enhancement than at 158 GeV/c. However, the errors are large, particularly in the p-Be yield measurement, and so a definite statement is not possible. Enhancements for Λ particles are required to give a more complete picture, but the Ξ^- enhancement provides some evidence that the QGP can be formed at this lower energy. This result is more consistent with the QGP than with the canonical suppression model of strangeness enhancement, as the canonical suppression model predicts that the enhancement will be much higher at the lower SPS energy than at the higher energy [33]. However, large errors make a definite conclusion difficult. The strangeness enhancement results are discussed further in chapter 7.

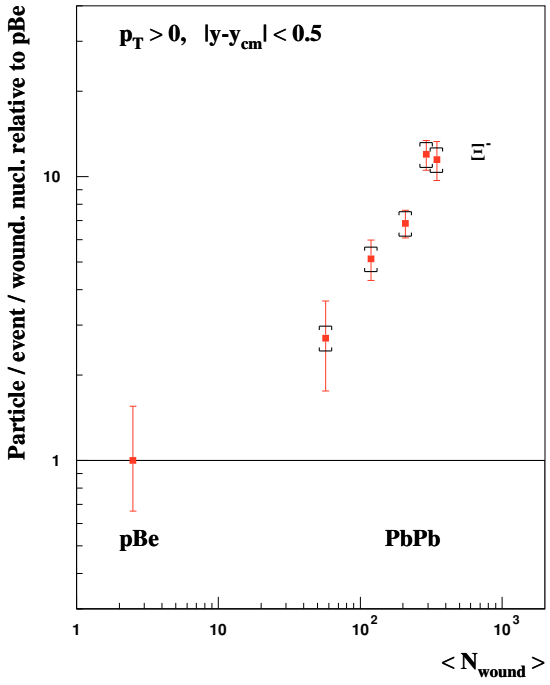

Figure 4.6: Enhancement of Ξ^- going from p-Be to Pb-Pb collisions at 40 GeV/c per nucleon.

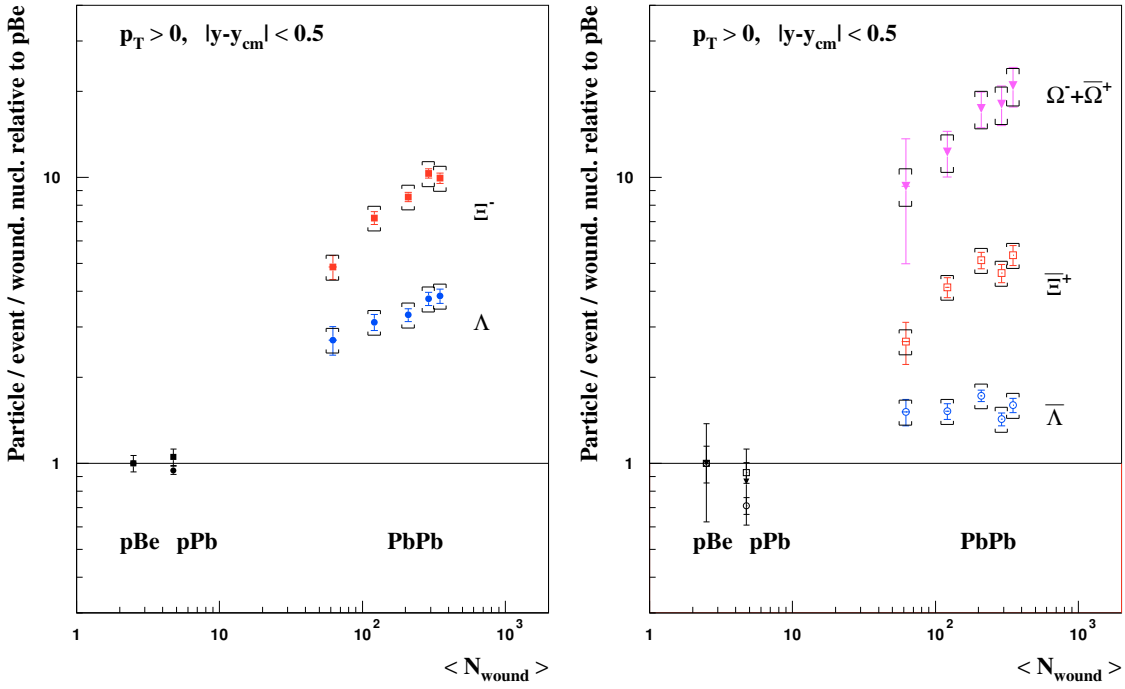

Figure 4.7: Enhancement of Ξ^- going from p-Be to Pb-Pb collisions at 158 GeV/c per nucleon.

Chapter 5

Monte Carlo simulations at ALICE

5.1 Introduction

The subject of the second part of this thesis is the analysis of ρ^0 resonance production at ALICE. This required the generation, simulation and reconstruction of a large number of pp and Pb-Pb collisions at LHC energies. The standard ALICE software provides a way to do this, but it was too slow to generate a sufficiently large sample of events for this analysis. Therefore it was necessary to develop a fast simulation method before the ρ^0 analysis could be performed. Relevant results from the standard ("detailed") simulation were used to develop this fast simulation routine, and these results, together with their consequences for the fast simulation routine, are described here.

The fast simulation method is then described, based on and justified by the results obtained from the full simulation. The use of this fast simulator to study the ρ^0 resonance at ALICE is described in the following chapter.

5.2 Simulation of events

To investigate the physics capabilities of ALICE before data taking takes place, it is necessary to run simulations. The simulation has two separate stages - simulation of the physics processes in the collision, and simulation of the response of the detector to these events. The physics processes are simulated using the Monte Carlo generators PYTHIA [91] and HIJING [92], and the detector response is simulated using the particle tracking package GEANT3 [81]. The results from the simulations are then processed using the same reconstruction methods as used for the real data.

It is important to note that the predictions of these generators are subject to large uncertainties at LHC energies, and the actual signals and backgrounds may be very different to the predicted ones. Therefore, the generator output serves as a rough estimate, not a precise prediction.

The generated primary particles are decayed into "stable" particles, i.e. ones which do not decay via the strong interaction, by the generator, and the resulting particles are passed to the next stage for tracking through the apparatus.

5.2.1 The PYTHIA Monte Carlo generator

The PYTHIA Monte Carlo generator is used to simulate the physics of p-p collisions, and a detailed description of the physics simulated is described in the PYTHIA reference manual [91]. A very brief summary of the relevant physics is presented here.

Simulation of initial interaction

A large number of physics processes are included in the simulation, e.g. QCD processes such as $gg \rightarrow q\bar{q}$. Perturbative methods are used to perform calculations

for the different contributions of such processes, taking into account the parton distributions of the beam particles. Soft QCD processes, which cannot be calculated this way, are simulated using various models [91].

Hadronization

The formation of colourless hadrons from coloured partons is not understood from first principles, so PYTHIA makes use of a phenomenological model known as "string fragmentation" in the form of the Lund model [91]. This is based on the linear model of confinement, where the potential between two quarks increases linearly with separation. A "string" is considered as present between these quarks, which can break up to form new $q\bar{q}$ pairs when it is energetically favourable to do so. The details of this process as used by PYTHIA are described in the PYTHIA reference manual.

Finally, decays of the resonances such as $\rho^0 \rightarrow \pi^+\pi^-$ are performed, using branching fractions and widths obtained from previous experiments.

5.2.2 The HIJING Monte Carlo generator

The HIJING Monte Carlo generator can be used to simulate the physics of proton-proton, proton-ion and ion-ion collisions [92]. It is based on the PYTHIA routines, and uses the same hadronization models as PYTHIA. It models features specific to heavy ion collisions, such as multiple minijets, nuclear shadowing and jet interactions in a dense medium [92].

For this analysis, HIJING was used to generate a sample of Pb-Pb events at LHC energies in order to study the performance of the ALICE detector for ρ^0 meson measurement.

5.2.3 Simulation of ALICE detector response

The tracking was performed by GEANT3 [81], which was also used for the NA57 weighting procedure described in chapter 4. GEANT3 simulates weak and electromagnetic decays, as well as interactions with material in the detector. If a particle travels through a sensitive part of the detector, the signal produced in response is simulated. These particular interactions are known as "hits", and the resulting signals are stored and are used by the reconstruction code, thus simulating the reconstruction of real data.

5.2.4 Reconstruction of events

In order to perform the analysis, it was necessary to convert the recorded detector signals into track information. The algorithm is described in detail in chapter 5 of the ALICE Physics Performance Report [93], and is summarised briefly below.

Tracking begins in the outer radius of the TPC. Firstly, the TPC signals are processed to form "clusters". Track candidates, known as seeds, are identified from the clusters, and the track fitting attempt begins at a seed and proceeds towards the inner radius of the TPC. New clusters are associated with the track candidate using the Kalman filter method [93], updating the track parameters as new clusters are discovered. When the inner radius of the TPC is reached, the fitting then passes to the ITS, which attempts to trace the tracks to the primary vertex. The ITS clusters are used to refine the track parameters.

The tracking is then restarted, beginning at the primary vertex and tracking outwards to the outer wall of the TPC, and then out further to the TRD, TOF and other detectors, which contribute tracking and PID information. Finally, the tracks are refitted back to the primary vertex, or as close as is possible.

5.3 The PYTHIA Monte Carlo generator's predictions of the ρ^0

The ρ^0 resonance has a mass of 771.1$\pm$0.9 MeV and a width of 149.2$\pm$0.7 MeV [19]. It decays primarily to $\pi^+\pi^-$ with a branching fraction very close to 100% [19], and this is the channel which was investigated. The large ρ^0 width and high multiplicity of pions in each event mean that the background was very large.

A sample of 100,000 PYTHIA pp events was generated. This event sample contained a total of 586,686 ρ^0s, corresponding to an average of 5.87 ρ^0s per event. The rapidity distribution is shown in figure 5.1, and it can be seen that the ρ^0s were generated with a wide range of rapidities. In order for a ρ^0 to be successfully reconstructed, it is necessary for both its decay tracks to be within the geometrical acceptance of the detector, i.e. their pseudorapidities must both be between -0.9 and +0.9. Of the 5.87 ρ^0s per event generated, 0.489 satisfied this criterion, representing a geometric acceptance of 8.3%. The rapidity distribution of these "reconstructable" ρ^0s is shown in figure 5.2. This corresponds to a potential sample of 489,000 ρ^0s per million events in the $\rho^0 \to \pi^+\pi^-$ channel and approximately 25 ρ^0s per million events in the $\rho^0 \to e^+e^-$ channel. The actual number reconstructed was somewhat lower due to inefficiencies and cuts.

The p_t distribution of the generated ρ^0s is shown in figure 5.3. The fraction of the ρ^0s in several p_t sub-regions is shown in table 5.1. This was obtained using a different sample of PYTHIA pp events, but the generator version and settings were the same as those used for the main sample, described above.

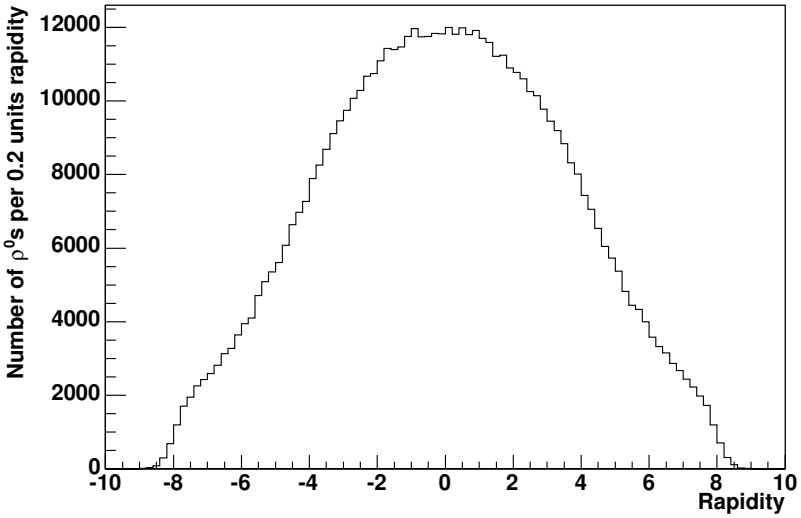

Figure 5.1: Rapidity distribution of generated ρ^0 particles for 10^5 PYTHIA pp events.

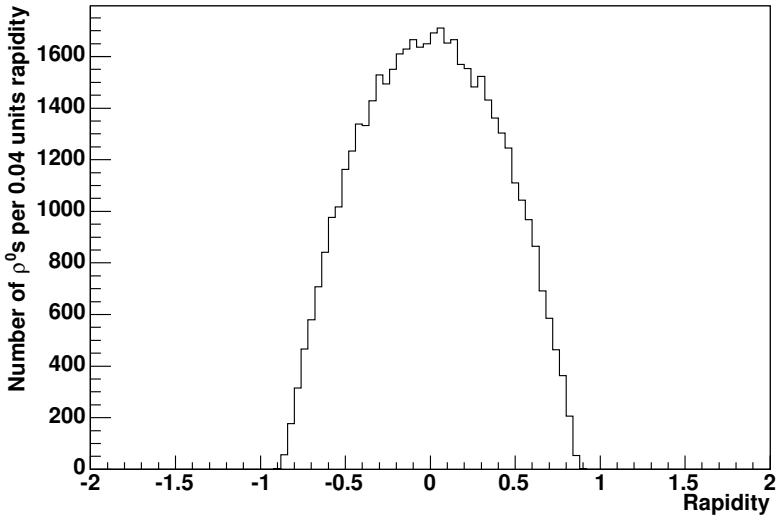

Figure 5.2: Rapidity distribution of generated ρ^0 particles for 10^5 PYTHIA pp events, where the ρ^0 decay tracks have pseudorapidities within the TPC acceptance of $-0.9 < \eta < 0.9$.

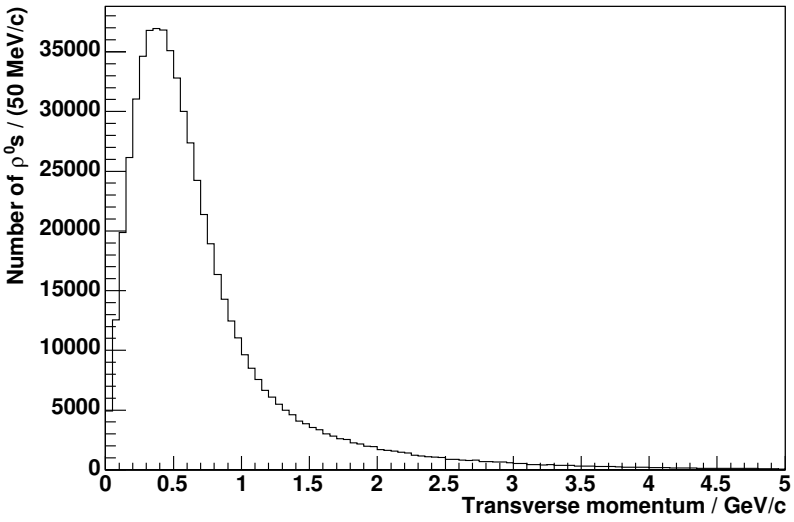

Figure 5.3: Transverse momentum distribution of generated ρ^0 particles for 10^5 PYTHIA pp events.

Table 5.1: Table showing the fraction of generated ρ^0s in several p_t sub-regions.

p_t / GeV/c	Number	Percentage
All	583,600	100 %
0-1	463,500	79.4 %
1-3	109,300	18.7 %
3-5	9,190	1.57 %
5-10	2,080	0.36 %
Above 10	161	0.03 %

5.4 Properties of reconstructed events

5.4.1 Primary and secondary tracks

The output from the reconstruction routine consists of a reconstructed event, which contains a list of reconstructed tracks. Some of the tracks will originate from the

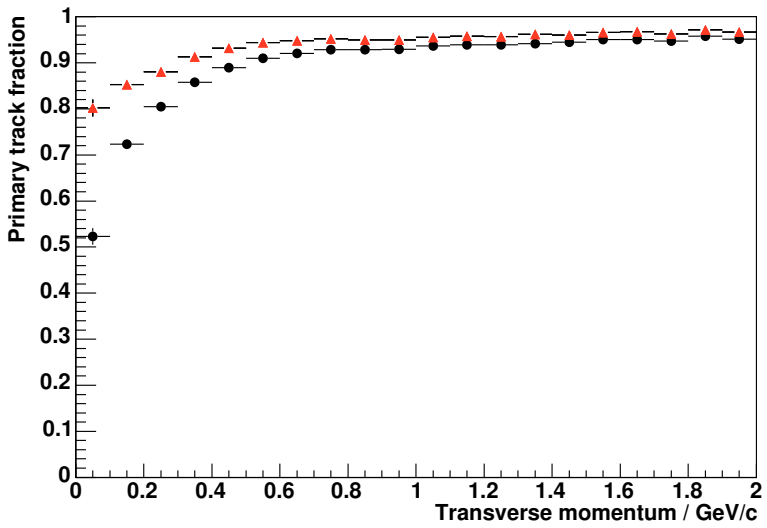

Figure 5.4: Ratio of primary tracks to total tracks for tracks satisfying the ITS fitting requirement, divided into 100 MeV/c bins, with no impact parameter cut imposed. The black circles are the values for all particle species and the red triangles are the values for pions only.

collision, and are known as primary tracks. Some will be the result of decays, or interactions in the detector material, and these are known as secondary tracks. As resonances decay at the primary vertex, it is the primary tracks that are of interest for resonance analysis. Secondary tracks will result in additional background, and should be removed as far as is practical.

To investigate this, a sample of HIJING central Pb-Pb events was generated using the detailed simulation, as described in section 5.2. A list of reconstructed tracks was obtained. It was required that these tracks were successfully fitted in both the TPC and ITS according to the procedure described in section 5.2.4. This was necessary in order to allow impact parameters to be calculated, and the refit requirement alone eliminated a large fraction of the secondary tracks.

Figure 5.4 shows the ratio of primary tracks to total tracks as a function of transverse momentum, divided into 100 MeV/c bins. Tracks are identified as "primary"

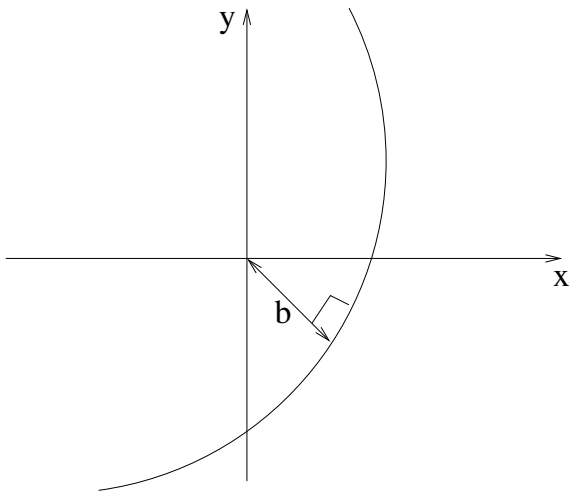

Figure 5.5: The impact parameter in the x-y plane.

or "secondary" using the Monte Carlo "truth" information supplied by the generator, although this will not be possible for the real data. It is clear that secondary particles are relatively more abundant at low p_t, and that the ratio flattens out at moderate p_t.

Impact parameter cut

To reject non-primary tracks, a cut on the value of the impact parameter was used. Two impact parameters are defined - an impact parameter in the x-y plane, shown in figure 5.5 and known as the transverse impact parameter, and an impact parameter in the z plane. The z impact parameter is calculated by finding the z position at the point of closest approach in the x-y plane.

However, a simple cut on the impact parameter does not take into account the variation of the error in the measurement of impact parameter. A tighter cut can be used if the error is small, whereas the same cut would reject many genuine primary tracks if the tracks have large errors in the impact parameter. The impact parameter resolution is a strong function of p_t - for example, in central Pb-Pb collisions the resolution of the transverse impact parameter is about 60 μm for 1 GeV/c pions

but about 200 μm for 300 MeV/c pions [93]. To account for this, the reconstruction and fitting routine calculates the χ^2 for the track's point of closest approach to the primary vertex assuming that the primary vertex should be a point on the track. Large values of this χ^2 indicate that the track does not originate from the primary vertex.

A cut on this χ^2 was investigated for a sample of tracks from the HIJING Pb-Pb events described above. Tracks which cannot be constrained to the primary vertex, such as secondary tracks which are produced far from the primary vertex and do not trace back to it, are arbitrarily assigned a very large χ^2 of 10^{10} by the reconstruction software.

In the sub-sample investigated, there were 1939 reconstructed non-primary tracks and 11,989 reconstructed primary tracks. If the cut to remove the tracks for which χ^2 is not calculated was applied, 632 non-primary and 11,706 primary tracks remained in the sample. Therefore, the rejection of tracks with a very large χ^2 eliminated 67% of the non-primary tracks and only about 2.4% of the primary tracks. The resulting sample consisted of about 5.1% secondary tracks. Figure 5.6 shows the primary track fraction for tracks after this cut, with the pion data points indicated by the red triangles. This shows that, for pions, the primary fraction wass over 97% over all the p_t range. The primary fraction for all reconstructed tracks after these cuts was above 95% for p_t greater than about 400 MeV/c and was above 85% even at low p_t.

A stricter cut could of course be used, and this will improve the signal-to-background ratio at the expense of the statistics. Therefore, a compromise is required between the need for a pure selection of tracks and the need for a large sample. A useful quantity for this purpose is the signal significance, which is the number of ρ^0s divided by the statistical fluctuation of the number of ρ^0s plus the

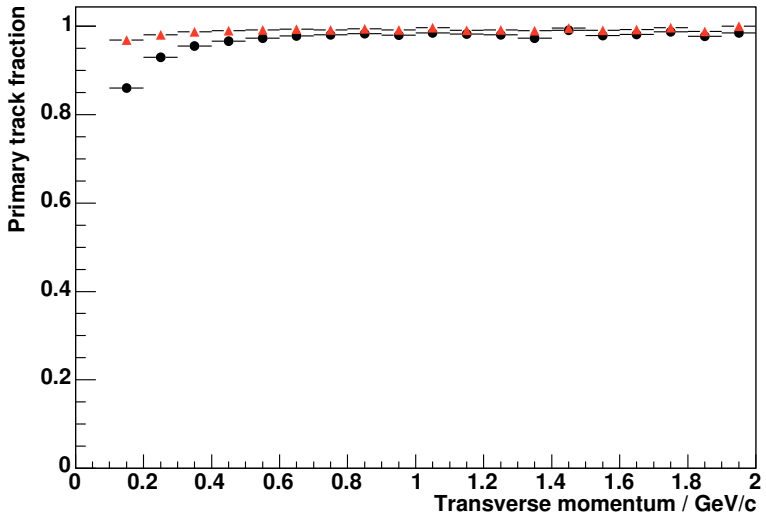

Figure 5.6: Ratio of primary tracks to total tracks for tracks satisfying the ITS fitting requirement and the χ^2 cut, divided into 100 MeV/c bins, with no impact parameter cut imposed. The black circles are the values for all particle species and the red triangles are the values for pions only.

number of background pairs. The significance is given by:

$$\text{Significance} = \frac{\text{S}}{\sqrt{\text{S} + \text{B}}} \tag{5.1}$$

where S is the number of ρ^0s in the relevant mass region and B is the number of background pairs in the same mass region. Essentially, the significance is the factor by which the signal stands out over the statistical noise. Significance can be improved by increasing the number of events, as it is proportional to $\sqrt{N_{events}}$.

Applying a cut to reject secondary tracks may improve the significance as the background (B) term in equation 5.1 is decreased. However, such a cut also removes some primary tracks and therefore decreases the signal (S). Therefore, beyond some point, the signal significance will decrease with increasing tightness of cut. For this analysis, as the contamination was small, the cut was restricted to removing only tracks which were assigned the extremely large χ^2 value. Any further cut reduced the statistics for little gain in reduced contamination.

5.4.2 Relative abundances of particle species

Using a sample of reconstructed tracks from PYTHIA pp events, the relative abundances of the various particle species were obtained. Of the charged tracks, only electrons, muons, pions, kaons and protons are sufficiently long lived to travel through the detector. As shown in table 5.2, almost all of the electron and muon tracks were

Table 5.2: Relative abundances of the particle species of reconstructed tracks, obtained from a sample of PYTHIA pp events.

Particle type	Number (total)	Number (primary)
e^+ and e^-	2681	23
μ^+ and μ^-	5188	4
π^+ and π^-	38269	33564
K^+ and K^-	2859	2844
p and $\bar{p}$	3651	1569

secondary. Of the 2681 electron tracks, 2459 originated from γ conversions. Of the 5188 muon tracks, 4173 originated from the decay $\pi \to \mu\nu$ and 958 originated from the decay $K \to \mu\nu$.

Before cuts, therefore, the electrons and muons gave a similar contribution to the tracks as the kaons and protons. Electrons and muons together are approximately 20% as abundant as pions. However, unlike kaons and protons, almost all of the lepton tracks were secondary and there was potential for removing them using impact parameter based cuts.

A loose cut on the χ^2 parameter described in section 5.4.1 eliminated 83% of the electrons and 97% of the muons. Stricter cuts may be possible, however even this loose cut reduced the number of muon tracks to well under 1% of the pion tracks and the number of electron tracks to approximately 1% of the pion tracks.

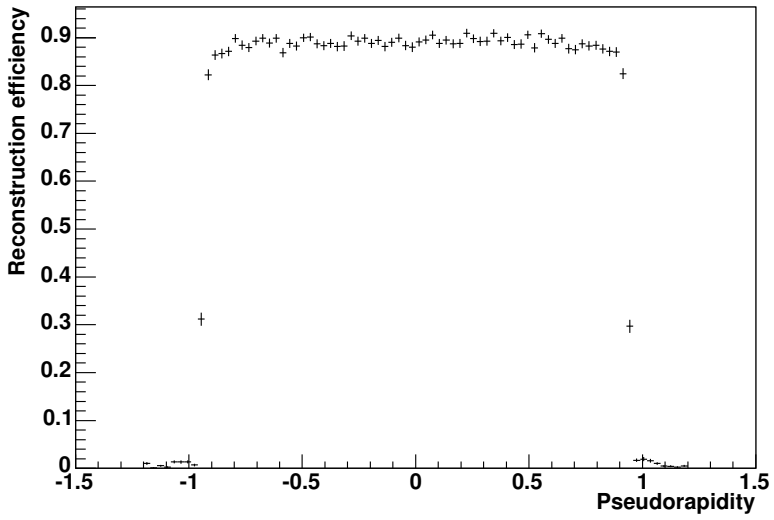

Figure 5.7: Reconstruction efficiency as a function of pseudorapidity for tracks from PYTHIA pp events which have p_t above 0.2 GeV/c and are either π^+, K^+ or p or their charge conjugates.

5.5 Detector acceptance and efficiency

5.5.1 Efficiency as a function of pseudorapidity

The geometric acceptance of the main sub-detectors of ALICE corresponds to a pseudorapidity range of $-0.9 < \eta < 0.9$. Therefore, it is expected that the reconstruction efficiency is zero for tracks outside this range, and should be large and not vary significantly inside this range. Figure 5.7 shows the reconstruction efficiency as a function of η for tracks which are either pions, kaons or protons and have p_t over 0.2 GeV/c. This result was obtained using a sample of PYTHIA pp events which were simulated using the detailed detector simulation and reconstruction. Figure 5.8 shows the efficiency obtained from a sample of HIJING central Pb-Pb events.

These plots clearly show a flat reconstruction efficiency within the geometric acceptance, an approximately zero efficiency outside this and a very rapid transition

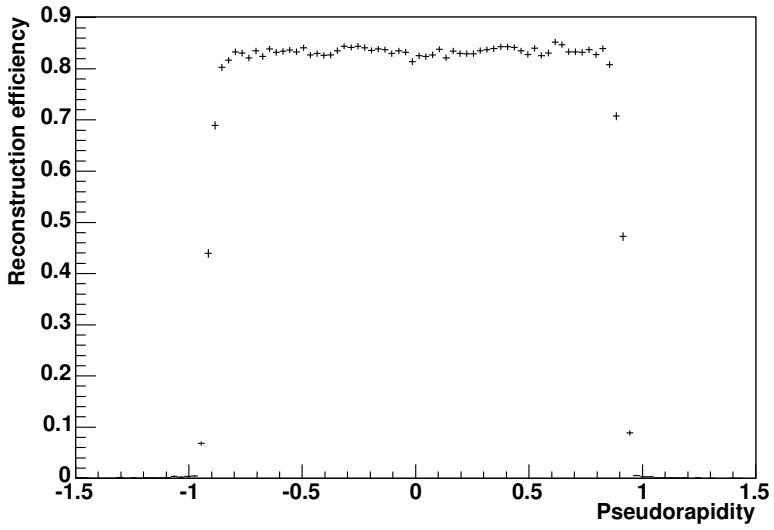

Figure 5.8: Reconstruction efficiency as a function of pseudorapidity for tracks from HIJING central Pb-Pb events which have p_t above 0.2 GeV/c and are either π^+, K^+ or p or their charge conjugates.

between the two. These results indicate that the efficiency as a function of η can be modelled using a "top hat" function, with zero efficiency for $\eta < -0.9$ or $\eta > 0.9$ for both pp and Pb-Pb events.

5.5.2 Efficiency as a function of transverse momentum

In order to be reconstructed, a track must reach the TPC and leave hits there. The radius of curvature for a track in the magnetic field is given by $p_t = 0.3\mathrm{Br}$, where p_t is transverse momentum in GeV/c, B is magnetic field strength in Tesla and r is radius in metres. A track with 0.85 m radius, roughly corresponding to the inner radius of the TPC, in a 0.5 T field corresponds to a p_t of about 130 MeV. Particles with p_t less than this will not reach the TPC and are not reconstructed by the standard ALICE reconstruction routines, though reconstruction using the ITS only may be possible. For the low p_t tracks which do reach the TPC, the efficiency at low momentum is lower than at high momentum due to energy loss, interactions in

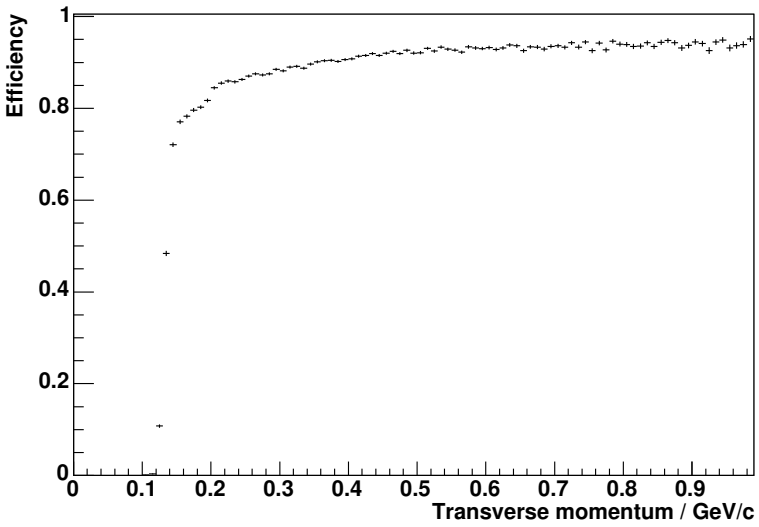

Figure 5.9: Reconstruction efficiency as a function of transverse momentum for pion tracks from PYTHIA pp events which have η between -0.7 and +0.7.

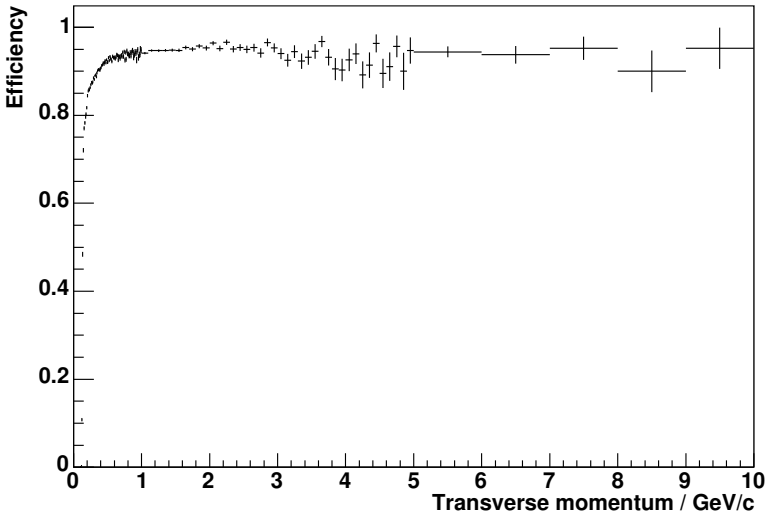

Figure 5.10: Reconstruction efficiency as a function of transverse momentum for pion tracks from PYTHIA pp events which have η between -0.7 and +0.7.

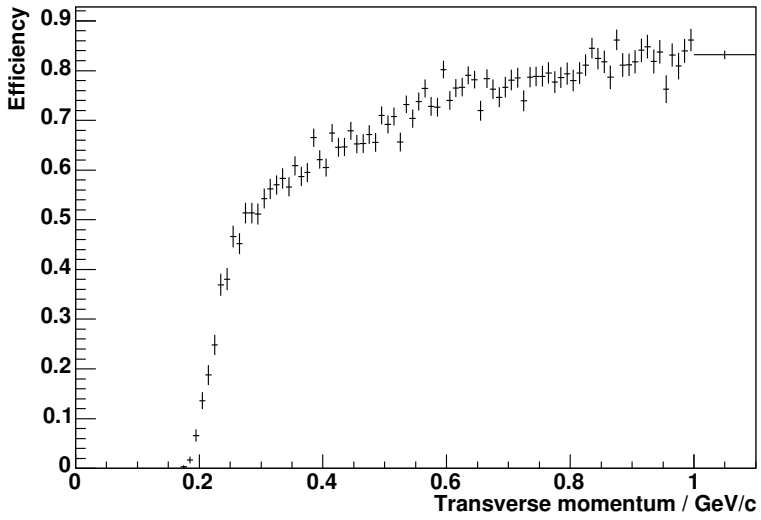

Figure 5.11: Reconstruction efficiency as a function of transverse momentum for kaon tracks from PYTHIA pp events which have η between -0.7 and +0.7.

the material, and decays [93].

Figures 5.9 and 5.10 show the reconstruction efficiency as a function of p_t for pions with pseudorapidity $-0.7 < \eta < 0.7$. As can be seen, the efficiency is zero for p_t below about 120 MeV/c, rises rapidly to over 80% at 200 MeV/c, then increases slowly to reach a maximum of about 95%, and is then flat to beyond 5 GeV/c.

By comparing figure 5.9 with figure 5.11, it can be seen that the efficiency varies with particle species.

5.6 Track momentum resolution

5.6.1 Errors in reconstruction

Measurements of track position and momentum are subject to random and systematic errors. Momentum measurements are performed by measuring track curvature

in a magnetic field. Therefore, errors associated with measuring the position of the track and errors in measurement of the magnetic field map will introduce errors into the momentum measurement. Multiple scattering and energy loss as particles interact with matter in the detector will also reduce the accuracy of the momentum measurement for the same reason, and this effect is particularly strong at low momentum.

These errors will result in errors in the reconstructed mass and other properties, and have a direct effect on the quality of results. In addition to the obvious problems due to systematic errors, a large random error in reconstructed mass will increase the error in the measured value of the particle's mass and will also increase the background as a wider mass cut must be used. For weakly decaying particles, the experimental resolution is the only contributor to the width in the reconstructed mass. For resonances, the particle's natural width is often, but not always, large compared to the width due to measurement errors.

To study these errors, a sample of PYTHIA Monte Carlo pp events, reconstructed using the detailed simulation, was analysed.

5.6.2 Errors in calculation of resonance properties

The momentum of the decay tracks is used to calculate the resonance momentum components, transverse momentum, mass and rapidity. Errors in measurements of track momentum will therefore propagate through to other quantities and the final fractional error may be much larger than the fractional error in the track momentum measurement. For example, a resonance with a p_t of 100 MeV/c may decay to tracks with p_t of several hundred MeV, with correspondingly larger absolute errors, which combine to give a large error in the p_t of the resonance. Reconstructed mass and rapidity, which are calculated from measured track momenta, are affected in a similar way.

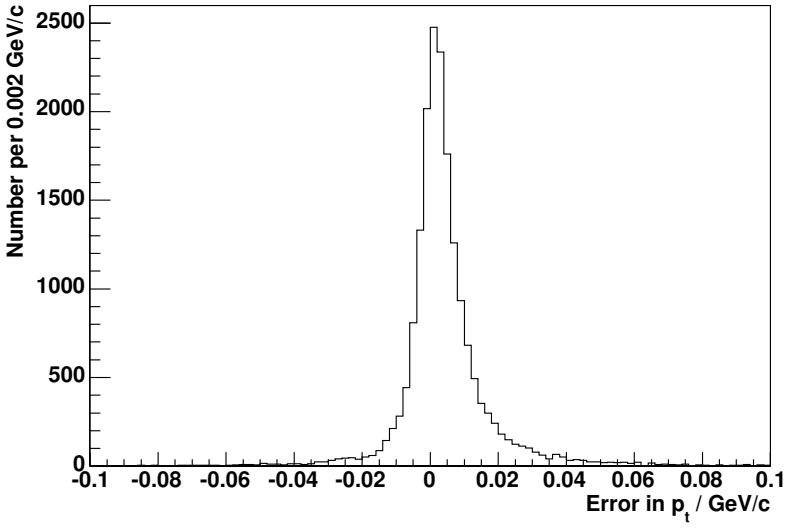

Figure 5.12: Errors in measurement of ρ transverse momentum, defined as the reconstructed p_t minus the generated p_t. There is a shift of +4.1 MeV/c and a random error with an RMS value of 14.0 MeV/c.

Figure 5.12 shows the distribution of errors in the reconstructed value of p_t for reconstructed ρ. The FWHM (full width at half maximum) is approximately 12 MeV.

Figure 5.13 shows the error in the reconstructed mass of ρ particles. The FWHM for the peak is approximately 11 MeV. This shows that the error is small compared to the natural width of the ρ resonance, and so will not significantly affect the analysis. There is also a systematic error, causing the reconstructed mass to be 2.1 MeV higher than the generated mass.

The error in rapidity is shown in figure 5.14. The FWHM value is approximately 0.005 units of rapidity as can be seen in figure 5.14.

The errors in ρ^0 mass, p_t and rapidity originating from track momentum measurement errors are small. The error in p_t is of the order of 10 MeV/c as compared to a typical p_t of a few hundred MeV/c. The error in the ρ^0 mass is about 6 MeV/c^2, which is small compared to the typical ρ^0 mass of 770 MeV/c^2. This error, however,

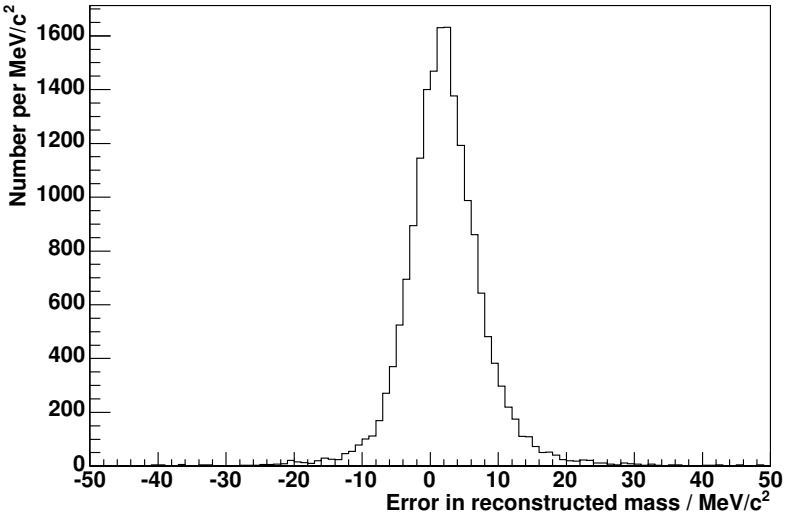

Figure 5.13: Errors in reconstructed ρ^0 mass. There is a shift of +2.1 MeV/c^2, a random error with an RMS value of 6.4 MeV/c^2.

will increase the width of the observed ρ^0, and this must be taken into consideration if the width is to be measured. However, the natural width of the ρ^0 is about 150 MeV/c^2, so the width due to momentum smearing is an order of magnitude smaller. The consequence of these results is that the momentum smearing does introduce errors in the quantities which are to be measured, but these effects are small and so the errors can be modelled quite approximately without significantly affecting the important results from the ρ^0 analysis.

5.7 Particle identification

The ALICE detector provides excellent facilities for identifying particles. Each sub-detector may provide information which may help to identify a particle, for example:

- The ITS and TPC provide dE/dx measurements, and so can identify particles as the dE/dx value is mass-dependent [93].

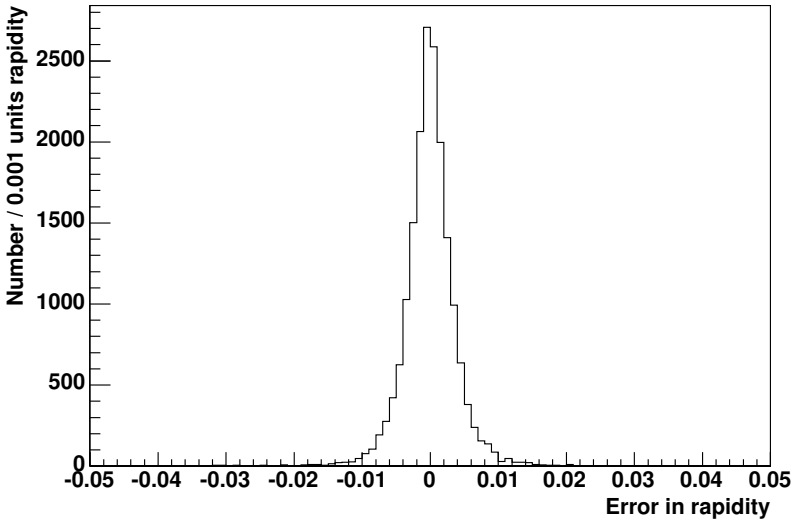

Figure 5.14: The distribution of error, defined as the reconstructed value minus the generated value, in the reconstructed ρ^0 rapidity values. There is a shift of -6.8×10^{-5} units of rapidity and a random error with an RMS value of 0.0046 units of rapidity.

- The TOF provides timing information, and so can provide information on a particle's velocity as well as its momentum, allowing its mass to be determined.
- The TRD detects the transition radiation emitted by electrons, allowing electrons to be identified.

The different sub-detectors can provide identification information over different momentum ranges. The information from all the sub-detectors is combined using Bayesian statistical methods, described in appendix A, to obtain a set of weights for each track, roughly corresponding to the probability of the track being of a particular particle species.

5.8 Fast simulation

The full simulation and reconstruction of an ALICE event involves the following:

1. Generation of the particles resulting from the collision, using a Monte Carlo generator such as PYTHIA or HIJING.

2. Tracking of the resulting particles through the detector, simulating decays, interactions and detector response, using the GEANT software.

3. Processing of the resulting simulated detector response to reconstruct tracks etc. for analysis. This step will also be performed on the real data.

Stages 2 and 3 are by far the most time consuming, taking several CPU-hours each per HIJING central Pb-Pb event, with stage 1 taking approximately one minute. Using the results obtained in the previous sections as a guide, a fast simulation routine was developed which replaced stages 2 and 3 with a suitable parameterisation of the detector response. This used values for particle reconstruction efficiency and momentum resolution obtained from the detailed simulation. This procedure was several orders of magnitude faster than the full simulation, and allowed a large sample of events to be simulated in a reasonable time. Without such a method, it would not have been possible to generate a large enough sample of events to study the ρ^0.

To make the fast simulation practical, several simplifying assumptions were made, which will inevitably introduce some systematic errors. The results obtained in the previous sections give confidence that these errors will be small compared to the reduction in statistical error which a fast simulation method achieves. It is also expected that they are small compared to the uncertainties in the physics predictions of the Monte Carlo generators. The assumptions are:

- Reconstruction efficiency as a function of pseudorapidity can be modelled as a top-hat function, using a constant efficiency within a range of η values and zero efficiency outside this range. This was shown to be a good approximation in section 5.5.1, figures 5.7 and 5.8, and is valid for both pp and Pb-Pb events.

- Reconstruction efficiency as a function of p_x and p_y can be described as a function of p_t only. Efficiency was shown to have a strong dependence on p_t in section 5.5.2. There is no reason from the physics or from the properties of the detector to introduce a ϕ angle dependence, so the specific values of p_x and p_y are not expected to affect the result.

- Efficiency does not depend on multiplicity for p-p collisions, but is expected to be different for Pb-Pb collisions of varying multiplicity. The fraction of occupied TPC cells, ITS pixels, etc. is much larger for Pb-Pb collisions than for pp collisions. This is expected to lead to different reconstruction efficiencies for pp events and for Pb-Pb events of varying multiplicity.

- Errors in momentum measurement are a function of p_t only. The errors themselves are treated separately for p_x, p_y and p_z.

- Electron and muon tracks are not included. Almost all these tracks are secondary, and, as shown in section 5.4.2, impact parameter based cuts can easily reduce the number of these tracks to a negligible level.

- Secondary tracks, such as those from weak decays, are not included. Loose cuts based on impact parameter reduce the contribution by such tracks to under 5%, as shown in section 5.4.1. This level of contamination will not significantly affect the results.

- Particle identification efficiency is a function of p_t and particle type only.

The values used for the parameterisation were obtained from the detailed simulation. For the pp case, a sample of 100,000 PYTHIA events was used. For Pb-Pb, a sample of 4,000 central HIJING events was used.

5.8.1 Acceptance and efficiency

As shown in figures 5.7 and 5.8, the track reconstruction efficiency is flat in η in the range $-0.9 < \eta < 0.9$, and zero outside this range. It is also a strong function of p_t, and depends on the particle species. The fast simulation routine, therefore, rejects all tracks with a pseudorapidity outside the range $-0.9 < \eta < 0.9$, and uses a parameterisation of efficiency as a function of p_t and particle species.

To obtain this parameterisation, the tracks from a sample of detailed simulation events were put into p_t bins from 0 to 10 GeV/c, with variable bin sizes to account for the lower statistics and slower variations of efficiency at high p_t. A different parameterisation was used for pions than for kaons and protons as the reconstruction efficiency is substantially different, particularly in the low-p_t region.

The reconstruction efficiency for each p_t bin was calculated by dividing the number of reconstructed tracks in the bin by the number of generated tracks in the bin, and a histogram was made of the resulting values. Polynomial functions were fitted to these histogram, using different functions in different regions to account for rapid changes in the efficiency as a function of p_t.

5.8.2 Momentum errors

As shown in section 5.6.2, the effect of track momentum resolution on the properties of the ρ^0 is small. Its contribution to the error in the ρ^0 p_t is of the order of 10 MeV/c, and its contribution to the error in the ρ^0 mass is of the order of 10 MeV/c^2. The errors in ρ^0 p_t and mass must be acknowledged, but the error in p_t is small compared to the typical ρ^0 p_t, and the error in mass is small compared to the ρ^0s natural width. Therefore, an approximate method of modelling these errors is appropriate in the fast simulation, and this will not affect the conclusions drawn from the ρ^0 analysis described later.

The error modelling was again based on a sample of detailed simulation events, with pp and Pb-Pb treated separately. A list of tracks of the appropriate particle species was obtained from each sample of events. For each of these tracks, the difference between the generated and reconstructed values of p_x, p_y and p_z was calculated. These tracks, together with the calculated "errors", were then placed into p_t bins. Variable bin sizes were used to ensure both a large number of particles per bin and to correctly account for large variations of resolution with p_t.

This table is then used when the fast simulation is applied to generated tracks. For each generated track which is put through the fast simulation, a particle is chosen at random from the appropriate p_t bin. The errors in p_x, p_y and p_z from this randomly chosen track are added to the momentum components of the generated track. This simulates the errors which would be introduced in the real momentum measurement.

5.8.3 Particle Identification modelling

In the fast simulation, the detector response information is not available and so the standard particle identification technique, described in section 5.7, cannot be used. Fortunately, for the study of the $\rho^0 \to \pi^+\pi^-$ channel, precise modelling of the PID is not required. Most of the tracks present in the events are pions, and PID is used to remove contamination from decays such as $K^{0*} \to K\pi$.

To model the PID in the fast simulation, a sample of tracks from the detailed simulation was used. To effectively suppress the contamination from kaons, a strict selection criterion was used. The standard ALICE detailed simulation PID information consists of a set of weights corresponding to the possibilities - electron, muon, pion, kaon or proton. These weights are roughly proportional to the probability of the track being of the relevant particle species, disregarding the relative abundances. These weights were normalised so that the total was one. As the masses of the pion

and muon are so similar, the central tracking detectors are unable to effectively distinguish them, so these two weights were added together. The selection criteria then used was that the combined muon + pion normalised weight must be greater than 0.9.

If this criterion is applied to the sample of tracks from the detailed simulation, the fraction of pions which are correctly identified as pions can be calculated as a function of transverse momentum, as can the fraction of electrons, muons, kaons and protons which incorrectly identify as pions. A table was constructed, based on this information, which allowed the probability of identification as a pion to be obtained as a function of particle species and transverse momentum. When the fast simulation processes a generated particle, it uses this table to label the particle as either as a pion or not a pion, simulating the identification performed by the full reconstruction routine. For example, if the probability in the table is P, the fast simulation chooses a random number from a uniform distribution between 0 and 1. If this number is less than P, the particle is labelled as a pion, otherwise it is labelled as "not pion". This method should account for both the loss in pion detection efficiency due to misidentification of pions and contamination of the pion sample from misidentified kaons and protons.

5.8.4 Fast simulation performance

The full simulation and reconstruction of a central Pb-Pb event takes several hours using a typical single processor, in this case a 2 GHz Xeon. The fast equivalent, due to the much simpler methods used, takes about 1 second. This is negligible compared to the time required for the Monte Carlo generator HIJING and for the resonance reconstruction and invariant mass calculation routine. Typically, the generation, fast simulation and invariant mass calculations take approximately 2 minutes per event in total. Therefore the overall time for 1 million central events is about 1400 CPU-days. This can be carried out in a reasonable time using computing farms,

whereas using the full simulation would need over 1,000 CPU-years to do the same thing. The greatly increased speed allows a sample of 10^6 central Pb-Pb events and 5×10^7 pp events to be generated for the ρ^0 analysis.

Chapter 6

Analysis of the ρ^0 resonance at ALICE

6.1 Introduction

The prospects for measurements of the ρ^0 resonance in proton-proton and lead-lead collisions at ALICE were investigated using Monte Carlo simulations. Simulations of Pb-Pb collisions are more difficult than p-p collisions, as the much larger event multiplicity requires correspondingly larger CPU time to simulate. The fast simulation method described in section 5.8 was used to generate a large number of pp and Pb-Pb events. After event simulation, the ρ^0 signal was reconstructed by calculating the invariant masses of track pairs. Background subtraction techniques were developed to subtract the very large combinatorial background. Finally, an appropriate function was used to fit the data in order to extract values of ρ^0 mass, width and yield.

6.2 Analysis of the ρ^0 in Pb-Pb collisions

6.2.1 Event generation

The HIJING event generator, described in section 5.2.2, was used to simulate 10^6 central Pb-Pb events. Only collisions with impact parameters of 0-3 fm were considered "central" and included in this sample. The HIJING generator predicts an average multiplicity of about 6000 charged primary tracks per unit of pseudorapidity in the central rapidity region for a central Pb-Pb collision. This is somewhat higher than the predictions of some other models, which typically estimate a $dN_{ch}/d\eta$ of about 2000-3000 in the central region [94, 95]. However, all models are estimates only, and it is reasonable to be conservative when investigating the performance of a future experiment.

To check whether the HIJING predictions are reasonable, the ρ/π ratio can be compared with results from previous experiments. The ρ/π ratio has been measured for a number of different centre-of-mass energies and for different collision systems, including pp at 6.8 GeV [96], 19.7 GeV [97], 27.5 GeV [98] and 52.5 GeV [99], e^+e^- at 10.45 GeV [100] and 91 GeV [101], π^-p at 19.6 GeV [102], K^+p at 7.82 GeV [103] and peripheral Au-Au at 200 GeV [46].

Figure 6.1 shows the ρ/π ratio measurements from previous experiments, with HIJING's prediction for Pb-Pb at ALICE included. The ρ refers to ρ^0 only and the π refers to a single species of pion (π^-, π^0 or π^+). The results from previous experiments suggest that the ratio is either independent of collision energy or increases slowly with collision energy. A decrease in ρ/π ratio is not supported by the data. The HIJING prediction of ρ/π ratio is similar to the results from lower energies, with a predicted ratio of 0.150 for central Pb-Pb, and 0.165 for peripheral Pb-Pb (not shown). Therefore, as the ρ^0 signal is more easily observable with higher ρ/π ratio, the HIJING prediction is reasonably conservative.

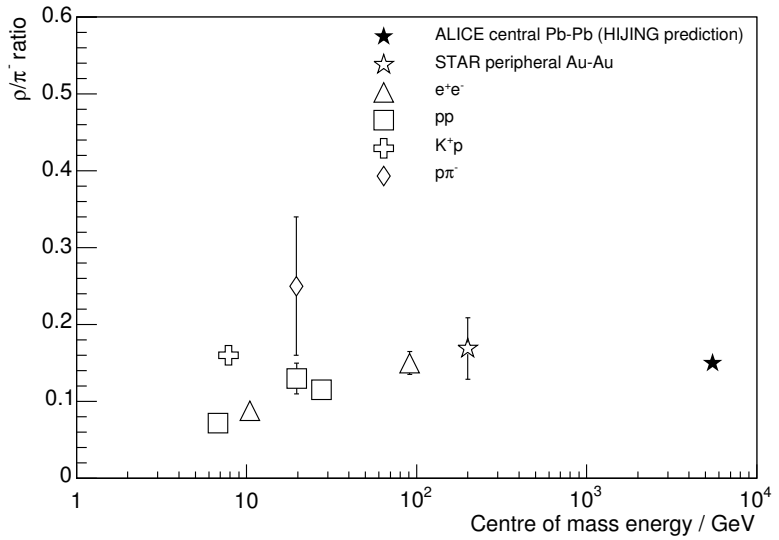

Figure 6.1: Ratio of ρ to π for various collision systems and energies, including HIJING's prediction for Pb–Pb at ALICE. The other systems are e^+e^- at 10.45 GeV and 91 GeV, pp at 6.8 GeV, 19.7 GeV, 27.5 GeV and 52.5 GeV, K^+p at 7.82 GeV, π^-p at 19.6 GeV and peripheral Au-Au at 200 GeV.

The generator output was passed to the fast simulation routine, described in section 5.8. The fast simulator attempts to reproduce the output of the full simulation and reconstruction process, resulting in a simulation of what will be seen when the reconstruction algorithms are applied to the real data. Some selection cuts are applied at this stage to eliminate tracks which are unlikely to be from a primary ρ^0 decay, and these are described below.

6.2.2 Selection of tracks

As shown in section 5.4.1, most secondary tracks can be removed by applying selection criteria based on their impact parameter. The remaining secondaries are a small fraction of the tracks, and so the fast simulation ignores them. However, PID requirements cannot be ignored. Not only do non-pion tracks add to the continuum background, but there will be contamination from other resonances, of which the

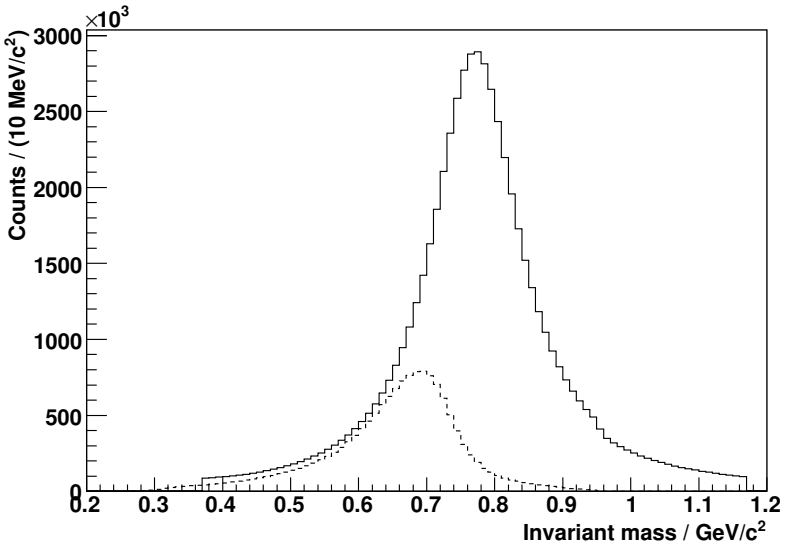

Figure 6.2: Plot of ρ^0 invariant mass signal (solid line) and K^{0*} invariant mass signal (broken line) for 10^6 central HIJING Pb-Pb events using a $\pi^+\pi^-$ hypothesis.

$K^{0*}(892)$ and its antiparticle are the most important. Each event will contain decays of the $K^{0*}(892)$ and $\overline{K}^{0*}$, resulting in additional correlated contributions to the $\pi^+\pi^-$ invariant mass spectrum. These particles decay via the following channels:

$$K^{0*} \rightarrow K^+\pi^- \tag{6.1}$$

$$\overline{K}^{0*} \rightarrow K^-\pi^+ \tag{6.2}$$

The term K^{0*} is used subsequently to refer to both of these decays. Under a $\pi^+\pi^-$ decay hypothesis, the invariant masses of the $K\pi$ pairs from the K^{0*} decays form a large peak in the ρ mass region of the invariant mass spectrum, which complicates the fitting of the ρ^0 signal. To eliminate this, pion identification was required. This used the PID model included in the fast simulation, described in section 5.8.3. The relative sizes of the ρ and K^{0*} contributions are shown in figure 6.2. Without particle identification, the number of K^{0*}s is 24% of the number of ρ^0s, which represents a significant contamination. After applying the PID selection criterion, this was reduced to 0.25%. This remaining K^{0*} contamination is small and can be ignored.

6.2.3 ρ reconstruction and background subtraction

Reconstruction of the ρ^0 signal was carried out by calculating the invariant mass of all possible $\pi^+\pi^-$ pairs which satisfy the selection criteria described in section 6.2.2. The resulting histogram is shown in figure 6.3. The ρ^0 signal with all background removed is shown for comparison in figure 6.4. It can be seen that the ρ^0 signal is very small compared to the background, as the background peak in the ρ^0 mass region is several thousand times larger than the peak of the ρ^0.

Due to the large number of tracks in each central Pb-Pb event, even after selection cuts, the combinatorial background was very large compared to the ρ^0 signal. Therefore, it was necessary to develop a method for estimating the background and then subtracting it.

6.2.4 Like-sign background subtraction

One method of estimating the background is the *like-sign* method. Assuming that there are equal numbers of positive and negative tracks, and that the momentum distributions of positive and negative tracks are the same, the combinatorial background for $\pi^+\pi^-$, $\pi^+\pi^+$ and $\pi^-\pi^-$ will be the same, within statistical errors. However, the $\pi^+\pi^+$ and $\pi^-\pi^-$ (like-sign) cases will not include the cases of both tracks coming from the same resonance, as there are no resonances of interest which decay to two pions of the same sign. Therefore, subtracting the $\pi^-\pi^-$ or $\pi^+\pi^+$ spectrum from the $\pi^+\pi^-$ spectrum should remove the combinatorial background but not the resonance contributions.

The combined like-sign spectrum was calculated by taking the geometric mean of the two separate like-sign spectra. For each bin, the total number of entries for the positive track combinations was multiplied by the total number of entries for the negative track combinations, and the square root of this product was then taken.

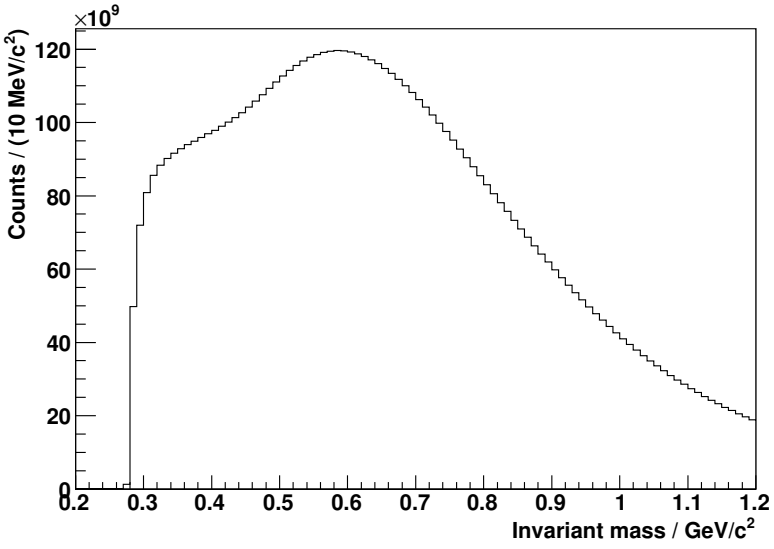

Figure 6.3: Unsubtracted $\pi^+\pi^-$ invariant mass spectrum for 10^6 central Pb-Pb events.

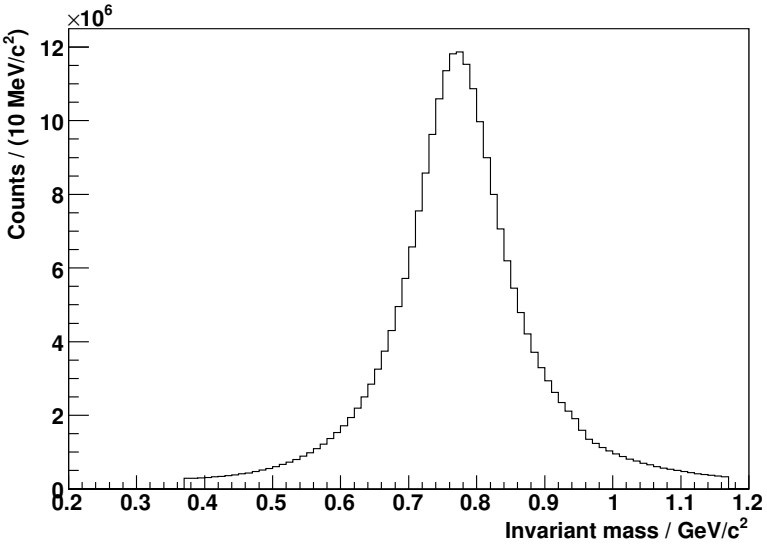

Figure 6.4: Background-free ρ^0 invariant mass spectrum for 10^6 central Pb-Pb events.

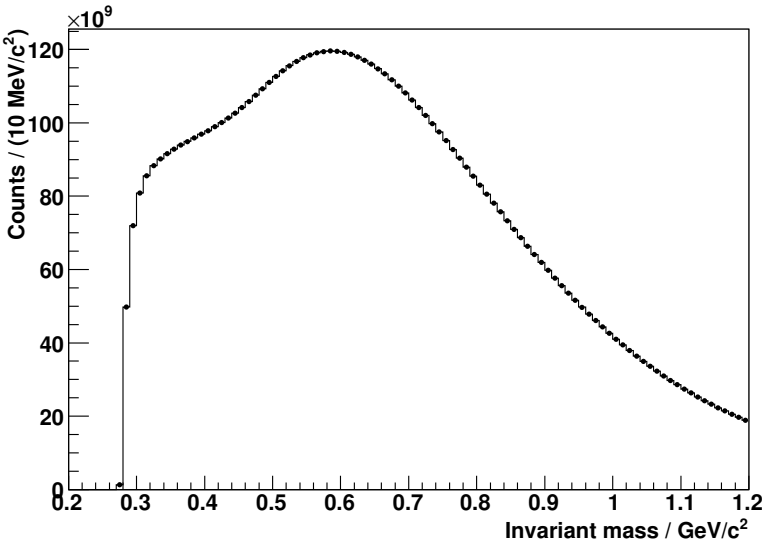

Figure 6.5: Comparison of unlike-sign (solid line) and like-sign (circular points) histograms for 10^6 central HIJING Pb-Pb events.

Using the geometric mean helps to correct for any asymmetry in the number of positive and negative tracks, and produce a background closer to the unlike-sign spectrum.

The like-sign and unlike-sign spectra are shown in figure 6.5, with the signal histogram shown by the line and the like-sign spectrum shown by the circles. No normalisation was applied to the like-sign spectrum as it reproduced the combinatorial background very closely. It was not possible to improve the result by multiplying the like-sign spectrum by a fixed factor.

The results of the like-sign subtraction for the 10^6 Pb-Pb central events are shown in figure 6.6. The points with circles show the difference between the two graphs shown in figure 6.5, and represent the background-subtracted invariant mass spectrum. The error bars are relatively large despite the very large number of ρ^0s. This is due to statistical fluctuations in the background estimate, which are given by $\sqrt{N_{background}}$, and not by fluctuations in the number of ρs, which are given by $\sqrt{N_{\rho^0}}$. As $N_{background} >> N_{\rho^0}$, the error bars are large.

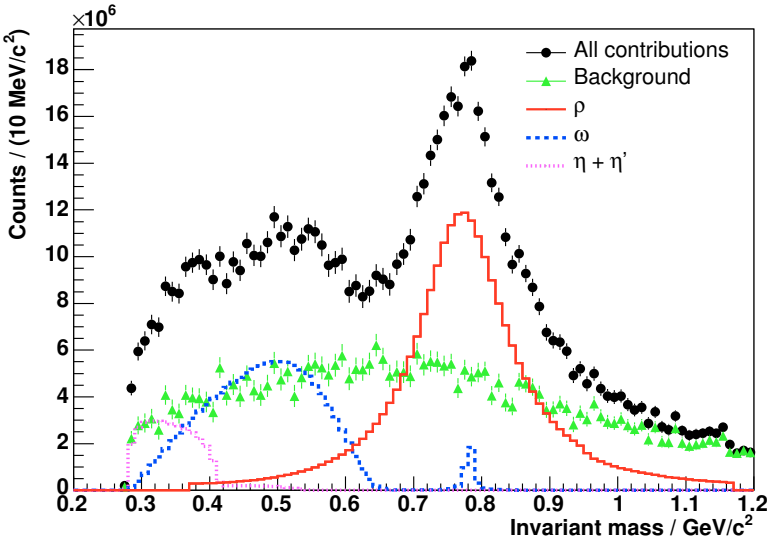

Figure 6.6: $\pi^+\pi^-$ spectrum for 10^6 central events after like-sign background subtraction, showing individual contributions.

As these data come from a Monte Carlo simulation, the actual source of a contribution to the invariant mass spectrum is recorded and can be extracted. This information, known as Monte Carlo "truth" information, will not be available in the real data, but is used here to show the contributions to the spectrum. The solid line shows the contribution from $\pi^+\pi^-$ pairs where both tracks originate from the same ρ^0 decay. Similarly, the dotted lines show the contribution from $\pi^+\pi^-$ pairs where both tracks originate from the same ω, η or η' decay. The large, wide shapes for ω, η and η' are due to the reconstruction of the invariant mass from two of the three decay products of these particles. The contributions from η and η' decays are added together and shown as a single line. The triangular points show the results from the like-sign background subtraction after the above resonance contributions are removed, giving an indication of the "residual background"', i.e. the difference between the true background and the like-sign estimate.

6.2.5 Mixed event background subtraction

Another method of estimating the background uses combinations of positive and negative tracks from different events. This method has the advantage that it naturally takes into account the asymmetry between positive and negative tracks. Also, as each event can be combined with many other events, the statistics are superior to those of the like-sign method. However, this method has the significant disadvantage that different events can have considerably different characteristics, such as multiplicity, mean p_t, anisotropic flow etc. Care must be taken to ensure that only similar events are mixed.

Preliminary investigations showed that the mixed-event method was considerably inferior to the like-sign method at reproducing the background shape. Whereas the like-sign method very closely reproduced the combinatorial background immediately and with no tuning, the mixed-event method introduced large distortions into the subtracted spectrum which would have made fitting impossible. This remained the case even when restrictions on multiplicity and mean p_t were applied to the mixed events. As a result of this, and also due to the success of the like-sign method, the mixed event method was not used in the final analysis.

6.2.6 Fitting method

To extract values for the ρ^0 mass, width and yield, it is necessary to fit an appropriate function to the background-subtracted invariant mass histogram, shown by the points labelled with circles in figure 6.6. As the ρ^0 signal cannot be isolated, it is necessary to fit a function describing not only the ρ^0 but the other contributions to the histogram. These contributions are:

- The ρ mass peak, labelled "ρ" in figure 6.6.

- The residual combinatorial background, caused by the like-sign distribution not exactly reproducing the background, labelled "background".
- The $\omega \to \pi^+\pi^-\pi^0$ decay, with the invariant mass calculated from the π^+ and π^- decay tracks only, labelled "ω".
- The $\omega \to \pi^+\pi^-$ decay, which forms a small peak at 0.782 GeV/c^2, labelled "ω".
- The $\eta \to \pi^+\pi^-\pi^0$ and $\eta^{'} \to \pi^+\pi^-\eta$ decays, with the invariant mass calculated from the π^+ and π^- decay tracks only, labelled "$\eta + \eta^{'}$".

As the mass and width of the ρ are to be measured, the fit should be carried out over as large a mass range as possible to include most of the ρ shape. However, to make the fit more reliable, as few free parameters should be included as possible. The fit was therefore carried out over the mass range $0.55 < m_{\pi\pi} < 1.2$ GeV/c^2, which excluded background from the η and η'. This reduced the number of free parameters needed in the fit, while retaining a large fraction of the ρ^0 signal. In this region, the residual combinatorial background could be modelled by a straight line, using two free parameters. The ρ was modelled by a non-relativistic Breit-Wigner, shown in equation 6.3, with mass, width and size as free parameters.

$$\frac{dN}{dm} = A \times \frac{\Gamma}{(m-\mu)^2 + \frac{\Gamma^2}{4}} \tag{6.3}$$

The non-relativistic form was used as this was the function used by the Monte Carlo generators, as an accurate model of the ρ^0 shape is difficult [91]. To model the ρ^0 realistically in the real data, a relativistic Breit-Wigner should be used, and it may be necessary to take phase space effects into account. There are also other factors which may could affect the shape of the ρ^0 compared to its value in elementary collisions. These include signal-background interference, Bose-Einstein correlations between pions from the ρ^0 decay and identical pions close in phase-space, and any effects due to the QGP.

The ω shape was determined from the Monte Carlo simulation, and the size is left as the only free parameter. As an additional constraint, the fitted function was normalised to the same area as the histogram in the mass range given above. This reduced the number of free parameters by one, and resulted in a more stable fit and reduced errors. The resulting fit had five free parameters. For the fits with fewer free parameters, e.g. where the ρ^0 width was fixed or where the fit was done to the ρ^0 without background, this normalisation constraint was not applied.

The fits were performed by the MINUIT software [104]. When using MINUIT, the fit parameters are set to reasonable initial values, and then the routine makes adjustments to the parameters in order to minimise the χ^2. The set of parameters with the lowest χ^2 is taken as the best fit. The errors are calculated using the MINOS routine in the MINUIT package [104]. To calculate the error in a fit parameter i, MINOS starts with the values of the fit parameters which minimize the χ^2, and adjusts i until the point is found at which the increase in χ^2 corresponds to the 1σ error. In general, this method produces asymmetric errors.

6.2.7 Fit results

Figure 6.7 shows the result of a fit of the function described above to the $\pi^+\pi^-$ invariant mass spectrum in HIJING Pb-Pb collisions. The fitted ρ mass is 0.771 ± 0.001 GeV/c^2, with a width of 0.162 ± 0.008 GeV/c^2 and a yield of $2.30^{+0.69}_{-0.47} \times 10^8$ ρ^0s. These can be compared to the generated mass of 0.7685 GeV/c^2, width of 0.151 GeV/c^2 and yield of 1.97×10^8 ρ^0s. These results show that the mass of the ρ was measured reliably to good precision, although the quoted error is an underestimate as it includes the statistical error only. Any significant mass shifts should be measurable. The number of ρs was also measurable, with an estimated statistical error of 20 to 30%. The width measurement was also reasonable.

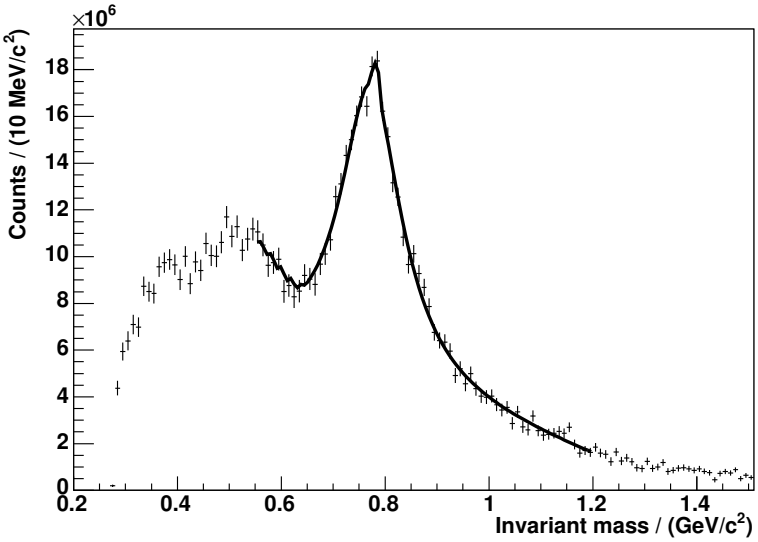

Figure 6.7: Fit to background-subtracted $\pi^+\pi^-$ spectrum.

6.2.8 Systematic errors in fitting

A distortion of the ρ^0 line shape was observed in the reconstructed signal when compared to the generated signal, as shown in figure 6.8. This indicates that the detector introduces a significant distortion of the ρ^0 shape, as the plot would show a flat line for a distortion-free detector. This was not initially expected, and is most likely due to variation of reconstruction and identification efficiency with track momentum. The ρ^0 has a large width, so the momentum of the decay tracks will tend to be larger for larger mass ρ^0s. The differences are not small compared to the momentum of most ρ^0s. For example, the momentum difference between a π from a 1070 MeV/c^2 ρ^0 and one from a 470 MeV/c^2 ρ^0 is 327 MeV/c, whereas the mean transverse momentum of ρ^0s in this sample was around 750 MeV/c, with 80% of ρ^0s having a p_t of below 1 GeV/c. The reconstruction efficiency is known to vary significantly over this momentum range, as shown in section 5.5.2, and particle identification efficiency is also highly momentum dependant. This could lead to the observed distortion of the ρ^0 shape.

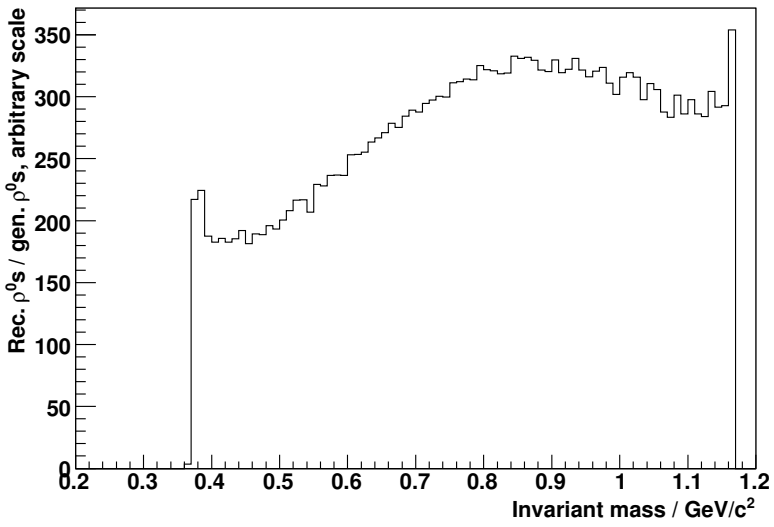

Figure 6.8: Number of reconstructed ρ^0s divided by number of generated ρ^0s. It can be seen that the detected ρ^0 shape is different from the generated shape, as the plot is not flat across the ρ^0 mass range. No normalisation is applied to the samples so the Y-axis units are arbitrary.

Comparison of fits to generated and reconstructed ρ^0s

To determine the effect of the line shape distortion described above on the ρ^0 measurement, fits were carried out on both the reconstructed ρ^0 spectrum and the generated ρ^0 spectrum. In both cases, the background was removed using the Monte Carlo truth information.

Figure 6.9 shows the background-free reconstructed ρ^0 spectrum and the fit that was made to it, and figure 6.10 shows the background-free generated ρ^0 spectrum and the fit that was made to it. The fitted masses and widths are shown in table 6.1. As the "generated" histogram was produced from a separate, smaller sample, the fit errors are larger than those for the fit to the reconstructed spectrum. However, the generator used was the same for both samples, and so there was no systematic difference.

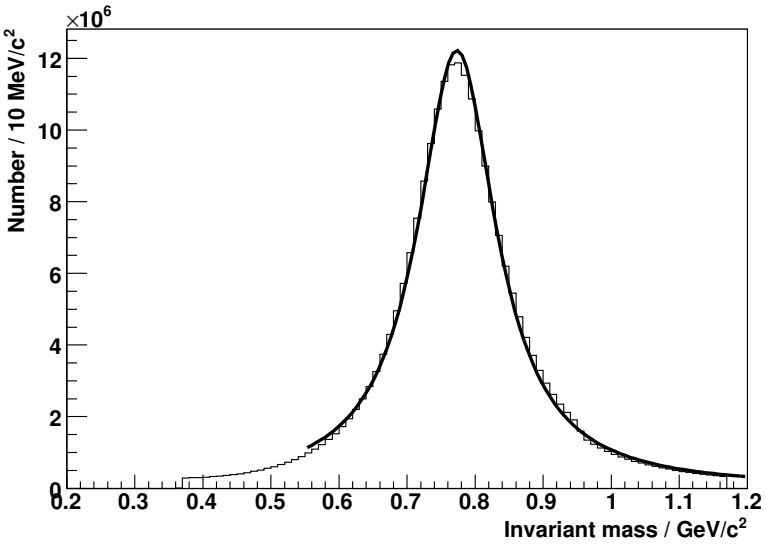

Figure 6.9: Fit to reconstructed ρ^0 signal, with background removed using the MC truth information.

Table 6.1: Fitted values of ρ^0 mass and width for generated and reconstructed ρ^0s in the absence of background, and a comparison to the generator input values.

	Generated value	Fit to generated	Fit to reconstructed
Mass / GeV/c^2	0.7685	0.76736 ± 0.00016	0.77325 ± 0.00001
Width / GeV/c^2	0.151	0.14813 ± 0.00037	0.14085 ± 0.00002

It can be seen that distortion affects the fit of the ρ. Both the fitted mass and width are subject to a shift from the true value. This error is in addition to the quoted MINOS errors. Additionally, the fitted reconstructed width is smaller than both the generated width and the fitted reconstructed width when background is present.

Whereas naively it may be thought that detector efficiency correction is only relevant for yield measurements, this result shows that efficiency effects must also be taken into account when measuring the mass and width of the ρ^0. In this case, the measured mass is reasonable although the quoted error is too small. The measured

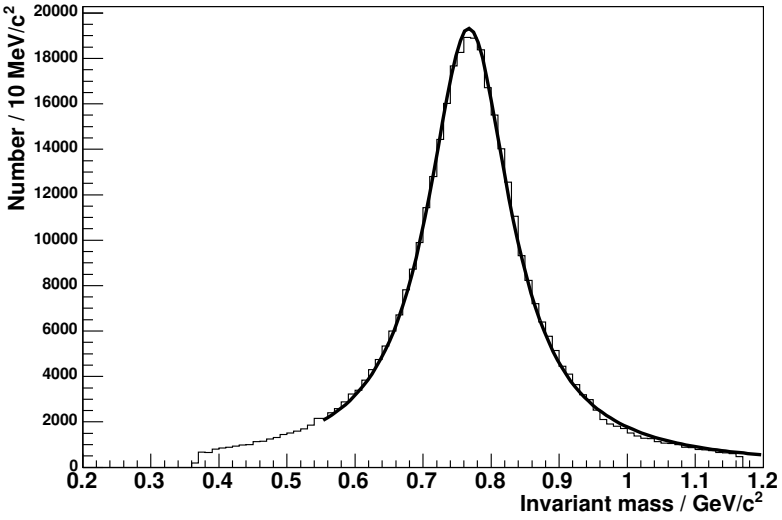

Figure 6.10: Fit to generated ρ^0 signal, with background removed using the MC truth information.

width, however, is much further away from the generated value and the quoted statistical error is far too small, but the width is still correct to within 6%. However, it should not be assumed that the results will be this favourable in general. Ideally, the invariant mass spectrum should be corrected for acceptance and efficiency before fitting is carried out, in order to correct for any detector induced line shape distortions.

6.2.9 Signal-to-background ratio and significance

The signal-to-background ratio is simply the number of ρ^0s in a defined mass region divided by the number of background $\pi^+\pi^-$ pairs in the same mass region. This is not a very useful measure for a Pb-Pb event, for two reasons:

- The S/B is very low for a Pb-Pb event, as the number of background pairs scales as N^2_{tracks}.
- Most of the background can be subtracted.

The signal significance, defined in section 5.1, is a more useful measure.

$$\text{Significance} = \frac{\text{S}}{\sqrt{\text{S} + \text{B}}} \tag{6.4}$$

Table 6.2 shows the number of signal ρ^0 histogram entries, number of background entries, S/B and significance for the 10^6 simulated Pb-Pb events, separated into different p_t ranges. The significances for a sample of 10^7 events, which is of the order of the number of events expected in one year of data taking, are larger by a factor of $\sqrt{10}$. All quoted numbers of histogram entries are in the mass range 630 MeV/c^2 to 930 MeV/c^2.

Table 6.2: Significance and S/B values for ρ^0 in various p_t regions for 10^6 HIJING central Pb–Pb events.

p_t range	PID	Signal	Background	S/B	Significance
All	Yes	1.97×10^8	2.65×10^{12}	7.43×10^{-5}	121
	No	2.66×10^8	4.11×10^{12}	6.0×10^{-5}	127
Below 1 GeV/c	Yes	1.78×10^8	2.40×10^{12}	7.42×10^{-5}	115
	No	2.27×10^8	3.74×10^{12}	6.0×10^{-5}	117
1-2 GeV/c	Yes	1.71×10^7	2.42×10^{11}	7.06×10^{-5}	34.8
	No	3.35×10^7	6.89×10^{11}	4.86×10^{-5}	40.4
2-4 GeV/c	Yes	2.15×10^6	9.30×10^9	2.31×10^{-4}	22.3
	No	5.05×10^6	3.50×10^{10}	1.44×10^{-4}	27.0
Above 4 GeV/c	Yes	2.16×10^5	2.14×10^8	1.0×10^{-3}	14.8
	No	8.20×10^5	1.27×10^9	6.45×10^{-4}	23.0

The lower signal significance in p_t sub-regions complicates the analysis. Additionally, as p_t increases to over 4 GeV/c, the PID becomes much less efficient and the signal significance is greatly decreased from the ideal case. Therefore, at high p_t, the PID described above cannot be used. It may be possible to study the high p_t region by not using PID at all or by using alternative PID criteria. Table 6.3 shows

the signal significance for 10^7 events for p_t between 4 GeV/c and 10 GeV/c with no PID selection cuts. However, if PID is not used, the $K^{0*} \rightarrow K\pi$ contamination must be removed in some other way, for example if the yield and shape are known from a dedicated K^{0*} analysis. Additionally, the lower statistics at very high p_t will prevent yield measurements even if the K^{0*} contamination can be eliminated.

Table 6.3: Significance and S/B values for ρ^0 at high p_t based on a sample of 93,000 HIJING central Pb–Pb events. Significance is shown for 10^7 events.

p_t range	PID	Signal	Background	S/B	Significance (10^7 evts.)
4-6 GeV/c	No	63958	1.17×10^8	5.47×10^{-4}	61.3
6-8 GeV/c	No	14383	1.28×10^7	1.12×10^{-3}	41.7
8-10 GeV/c	No	3898	2.01×10^6	1.94×10^{-3}	28.4

6.2.10 Effect of reduced signal

The results described above were based on the HIJING predictions. As the real data may differ significantly from these, it is useful to know how the analysis will be affected if the number of ρ^0s is smaller than expected. To investigate this, the fits were performed on the same data set as above but with a certain fraction of the ρ^0s removed. For these fits, the width parameter was fixed at 140 MeV/c^2 to improve the fit stability when the signal was reduced. The results are shown in table 6.4.

The results show that it is still possible to obtain a fit with a ρ^0 signal reduced by a factor of four from that in the main analysis, but the error in the measured yield increases to about 25%. However, the quoted statistical error is unreasonably low, indicating that systematic effects become dominant for low ρ^0 yields. This effect is even more noticeable in the case of a ρ^0 yield which is 10% of the HIJING prediction, where the fitted yield is 67% larger than the true value but the quoted error is much smaller than this. It is apparent that a reasonable value of significance is required

Table 6.4: Fitted mass and yield for cases with a number of ρ^0 equal to 50%, 25% and 10% of the HIJING prediction for 10^6 central Pb-Pb events. The width is fixed at 140 MeV/c^2 for these fits.

ρ^0 fraction	Fitted mass (GeV/c^2)	Fitted N_{ρ^0}	Correct N_{ρ^0}
50%	0.771 ± 0.002	$10.8 \pm 0.8 \times 10^7$	9.85×10^7
25%	0.769 ± 0.004	$6.13^{+0.65}_{-0.57} \times 10^7$	4.92×10^7
10%	0.765 ± 0.007	$1.03 \pm 0.16 \times 10^6$	1.97×10^7

for a good measurement of the ρ^0 yields and properties. The results show that a reasonable measurement of mass and yield of the ρ^0, assuming the width can be fixed for the fitting, can be made for a significance of 30, as this is the significance for the 25% ρ^0 fraction shown in table 6.4.

6.2.11 Error analysis

The error analysis is more difficult for the ρ^0 measurement than for the Ξ measurement at NA57. The Ξ signal suffered from low statistics, but was otherwise clean. The ρ^0 signal had good statistics but had significant background contributions which were non-random in nature, such as the ω, the residual background and the distortion of the ρ^0 shape. Imprecise modelling of these factors leads to systematic errors which are difficult to assess.

Statistical errors

The MINOS routine [104], described in section 6.2.6, was used to estimate the statistical error on the fitted values of ρ^0 mass, width and yield. However, as shown in table 6.4, this is not a reliable indication of the total error, especially as the ρ^0 signal becomes smaller compared to the other $\pi^+\pi^-$ contributions.

Systematic errors

Several systematic effects contribute to the error in the measurement of ρ^0 properties.

- A systematic error was introduced by detector-induced modification of the ρ^0 line shape, described in detail in section 6.2.8.
- The residual combinatorial background was modelled by a straight line over an extended region. This is only an approximation, and any deviations from this behaviour appear as an effective distortion of the ρ^0 shape and size. This error becomes more significant if the ρ^0 yields are smaller than expected.

Therefore, when analyzing the real data, thorough Monte Carlo studies will be necessary to ensure that such systematic effects are well understood.

6.2.12 Conclusions

The Monte Carlo study described above suggests that it will be possible to measure the ρ^0 signal in central Pb-Pb collisions at ALICE. Two important measurements are the ρ^0 mass and yield, and this study showed that:

- The central mass value can be measured to good precision, therefore significant mass shifts will be measurable. However, due to line shape distortions and difficulties associated with fitting, a careful analysis of the systematic errors will be essential.
- The yield of ρ^0s can be measured to sufficient precision to allow comparisons to, e.g. pp collisions. The statistical error as reported by MINOS for the case investigated is of the order of 25%.
- Measurement of ρ^0 width is difficult due to systematic errors such as line-shape modification. However, if these effects are corrected for and the size of the error

is understood, width measurement should also be possible to a reasonable precision. Results shown here indicated a typical width measurement error of under 10%.

The results show that it should be possible to measure ρ^0 yields and properties in p_t sub-regions. When using a sample of 10^7 events, the signal significances in the sub-regions are similar to or larger than the full-p_t significance of the sample studied here. However, systematic effects can have a large effect and must be well understood. The quoted MINOS errors are not a suitable estimate of the total error, as they reflect the statistical errors only. This is most clearly illustrated by the results shown in table 6.1 - as the error bars on the fitted data are very small, the corresponding MINOS error is very small. However, as the fitted function cannot correctly reproduce the data for any set of fit parameters, the true error is quite large.

6.3 Analysis of the ρ^0 in pp collisions

The techniques which were used to study Pb-Pb collisions were then applied to pp collisions. The changes made for the pp study were:

- Use of the PYTHIA event generator rather than HIJING.
- Generation of a larger number of events. A sample of 5×10^7 pp events was generated for this analysis.
- In the fast simulation, different values for reconstruction efficiency, identification efficiency and momentum smearing were used. As for Pb-Pb, these values were derived from the detailed simulation.

As the analysis methods were the same as for Pb-Pb, the results are stated without a detailed description of the analysis technique.

6.3.1 Event generation, fast simulation, reconstruction and background subtraction

The PYTHIA Monte Carlo generator, described in section 5.2.1, was used to generate 5×10^7 pp events at a centre of mass energy of 14 TeV. The generator output was passed to the fast simulation routine, which was mostly the same as was used for Pb-Pb events. As for Pb-Pb, secondary tracks were ignored, the PID performance of the detector was simulated for the selection of π tracks and the like-sign background subtraction method was used. The functions and tables describing reconstruction efficiency, PID efficiency and momentum smearing were different for the pp case, and were obtained from a detailed simulation of PYTHIA pp events.

An important difference for the pp case was the time required for simulation. Because the events are much simpler and have much lower multiplicity, both the generation and resonance reconstruction stages were much quicker than for Pb-Pb. This allowed a much larger number of events to be generated, which in turn allowed more detailed analysis for p_t sub-regions. Like-sign subtracted invariant mass spectra were obtained for several p_t sub-regions:

- Figure 6.11 shows the invariant mass spectrum for reconstructed resonance candidates with any p_t.
- Figure 6.12 shows the invariant mass spectrum for reconstructed resonance candidates with $p_t < 1$ GeV/c.
- Figure 6.13 shows the invariant mass spectrum for reconstructed resonance candidates with $1 < p_t < 2$ GeV/c.
- Figure 6.14 shows the invariant mass spectrum for reconstructed resonance candidates with $2 < p_t < 4$ GeV/c.

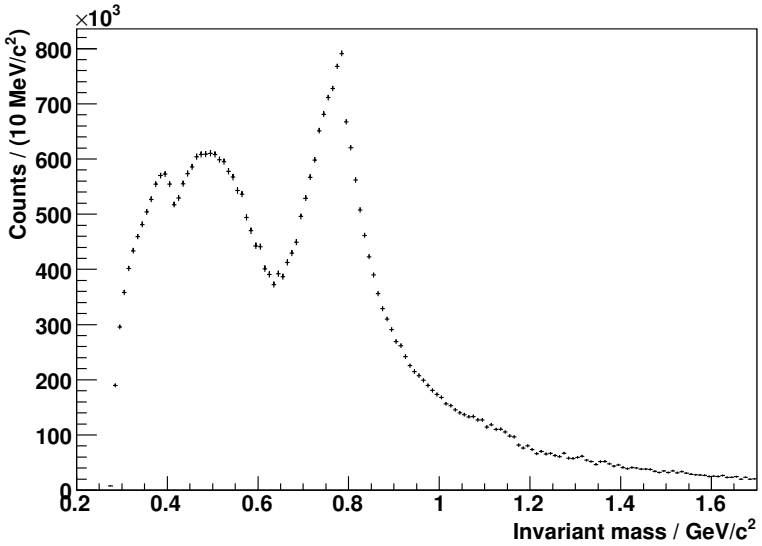

Figure 6.11: $\pi^+\pi^-$ invariant mass spectrum for 5×10^7 PYTHIA pp events after like-sign background subtraction, for resonance candidates with any p_t.

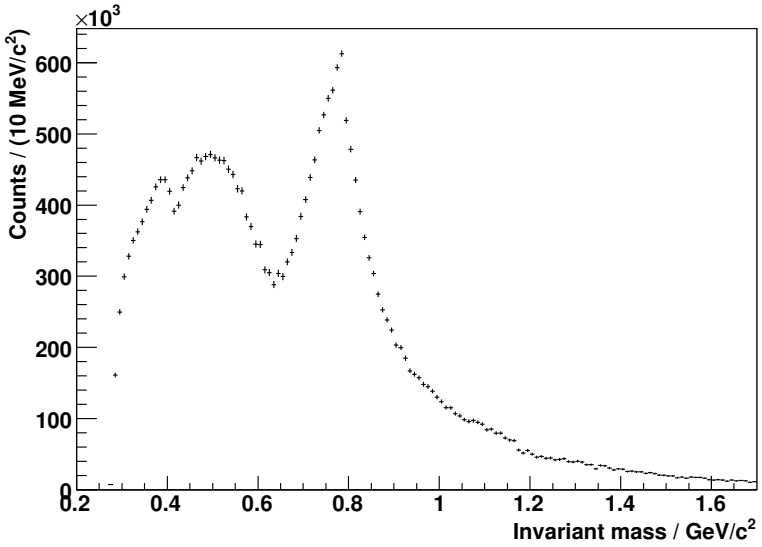

Figure 6.12: $\pi^+\pi^-$ invariant mass spectrum for 5×10^7 PYTHIA pp events after like-sign background subtraction, for resonance candidates with $p_t < 1$ GeV/c.

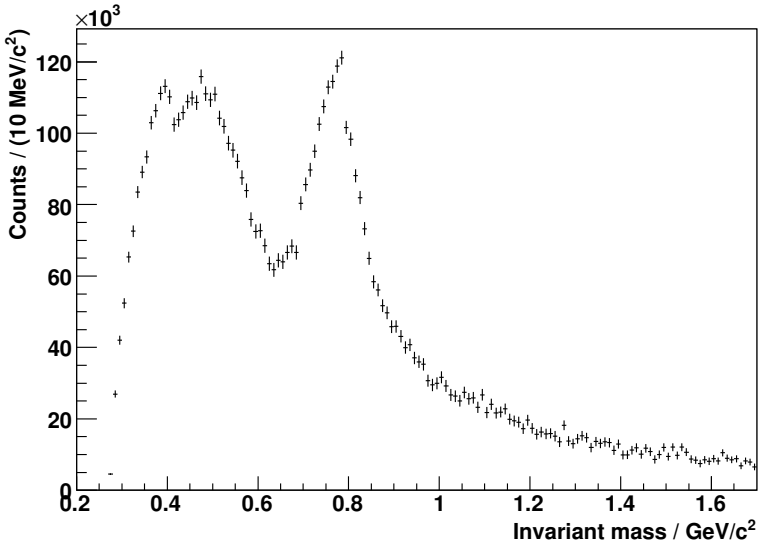

Figure 6.13: $\pi^+\pi^-$ invariant mass spectrum for 5×10^7 PYTHIA pp events after like-sign background subtraction, for resonance candidates with $1 < p_t < 2$ GeV/c.

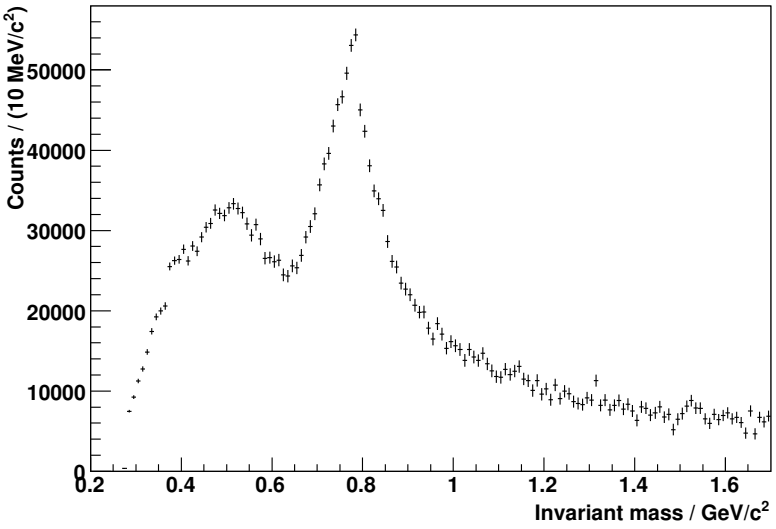

Figure 6.14: $\pi^+\pi^-$ invariant mass spectrum for 5×10^7 PYTHIA pp events after like-sign background subtraction, for resonance candidates with $2 < p_t < 4$ GeV/c.

6.3.2 Fitting

Figure 6.11 shows that the pp result is similar to the Pb-Pb result, the most notable difference being the smaller error bars due to the higher statistics. Therefore, a similar fitting method was applied to the pp case. The fitted function is shown by equation 6.5:

$$\frac{dN}{dm} = A + Bm + CW(m) + D\frac{\Gamma}{(m-\mu)^2 + \frac{\Gamma^2}{4}} \tag{6.5}$$

A and B are free parameters describing the linear background. C is a free parameter which controls the size of the ω contribution and W(m) is a fixed function describing the ω shape. The remaining free parameters describe the ρ^0 - D is its size, μ its mass and Γ is its width.

This function was used to fit each of the like-sign subtracted invariant mass spectra shown in figures 6.11-6.14. The values for the masses, widths and sizes of the ρ^0 peaks were extracted and the extracted ρ^0 functions were compared to the true ρ^0 components of the invariant mass spectra. The results of the fits are shown in figures 6.15-6.18.

Table 6.5: Fitted values of ρ^0 mass, width and yield for pp collisions at 14 TeV. The number refers to the number per 1000 events, and only ρ^0s which have masses between 630 and 930 MeV/c^2 were included.

p_t / GeV/c	Mass / GeV/c^2	Width / GeV/c^2	Number	True Number
All	$0.76739^{+0.00034}_{-0.00041}$	$0.1508^{+0.0026}_{-0.0018}$	$177.0^{+7.0}_{-4.7}$	170.4
0-1	$0.76734^{+0.00043}_{-0.00044}$	$0.1523^{+0.0027}_{-0.0024}$	$138.4^{+5.5}_{-4.9}$	131.1
1-2	$0.76548^{+0.00095}_{-0.00093}$	$0.1454^{+0.0052}_{-0.0052}$	$25.5^{+2.1}_{-2.0}$	26.14
2-4	$0.77002^{+0.00090}_{-0.00093}$	$0.1522^{+0.0061}_{-0.0057}$	$11.7^{+1.1}_{-1.0}$	11.35
4-5	$0.7740^{+0.0018}_{-0.0018}$	$0.166^{+0.013}_{-0.012}$	$1.28^{+0.24}_{-0.19}$	1.080

The ρ^0s were generated with a mass of 0.76850 GeV/c^2 and a width of 0.15100 GeV/c^2. Table 6.5 shows that the fit produces a reliable measurement of these two

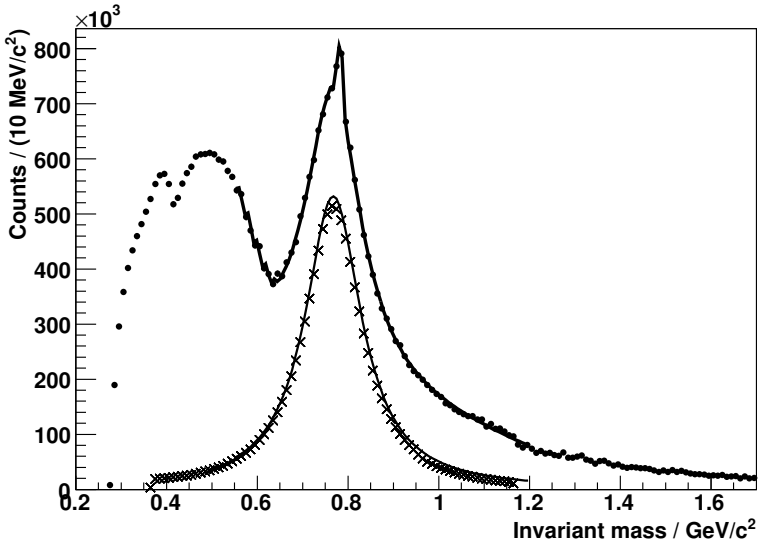

Figure 6.15: Fit of equation 6.5 to like-sign subtracted $\pi^+\pi^-$ spectrum for resonance candidates of any p_t. The solid dots show the like-sign subtracted spectrum and the crosses show the ρ^0 component. The ρ^0 component of the fit is also shown in the plot for comparison with the actual ρ^0 contribution.

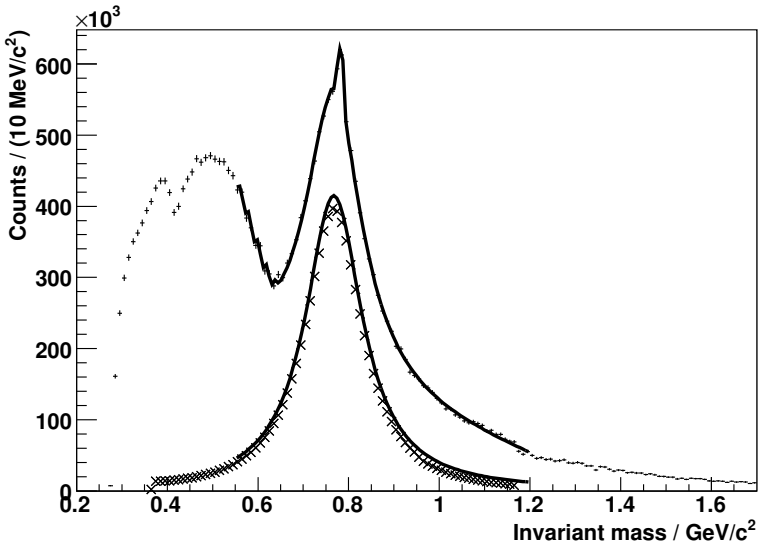

Figure 6.16: Fit of equation 6.5 to like-sign subtracted $\pi^+\pi^-$ spectrum for resonance candidates with $0 < p_t < 1$ GeV/c. The solid dots show the like-sign subtracted spectrum and the crosses show the ρ^0 component. The ρ^0 component of the fit is also shown in the plot for comparison with the actual ρ^0 contribution.

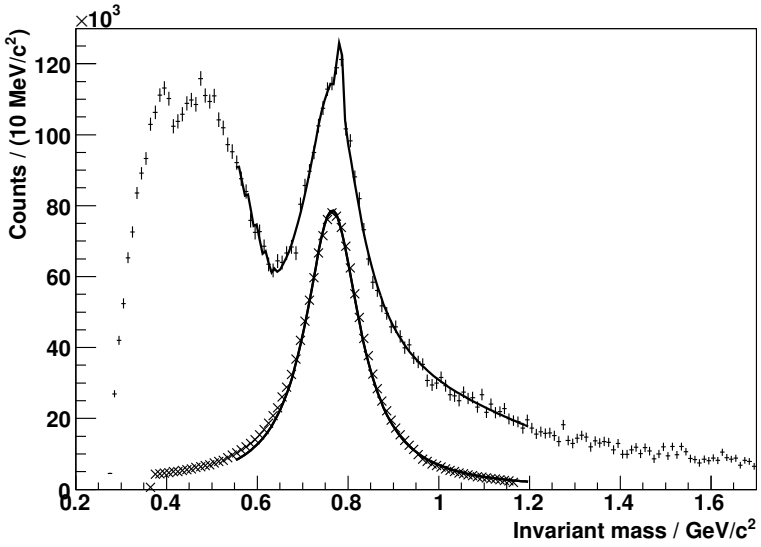

Figure 6.17: Fit of equation 6.5 to like-sign subtracted $\pi^+\pi^-$ spectrum for resonance candidates with $1 < p_t < 2$ GeV/c. The solid dots show the like-sign subtracted spectrum and the crosses show the ρ^0 component. The ρ^0 component of the fit is also shown in the plot for comparison with the actual ρ^0 contribution.

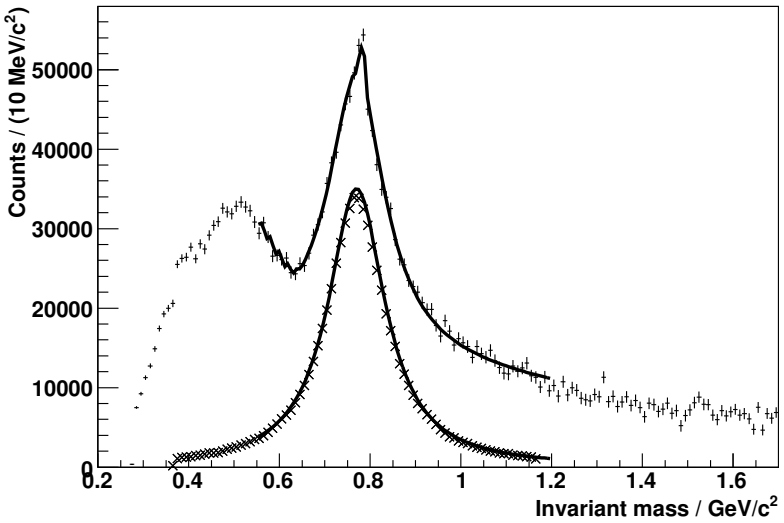

Figure 6.18: Fit of equation 6.5 to like-sign subtracted $\pi^+\pi^-$ spectrum for resonance candidates with $2 < p_t < 4$ GeV/c. The solid dots show the like-sign subtracted spectrum and the crosses show the ρ^0 component. The ρ^0 component of the fit is also shown in the plot for comparison with the actual ρ^0 contribution.

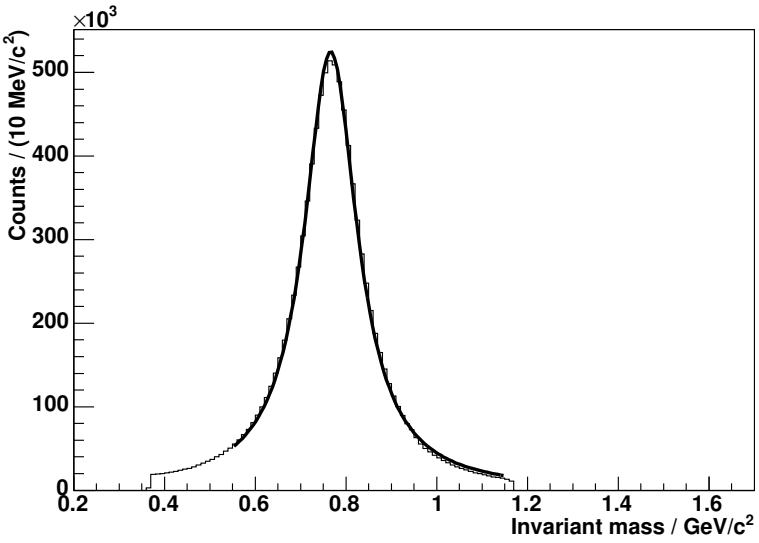

Figure 6.19: A fit to the reconstructed ρ^0 signal, with all background removed using the Monte Carlo truth information. The fitted mass is 0.76626 GeV/c^2 and the fitted width is 0.14277 GeV/c^2.

quantities for p_t below 4 GeV/c, though the errors quoted for the mass measurement are an underestimate. The extracted yield is also consistent with the value obtained using the Monte Carlo truth information.

Systematic errors in fits

As a systematic error due to the distortion of the ρ^0 shape was observed in the Pb-Pb results, the possibility was investigated for pp as well. Figure 6.19 shows a fit of a Breit-Wigner function to the reconstructed ρ^0 signal, with all the background removed using the Monte Carlo truth information. The fitted mass, with MINOS errors, was 0.76626 ± 0.00003 GeV/c^2 and the fitted width was 0.14277 ± 0.00007 GeV/c^2. This can be compared to the fitted values for the generated ρ^0 spectrum, as shown in table 6.6. The generated ρ^0 spectrum is the same for pp and Pb-Pb as the resonance decay routines and the mass and width inputs are the same in both cases.

Table 6.6: Fitted values of ρ^0 mass and width for generated and reconstructed ρ^0s, and a comparison to the generator input values.

	Gen. Value	Fit to generated	Fit to reconstructed (pp)
Mass / GeV/c^2	0.7685	0.76736 ± 0.00016	0.76626 ± 0.00003
Width / GeV/c^2	0.151	0.14813 ± 0.00037	0.14277 ± 0.00007

It is clear from these results that the distortion of the ρ^0 spectrum is an issue for pp, as it was for Pb-Pb, and introduces a systematic error in the measurement of the ρ^0 properties. The systematic shift in the width is similar for pp and Pb-Pb but the shift in the mass is much smaller. Interestingly, the fitted mass and width for the ρ^0s with background are closer to the correct values than the ones without background, suggesting an additional systematic error which acts in the opposite direction to the error introduced from the distortion. As in the Pb-Pb case, a full Monte Carlo study must be carried out when analysing the real data to obtain reliable estimates of all sources of error.

6.3.3 Signal-to-background ratio and significance

Table 6.7 shows the significance and S/B values for the ρ^0 in p_t sub-regions for PYTHIA pp events. As expected, the signal-to-background ratio is much larger for pp than Pb-Pb, due to the much smaller number of tracks per event. However, this is not an effective indicator of the quality of fit that can be obtained. As was the case for Pb-Pb, the signal significance is a more useful quantity. Whereas S/B increases with p_t, significance decreases, and the results obtained from the fit become poorer. As was previously observed in Pb-Pb events, the PID becomes less effective as p_t increases, and so the result quoted for 4-10 GeV should be regarded with caution. The PID cuts will disproportionally favour ρ^0s with p_t at the lower end of this range. To obtain useful results at high p_t, the use of PID must be re-assessed, and perhaps

avoided completely.

Table 6.7: Signal, background, significance and S/B values for ρ^0 in various p_t regions for the sample of 50 million PYTHIA pp events analysed. Significance is also shown for the expected 1 year total of 10^9 pp events.

p_t range	Signal	Background	S/B	Significance	
				5×10^7 events	10^9 events
All	8520012	359672175	0.0237	444	1986
Below 1 GeV/c	6554183	296217252	0.0221	377	1686
1-2 GeV/c	1307041	53435309	0.0245	177	792
2-4 GeV/c	567570	9421182	0.0602	180	805
4-10 GeV/c	90299	596055	0.1515	109	487

6.3.4 Conclusions for pp measurements

These results show that, for pp events, the ρ^0 properties can be measured as a function of p_t to at least $p_t = 4$ GeV/c. The same systematic errors which were present in the Pb-Pb analysis are also present in the pp analysis, and so many of the conclusions are the same as described in section 6.2.12.

The most important differences between the pp and PbPb results are consequences of the much larger number of events available for pp. As a result of the larger sample, the statistical error in the yield measurement is greatly reduced. For all p_t in pp collisions, the measured ρ^0 yield is $177.0^{+7.0}_{-4.7}$ per 1000 events as compared to the true value of 170.4 per 1000 collisions, as shown in table 6.5. For PbPb collisions, the measured ρ^0 yield is $2.30^{+0.69}_{-0.47} \times 10^5$ per 1000 collisions as compared to the true value of 1.98×10^5 per 1000 collisions. It is clear that the error in the yield measurement is much lower for pp. However, as a consequence, the effect of

systematic errors is more clear, as the quoted error is the MINOS statistical error only.

The clear improvement of yield measurement capability with sample size suggests that a detailed measurement of the ρ^0 yield in pp collisions as a function of p_t should be possible, and a similar measurement should be possible with a full year's Pb-Pb event sample of 2×10^7 events. The larger event sample also appears to improve the measurement of the ρ^0 width, although, as for Pb-Pb, the MINOS error is not a good estimate of the total error. It is necessary to have the same care with regards to systematic errors as is required for Pb-Pb.

6.4 Limitations of these studies

The studies described here make use of the predictions of the PYTHIA and HIJING Monte Carlo generators. The uncertainties in the generators' predictions of track multiplicity, ρ^0 abundance etc. are large. Consequently, the significance may be much better or worse than indicated here, although the consistency of the HIJING prediction of the ρ^0/π ratio with previous experiments suggests that the predictions are, at least, not unreasonable.

The particle identification used here is not available for high p_t tracks. In particular, the conventional ALICE PID starts to lose the ability to distinguish between π and K at $p_t = 2$ GeV/c. Therefore, studies for $p_t > 4$ GeV/c will require different PID selection criteria to those used here.

One possible method for improving PID at high momentum is to make use of the relativistic rise effect. For values of γ above about 4, relativistic effects causes the energy loss of a particle in a medium to increase logarithmically up to a plateau at a $\beta\gamma$ of a few hundred [105]. This effect, not included in the PID procedure used here, may allow hadron identification at higher p_t than was previously available,

and therefore may allow the K^{0*} contamination to be removed for higher p_t than indicated here.

Finally, the study does not take into account any effects which may be present in reality but which the generator does not predict. Due to the low signal-to-background ratio, small systematic effects can have a large influence on the ρ^0 measurements. The real ρ^0 measurement may be complicated by mass shifts of the ρ^0 and ω, changes of the ρ^0 line shape, other resonance contributions and other correlations between particles. As such, this result should be considered as indicating the statistical limits of the ρ^0 measurement.

Chapter 7

Summary and conclusions

The Quark-Gluon plasma (QGP) is a state of matter which is expected to exist under extreme conditions of temperature or density. Such conditions can be produced in the laboratory in relativistic heavy ion collisions, and many experiments have searched for it using various signatures and over a range of collision energies. This thesis has described two such studies:

- The investigation of Ξ production at the NA57 experiment, a fixed target experiment at the CERN SPS.
- The determination of the capability of the ALICE experiment at the CERN LHC to measure ρ^0 production in the hadronic decay channel.

7.1 Strangeness results summary

The NA57 experiment was intended to measure strangeness enhancement in heavy ion collisions by measuring the yields of weakly decaying strange particles in Pb-Pb and p-Be collisions. Strangeness enhancement is believed to be a signature of QGP

formation, as described in section 1.5.2. The analysis of the Ξ in p-Be collisions described in this thesis provided a "control" measurement to which the result in Pb-Pb collisions could be compared. The results of the full set of NA57 and WA97 measurements, of which the Ξ in 40 GeV/c p-Be data point is a part, show that strangeness enhancement occurs in Pb-Pb collisions at both lower and higher SPS energies. The SPS results can be compared to those from the STAR experiment, which involve collisions of a much higher energy. The enhancement factors are comparable for all three of the considered energies, and show a scaling with strangeness content and collision centrality [34]. Canonical suppression model calculations predict a decrease in enhancement with increasing collision energy, with a large difference at the low and high SPS energies [33]. The NA57 results suggest that this is not the case, however errors are large and do not allow a definite conclusion to be drawn. Nevertheless, the strangeness enhancement results from NA57 and WA97 provide evidence which, together with results from other experiments, suggest that the QGP was formed at the SPS.

The ALICE experiment at the LHC will measure strangeness enhancement in heavy ion collisions at energies much greater than were previously available.

7.2 Resonance results summary

Resonance measurements can provide information about the conditions produced in the collision fireball, as described in section 1.6. Resonance yields are affected by daughter particle rescattering and the resonance mass, width and shape may be modified in the medium. Previous experiments have measured resonance properties, but, so far, no conclusive results have been obtained. As the fireball produced in heavy ion collisions at the LHC will be much larger, hotter and longer lived than at any previous experiment, the measurement of resonance properties at ALICE will provide valuable information about conditions which have not been previously

observed.

The results from the ρ^0 analysis described in this thesis indicate that measurement of ρ^0 mass and yield in the hadronic decay channel should be possible in pp and Pb-Pb collisions at ALICE. Extending this measurement to p_t sub-regions should be straightforward for pp and also possible for Pb-Pb. It should also be possible to measure the ρ^0 width, if care is taken to identify and reduce all the systematic errors described in chapter 6.

7.3 Extensions and improvements

There is considerable scope for further analysis of the ρ^0 meson at ALICE. This thesis described the measurement of $\rho^0 \rightarrow \pi^+\pi^-$ for transverse momenta below 4 GeV/c. This could be extended to transverse momenta above 4 GeV/c, though there are difficulties with particle identification at high momenta. More importantly, the leptonic decay channel could be measured.

Measurement of $\rho^0 \rightarrow e^+e^-$ would be a valuable and complementary study, as it would allow measurement of ρ^0s from all stages of the collision system, as described in section 1.6. However, there are additional problems associated with this measurement:

- The branching fraction for the e^+e^- channel is about 4.5×10^{-5}, and so the sample of ρ^0s decaying in this channel is much smaller.
- The particle identification requirements are much stricter, as primary electrons are rare compared to primary hadrons, and even a relatively small probability of hadron misidentification could swamp the genuine electron signal.
- There is potentially a large source of background from gamma conversions and π^0 decays.

However, the excellent tracking and particle identification performance available at ALICE mean that such problems may be solvable, and this decay channel is worthy of investigation. A comparison of hadronic and leptonic measurements at the same experiment will be valuable.

The LHC is expected to start up in 2008, taking data from pp collisions, and the first Pb-Pb collisions are expected in 2009. As data from a new detector using conditions in a new energy regime will become available, the next few years will be a particularly interesting time for heavy ion physics, and the results shown here indicate that we can be optimistic that ALICE will be able to make a contribution to studies of the ρ^0 resonance in heavy ion collisions.

Appendix A

Bayesian PID in the ALICE detector

Bayes' theorem [106] is used to assign probabilities of a particle being a certain species based on individual detector information, and to combine the results of several detectors [93].

A.1 PID in a single detector

Let $r(s|i)$ be the probability of observing a PID signal s if a particle of type i is detected. It is necessary to find $w(i|s)$, the probability of a particle being of type i if the signal s is observed. This depends on $r(s|i)$ and a factor C_i, which is the *a priori* probability of a track being of species i. For example, the relative abundances of the different particle species could be used as C_i. Bayes' formula relates these quantities:

$$w(i|s) = \frac{C_i r(s|i)}{\sum_{k=e,\mu,\pi,K,p} C_k r(s|k)} \tag{A.1}$$

It is assumed that C_i and $r(s|i)$ are independent. Values of $r(s|i)$ are calculated for each track, using known properties of the detector. Values of C_i are estimated appropriately and a set of $w(i|s)$ for the subdetector is calculated. The estimate of C_i depends on the situation in which the detector is used, and may reflect relative abundances of particles or probabilities as estimated by other subdetectors.

A.2 Combined PID

The PID information from the various subdetectors can be easily combined. The PID weights $w(i|s_1)$ are used as the values of C_i for the second detector. The output from the combination of detectors 1 and 2 are used as the values of C_i for the third detector, and so on. The following formula is obtained:

$$W(i|s_{all}) = \frac{C_i \prod_{j=1}^{N} r(s_j|i)}{\sum_{k=e,\mu,\ldots} C_k \prod_{j=1}^{N} r(s_j|k)} \tag{A.2}$$

This procedure achieves the following:

- If a detector cannot make any identification for a certain track, this detector does not contribute to the final PID value.
- If several detectors can provide information for a certain track, their contributions are accounted for with appropriate weights, to take into account the quality of information from each subdetector.

- The result is presented in a simple form, and, in the final physics analysis, the particle abundances can easily be taken into account by setting appropriate values of C_i and applying Bayes' formula.

The efficiency and contamination of the combined PID is always better (or equal) than that of the individual detectors. Additionally, these quantities are much weaker functions of momentum than the single detector particle identification.

Bibliography

[1] B.R. Martin and G. Shaw, *Particle Physics*, pages 169–174, John Wiley and Sons Ltd, 2nd edition.

[2] J. Letessier and J. Rafelski, Hadrons and Quark-Gluon Plasma, Cambridge University Press, 2002.

[3] C. Alcock, G. M. Fuller, G. J. Mathews, and B. Meyer, Cosmological Consequences of the Quark-Hadron Phase Transition, *Nucl. Phys.* **A498**, 301c–312c (1989).

[4] E. Witten, Cosmic Separation of Phases, *Phys. Rev.* **D30**, 272–285 (1984).

[5] M. G. Alford, Color superconducting quark matter, *Ann. Rev. Nucl. Part. Sci.* **51**, 131–160 (2001).

[6] H. Fritzsch, M. Gell-Mann, and H. Leutwyler, Advantages of the Color Octet Gluon Picture, *Phys. Lett.* **B47**, 365–368 (1973).

[7] M. Guidry, Gauge field theories - an introduction with applications, John Wiley and Sons, 1999.

[8] S. Bethke, Determination of the QCD coupling alpha(s), *J. Phys.* **G26**, R27 (2000).

[9] A. Chodos, R. L. Jaffe, K. Johnson, C. B. Thorn, and V. F. Weisskopf, A New Extended Model of Hadrons, *Phys. Rev.* **D9**, 3471–3495 (1974).

[10] K. G. Wilson, CONFINEMENT OF QUARKS, *Phys. Rev.* **D10**, 2445–2459 (1974).

[11] D.H. Perkins, Introduction to High Energy Physics, Cambridge University Press, fourth edition, 2000.

[12] P. Pennanen, A. M. Green, and C. Michael, Flux-tube structure and beta-functions in SU(2), *Phys. Rev.* **D56**, 3903–3916 (1997).

[13] S. Hands, The phase diagram of QCD, *Contemp. Phys.* **42**, 209–225 (2001).

[14] B. Muller, Physics and signatures of the quark - gluon plasma, *Rept. Prog. Phys.* **58**, 611–636 (1995).

[15] J. C. Collins and M. J. Perry, Superdense Matter: Neutrons Or Asymptotically Free Quarks?, *Phys. Rev. Lett.* **34**, 1353 (1975).

[16] D. Evans, Strange, Multistrange Baryon, and Antibaryon Production in Sulphur-Tungsten Interactions at 200 GeV/c per Nucleon, PhD thesis, University of Birmingham, 1992.

[17] F. Karsch, Lattice results on QCD thermodynamics, *Nucl. Phys.* **A698**, 199–208 (2002).

[18] C. R. Allton et al., QCD at nonzero chemical potential and temperature from the lattice, *hep-ph/0206200* (2002), Invited paper presented at the Joint Workshop on Physics at the Japanese Hadron Facility, March 2002, Adelaide.

[19] Particle Data Group, July 2002 Particle Physics Booklet extracted from the Review of Particle Physics, K. Hagiwara et al., *Physical Review* **D66** (2002).

[20] F. Antinori et al., First results from the 1994 lead beam run of WA97, *Nucl. Phys.* **A590**, 139c–146c (1995).

[21] F. Antinori et al., Experiment NA57 at the CERN SPS, *J. Phys.* **G25**, 473–479 (1999).

[22] U. Faschingbauer, M. G. Trauth, J. P. Wurm, et al., Study of electron pair production in hadron and nuclear collisions at the CERN SPS, CERN document CERN-SPSC-88-25; SPSC-P-237.

[23] C. Adler et al., Centrality dependence of high p_t hadron suppression in Au + Au collisions at $\sqrt{s} = 130$ GeV, *Phys. Rev. Lett.* **89**, 202301 (2002).

[24] J.W. Harris et al., The STAR Experiment at the Relativistic Heavy Ion Collider, *Nucl.Phys* **A44**, 227c–286c (1994).

[25] D. P. Morrison et al., The PHENIX experiment at RHIC, *Nucl. Phys.* **A638**, 565–570 (1998).

[26] B. Wyslouch, The PHOBOS Experiment at RHIC and AGS, *Nucl.Phys* **A566**, 305c (1994).

[27] F. Videbæk, The BRAHMS experiment at RHIC, *Nucl.Phys.* **A566**, 299c (1994).

[28] F. Carminati et al., ALICE: Physics performance report, volume I, *J. Phys.* **G30**, 1517–1763 (2004).

[29] K. J. Eskola, High energy nuclear collisions, in *High Energy Physics 99, Proceedings of the International Europhysics Conference on High Energy Physics, Tampere, Finland*, pages 231–250, 1999.

[30] P. Koch, B. Muller, and J. Rafelski, Strangeness in Relativistic Heavy Ion Collisions, *Phys. Rept.* **142**, 167–262 (1986).

[31] F. Antinori et al., Production of strange and multistrange hadrons in nucleus nucleus collisions at the SPS, *Nucl. Phys.* **A661**, 130–139 (1999).

[32] M. A. C. Lamont, Recent results on strangeness production at RHIC, *J. Phys. Conf. Ser.* **50**, 192–200 (2006).

[33] A. Tounsi and K. Redlich, Strangeness enhancement and canonical suppression, *hep-ph/0111159* (2001).

[34] H. Helstrup, Results from NA57, *J. Phys.* **G32**, S89–S95 (2006).

[35] M. Asakawa and C. M. Ko, Seeing the QCD phase transition with phi mesons, *Phys. Lett.* **B322**, 33–37 (1994).

[36] R. D. Pisarski, Phenomenology of the Chiral Phase Transition, *Phys. Lett.* **B110**, 155 (1982).

[37] C. A. Dominguez, M. Loewe, and J. C. Rojas, Temperature dependence of the rho meson mass and width, *Z. Phys.* **C59**, 63–66 (1993).

[38] R. D. Pisarski, Where does the rho go? Chirally symmetric vector mesons in the quark - gluon plasma, *Phys. Rev.* **D52**, 3773–3776 (1995).

[39] R. Rapp, G. Chanfray, and J. Wambach, Rho meson propagation and dilepton enhancement in hot hadronic matter, *Nucl. Phys.* **A617**, 472–495 (1997).

[40] R. Rapp and J. Wambach, Chiral symmetry restoration and dileptons in relativistic heavy-ion collisions, *Adv. Nucl. Phys.* **25**, 1 (2000).

[41] R. Rapp and J. Wambach, Low mass dileptons at the CERN-SPS: Evidence for chiral restoration?, *Eur. Phys. J.* **A6**, 415–420 (1999).

[42] G. E. Brown and Mannque Rho, On the manifestation of chiral symmetry in nuclei and dense nuclear matter, *Phys. Rept.* **363**, 85–171 (2002).

[43] C. Markert, What do we learn from resonance production in heavy ion collisions?, *J. Phys.* **G31**, S169–S178 (2005).

[44] J. Adams et al., Experimental and theoretical challenges in the search for the quark gluon plasma: The STAR collaboration's critical assessment of the evidence from RHIC collisions, *Nucl. Phys.* **A757**, 102–183 (2005).

[45] S. Damjanovic et al., First measurement of the rho spectral function in nuclear collisions, *Nucl. Phys.* **A774**, 715–718 (2006).

[46] J. Adams et al., rho0 production and possible modification in Au + Au and p + p collisions at s(NN)**(1/2) = 200-GeV, *Phys. Rev. Lett.* **92**, 092301 (2004).

[47] D. Adamova et al., Enhanced production of low-mass electron pairs in 40-A-GeV Pb Au collisions at the CERN SPS, *Phys. Rev. Lett.* **91**, 042301 (2003).

[48] A. Cherlin and S. Yurevich, Preliminary results from the 2000 run of CERES on low-mass e+ e- pair production in Pb Au collisions at 158-A-GeV, *J. Phys.* **G30**, S1007–S1011 (2004).

[49] S. V. Afanasev et al., Production of Phi mesons in p + p, p + Pb and central Pb + Pb collisions at E(beam) = 158-A-GeV, *Phys. Lett.* **B491**, 59–66 (2000).

[50] M. C. Abreu et al., Production of the phi vector-meson in heavy-ion collisions, *J. Phys.* **G27**, 405–412 (2001).

[51] D. Adamova et al., Leptonic and charged kaon decay modes of the Phi meson measured in heavy-ion collisions at the CERN SPS, *Phys. Rev. Lett.* **96**, 152301 (2006).

[52] S. S. Adler et al., Production of Phi mesons at mid-rapidity in s**(1/2)(NN) = 200-GeV Au + Au collisions at RHIC, *Phys. Rev.* **C72**, 014903 (2005).

[53] R. Baier, D. Schiff, and B. G. Zakharov, Energy loss in perturbative QCD, *Ann. Rev. Nucl. Part. Sci.* **50**, 37–69 (2000).

[54] J. Adams et al., Evidence from d + Au measurements for final-state suppression of high p(T) hadrons in Au + Au collisions at RHIC, *Phys. Rev. Lett.* **91**, 072304 (2003).

[55] T. Matsui and H. Satz, J/Psi Suppression by Quark-Gluon Plasma Formation, *Phys. Lett.* **B178**, 416 (1986).

[56] C. Quintans et al., NA50 final results on charmonia suppression, *J. Phys. Conf. Ser.* **50**, 353–356 (2006).

[57] H. D. Haseroth, The CERN heavy ion accelerating facility, Presented at the 16th Biennial Particle Accelerator Conference - PAC 95, Dallas, TX, USA, 1 - 5 May 1995. Published in IEEE PAC 1995:411-415.

[58] ALICE: Technical Proposal for A Large Ion Collider Experiment at the CERN LHC, Technical report, CERN-LHCC-95-71.

[59] W. W. Armstrong et al., ATLAS: Technical proposal for a general-purpose p p experiment at the Large Hadron Collider at CERN, Technical report, CERN-LHCC-94-43.

[60] CMS, the Compact Muon Solenoid: Technical proposal, Technical report, CERN-LHCC-94-38.

[61] S. Amato et al., LHCb technical proposal, Technical report, CERN-LHCC-98-04.

[62] High Level Trigger Control System ALICE technical design report trigger, Data Acquisuition, Technical report, 2004, CERN-LHCC-2003-062.

[63] F. Antinori et al., Silicon pixel detectors for tracking in NA57, *Nucl. Phys.* **A661**, 716–720 (1999).

[64] P. A. Bacon, A study of negatively charged hadrons in Pb-Pb collisions in the NA57 experiment at the CERN SPS, PhD thesis, University of Birmingham, 2005.

[65] F. Antinori et al., Determination of the event centrality in the WA97 and NA57 experiments, *J. Phys.* **G27**, 391–396 (2001).

[66] S. Beole et al., ALICE technical design report: Detector for high momentum PID, Technical report, CERN-LHCC-98-19.

[67] ALICE technical design report of the photon spectrometer (PHOS), Technical report, CERN-LHCC-99-04.

[68] C. Finck, The muon spectrometer of the ALICE, *J. Phys. Conf. Ser.* **50**, 397–401 (2006).

[69] ALICE The Electromagnetic Calorimeter, Addendum to the Technical Proposal, Technical report.

[70] ALICE technical design report of the inner tracking system (ITS), Technical report, 1999.

[71] G. Dellacasa et al., ALICE technical design report of the time projection chamber, Technical report, 2000, CERN-OPEN-2000-183, CERN-LHCC-2000-001.

[72] P. Glassel, The ALICE TPC: An innovative device for heavy ion collisions at LHC, *Nucl. Instrum. Meth.* **A572**, 64–66 (2007).

[73] ALICE technical design report of the Transition Radiation Detector, Technical report, CERN-LHCC-2001-021.

[74] ALICE technical design report of the time of flight system (TOF), Technical report, CERN-LHCC-2000-012.

[75] G. Scioli, The time of flight (TOF) system of the ALICE experiment, *Eur. Phys. J.* **C39S3**, 7–12 (2005).

[76] A. Bhasin et al., Recent developments on the ALICE Central Trigger Processor, in *Proceedings of the Twelfth Workshop on Electronics for LHC and Future Experiments*, pages 341–345, 2006.

[77] T0 ALICE technical design report on forward detectors: FMD and V0, Technical report, CERN-LHCC-2004-025.

[78] ALICE technical design report of the zero degree calorimeter (ZDC), Technical report, CERN-LHCC-99-05.

[79] G. Di Marzo, P. Jovanovic, P. Vande Vyvre, and O. Villalobos Baillie, Specification and Simulation of the ALICE DAQ System, 6th Workshop on Electronics for LHC Experiments, Cracow, Poland, 11-15 Sep 2000.

[80] J. Podolanski and R. Armenteros, *Phil. Mag* **45**, 13 (1954).

[81] GEANT Detector Description and Simulation Tool, CERN program library long writeup W5013, 1993.

[82] F. Antinori et al., Rapidity distributions around mid-rapidity of strange particles in Pb Pb collisions at 158-A-GeV/c, *J. Phys.* **G31**, 1345–1357 (2005).

[83] F. Antinori et al., Study of the transverse mass spectra of strange particles in Pb - Pb collisions at 158-A-GeV/c, *J. Phys.* **G30**, 823–840 (2004).

[84] F. Becattini and U. W. Heinz, Thermal hadron production in pp and $p\bar{p}$ collisions, *Z. Phys.* **C76**, 269–286 (1997).

[85] F. Antinori et al., Enhancement of hyperon production at central rapidity in 158-A-GeV/c Pb Pb collisions, *J. Phys.* **G32**, 427–442 (2006).

[86] F. Antinori et al., Strange particle production in p Be, p Pb, Pb Pb at 158-A-GeV/c (WA97 experiment), *Nucl. Phys.* **A681**, 141–148 (2001).

[87] C. Y. Wong, *Introduction to High-Energy Heavy-Ion Collisions*, pages 251–264, Singapore: World Scientific, 1994.

[88] F. Antinori et al., Energy dependence of hyperon production in nucleus nucleus collisions at SPS, *Phys. Lett.* **B595**, 68–74 (2004).

[89] D. Elia, private communication.

[90] G. E. Bruno, New results from the NA57 experiment, *J. Phys.* **G30**, S717–S724 (2004).

[91] T. Sjostrand, S. Mrenna, and P. Skands, PYTHIA 6.4 physics and manual, *JHEP* **05**, 026 (2006).

[92] M. Gyulassy and X. N. Wang, HIJING 1.0: A Monte Carlo program for parton and particle production in high-energy hadronic and nuclear collisions, *Comput. Phys. Commun.* **83**, 307 (1994).

[93] B. Alessandro et al., ALICE: Physics performance report, volume II, *J. Phys.* **G32**, 1295–2040 (2006).

[94] K. J. Eskola, K. Kajantie, P. V. Ruuskanen, and K. Tuominen, Scaling of transverse energies and multiplicities with atomic number and energy in ultrarelativistic nuclear collisions, *Nucl. Phys.* **B570**, 379–389 (2000).

[95] N. S. Amelin, N. Armesto, C. Pajares, and D. Sousa, Monte Carlo model for nuclear collisions from SPS to LHC energies, *Eur. Phys. J.* **C22**, 149–163 (2001).

[96] V. Blobel et al., *Phys. Lett. B* **48**, 73 (1974).

[97] R. Singer et al., *Phys. Lett. B* **60**, 385 (1976).

[98] M. Aguilar-Benitez et al., *Z. Phys. C* **50**, 405 (1991).

[99] D. Drijard et al., *Z. Phys. C* **9**, 293 (1981).

[100] H. Albrecht et al., *X. Phys. C* **61**, 1 (1994).

[101] Y. J. Pei et al., *Z. Phys. C* **72**, 39 (1996).

[102] F. C. Winkelmann et al., *Phys. Lett. B* **56**, 101 (1975).

[103] P. V. Chliapnikov et al., *Nucl. Phys. B* **176**, 303 (1980).

[104] F. James and M. Roos, Minuit: A System for Function Minimization and Analysis of the Parameter Errors and Correlations, *Comput. Phys. Commun.* **10**, 343–367 (1975).

[105] W. W. M. Allison and P. R. S. Wright, The Physics of Charged Particle Identification: dE/dx, Cerenkov and Transition Radiation, in *Experimental Techniques in High Energy Physics*, edited by T. Ferbel, pages 371–417, 1987.

[106] T. Bayes, An Essay towards solving a Problem in the Doctrine of Chances, *Philosophical Transactions of the Royal Society of London* **53**, 370–418 (1763), communicated by Mr. Price, in a letter to John Canton, M. A. and F. R. S.